2021

PHYSICOCHEMICAL PROPERTIES OF ATMOSPHERIC AEROSOLS AND THEIR EFFECT ON ICE CLOUD FORMATION

Nurun Nahar Lata
Michigan Technological University, nnlata@mtu.edu

PHYSICOCHEMICAL PROPERTIES OF ATMOSPHERIC AEROSOLS AND THEIR EFFECT ON ICE CLOUD FORMATION

By

Nurun Nahar Lata

A DISSERTATION

Submitted in partial fulfillment of the requirements for the degree of

DOCTOR OF PHILOSOPHY

In Atmospheric Sciences

MICHIGAN TECHNOLOGICAL UNIVERSITY

2021

This dissertation has been approved in partial fulfillment of the requirements for the Degree of DOCTOR OF PHILOSOPHY in Atmospheric Sciences.

Department of Physics

Dissertation Advisor:	*Dr. Will Cantrell*
Committee Member:	*Dr. Raymond Shaw*
Committee Member:	*Dr. Lynn Mazzoleni*
Committee Member:	*Dr. Sapna Sarupria*
Committee Member:	*Dr. Swarup China*
Department Chair:	*Dr. Ravindra Pandey*

Dedication

To my respectful Father and Mother

for their love and prayer.

Contents

List of Figures

List of Tables

Preface

I want to mention that portions of this dissertation have already been published in peer-reviewed journals. Chapter two is based on a portion of paper in preparation. I am one of the co-author of this preprint. The preprint of this work can be found under CC BY NC ND 4.0 License.The license information is attached in A.1 Chapter three is based on a paper published in Journal of Physical Chemistry Letters (Lata et al. 2020). I performed the experimental work, data analysis and interpretation.The simulation work, data analysis and interpretation was performed by our collaborator. This paper was written by me with input from my advisor Dr. Will Cantrell and other co-authors. Permission to use the published materials was granted and the documentation of the permission is attached in Appendix A.2. Chapter four is based on a paper published in ACS Earth & Space Chemistry Journal (Lata et al. 2021). I performed all the data analysis and interpretation of the results. This paper was written by me with input from my internship mentor Dr. Swarup China and other co-authors. Permission to use the published materials was granted and the documentation of the permission is attached in Appendix A.3. Chapter five is based on a manuscript that we plan to submit to the Journal of Geophysical Research Letters. For their efforts, we are deeply grateful to all of our co-authors and colleagues.

Acknowledgments

I am thankful to my research advisor Dr. Will Cantrell for his unwavering support, guidance, and encouragement throughout my Ph.D. research. I feel fortunate to have had the opportunity to work with him. He provided tremendous guidance and was always patient and willing to assist.

I would like to thank Dr. Raymond Shaw, Dr. Sapna Sarupria, Dr. Lynn Mazzoleni and Dr. Swarup China for participating on my PhD dissertation committee.

Thanks to Dr. Sarupria for the valuable discussion on mica-ice collaboration work, which helps me to improve my understanding of molecular dynamic simulation. I would like to thank Dr. China, my mentor during my internship at Pacific Northwest National Laboratory (PNNL). I owe my greatest gratitude to him for his valuable guidance and support for the research work I had conducted at PNNL. Special thanks to him for including me in a variety of projects and for establishing a broad collaboration network that allowed me to be exposed to a variety of studies and connect with a variety of researchers. I would like to thank Dr. Claudio Mazzoleni for the valuable science discussion and guidance for the Pico project.

Additionally, I would like to thank Dr. Ravindra Pandey, Claire Wiitanen, Ms Andrea Lappi, Mr. Jesse Nordeng, Mr. Slough their assistance with my research in

one way or another. I would like to express our gratitude to the MTU Atmospheric Science Program, the MTU Physics Department, the MTU Graduate School for their support. I want to acknowledge National Science Foundation, U.S. Department of Energy, Office of Science (BER), Atmospheric System Research, Atmospheric Radiation Measurement, PNNL, Environmental Molecular Sciences Laboratory for providing fund to conduct the research works.

Finally, I want to offer my sincere gratitude to my loved ones- my mother, my sisters and my sister-in-laws for all of their support and encouragement throughout the writing process. I owe a lot to my better half Ashfiqur Rahman for all of his help, guidance and motivation throughout the PhD.

List of Abbreviations

AFM	Atomic Force Microscopy
ALS	Advanced Light Source
ARM	Atmospheric Radiation Measurement
CCSEM/EDX	Computer Controlled Scanning Electron Microscopy coupled with Energy Dispersive X-Ray Spectroscopy
CPC	Condensation Particle Counter
FLEXPART	Lagrangian Flexible Particle dispersion model
FTIR	Fourier Transform Infrared Spectroscopy
HYSPLIT	Hybrid Single Particle Lagrangian Integrated Trajectory
IN	Ice Nucleation
INP	Ice Nucleating Particle
INESEM	Ice Nucleation Environmental Electron Microscopy
MD	Molecular Dynamics
MPC	Mixed Phase Cloud
OMP	Observatory of Mountain Pico
OVF	Organic Volume Fraction
PCF	Pore Condensation Freezing
POPS	Portable Optical Particle Spectrometer

PSAP	Particle Soot Absorption Photometer
RH	Relative Humidity
STXM/NEXAFS	Scanning Transmission X-Ray Microscopy coupled with near-edge x-ray absorption and fine structure
TBS	Tethered Ballon System

Abstract

Atmospheric aerosols play a vital role in the Earth's energy budget-directly by scattering and absorbing solar radiation and indirectly by acting as cloud condensation nuclei and ice-nucleating particles [1, 2]. The cloud formation potential of aerosol is driven by multiple factors, including surface properties, size distribution, composition, mixing state, phase state, and morphology [3]. The interaction of aerosols with clouds alters the aerosol's physicochemical properties. Those properties can also evolve during transport due to atmospheric processing, in turn, affect the aerosol's ice nucleation and cloud formation activities. This thesis presents experimental studies to understand the role of physicochemical properties of aerosol on the formation of ice.

To get a detailed understanding of the aerosol effect on ice nucleation, we conducted controlled ice nucleation experiments on a known surface (muscovite mica) with controlled properties (e.g., surface cations) as well as ice nucleation experiments on complex atmospheric particles, which were characterized with multimodal microspectroscopic techniques. The results from controlled experiments suggest that the ice nucleation activity of a surface can be modified by simply changing the surface cations. In contrast, ice nucleation experiments with complex atmospheric particles indicates a more complicated dependence on the physicochemical properties.

Chapter 1

Introduction

Although clouds are most well known for their effect on precipitation, their impact on global climate and Earth's living creatures is crucial [2, 4]. For example, the effect of clouds and aerosol particles on Earth's radiation budget is highly substantial. Short-wave and long-wave radiation interacts with clouds, altering the flow of radiant energy [5]. Precipitation starts with clouds; therefore they're vital to the water cycle and, hence, to the transmission of latent heat and the distribution of freshwater [6].

Cloud microphysical features dictate how precipitation forms, how radiation interacts with clouds, and how long clouds last. Aerosol particles serve as cloud condensation nuclei (CCN), activating into cloud droplets and so contributing significantly to cloud characteristics [1, 7] . However, cloud microphysical features remain a mystery due to the system's complexity [8]. Indeed, aerosol-clouds interactions account for one of

the major uncertainty in today's climate change estimation [9]. Clouds carrying ice are a key source of uncertainty due to the lack of understanding of their formation mechanism and continued evolution [10]. As such, the next sections explain our current understanding of cloud formation, with a focus on the formation of atmospheric ice via heterogeneous mechanism.

1.1 Role of Aerosol in Cloud Formation

Aerosol particles are produced by a wide range of natural and man-made processes [11]. Primary aerosol particles are released directly into the atmosphere by a variety of sources, including sea salt from bubble breaking at the ocean's surface, mineral dust from deserts, volcanic eruptions, smoke from forest fires, and other combustion processes such as coal burning. Biological particles such as pollen and viruses, as well as biogenic organic compounds, also contribute significantly to atmospheric aerosols. Secondary organic aerosol particles are produced in the atmosphere when gas phase organic species react to form low-volatility compounds that condense as a particle. Industrial emissions, transportation, agricultural activities, and the burning of coal and fossil fuels all contribute to the quantity and composition of aerosol particles in the atmosphere.

1.1.1 Aerosol as Cloud Condensation Nuclei (CCN)

Clouds are mainly comprised of liquid water in the lower troposphere, but as altitude rises, the proportion of ice to liquid water in clouds increases until they reach the

high troposphere, at which they are predominantly composed of ice [12]. Aerosol particles may act as CCN in the lower troposphere (where liquid water dominates cloud formation) by absorbing water and forming liquid cloud droplets to create water clouds. Indeed, the production of all liquid droplets in the atmosphere is dependent on the existence of a nucleating aerosol particle. The particle's hygroscopicity heavily influences its effectiveness as a CCN [13]. Clouds in areas with a high concentration of CCN are composed of a greater number of tiny water droplets. This modification of the cloud's microphysical characteristics results in increased reflectance, decreased precipitation efficiency, and prolonged cloud lifetimes [8].

1.1.2 Aerosol as Ice Nucleating Particle (INP)

Aerosol particles may act as ice nucleating particle (INP) by providing a surface on which ice can develop in the atmosphere. Only a small fraction of the total population of atmospheric aerosols has the potential to catalyze the formation of ice [14]. Such atmospheric INPs may have a low population (e.g. one out of 10^5 - 10^6 particles) [15, 16, 17]. Atmospheric ice can be formed by homogeneous or heterogeneous mechanism. It's believed that heterogeneous nucleation may take place in four different ways: deposition, immersion, condensation, and contact [18]. In deposition mode, ice forms immediately on the surface from vapor phase. A previous study showed that this ice nucleation (IN) mode is important for cirrus cloud production but not so much for mixed phase cloud (MPC) development [19].This finding is confirmed by lidar measurements (in conjunction with radiosonde temperature and humidity

profile data) indicating that the liquid phase exists in clouds below 8–8.5 km above sea level prior to the production of ice crystals [20]. On the other hand, a different study suggests that what is commonly referred to as deposition nucleation can be pore condensation and freezing (PCF) occurring in pores (surface defects and/or the porous nature of INPs) on INPs, that may hold water due to surface curvature forces rather than deposition nucleation [21]. In the case of immersion mode, the INPs are immersed in the supercooled cloud droplet and facilitate ice formation. Immersion freezing is considered to be the most significant mode in MPCs [20, 22]. Similarly, condensation freezing takes place when water condensed on a particle at saturation and instantly freezes. On the other hand, the contact freezing process is initiated when an aerosol particle collides with a supercooled liquid droplet. The particle inside the interior of droplet migrates to the surface where it may cause freezing [23]. Researchers believe that the effectiveness of the method depends on the particle's location relative to the droplet's surface [23]. Supercooled cloud droplet freezing, as seen in nature, is restricted by the degree of interaction between particles (e.g., by a collision rate) which determines how relevant the phenomenon is to the atmosphere [24]. The effect of collisions with supercooled cloud droplets caused certain particles to deliquesce already at the surface that initiated ice formation [25]. Overall, different modes of ice nucleation in demonstrating heterogeneous ice nucleation indicates its intricacy in understanding the formation mechanism.

1.2 Factors Affecting Ice Nucleation Propensity of Aerosols

It is yet not clear what characteristics of aerosols make one type of aerosols more efficient IN than other. Though, a previous study demonstrated a set of pre-requisites of good INPs [26], but there are lots of exceptions also observed. The requirements include insolubility, size, chemical bonding and crystallographic structure. The insolubility requirement states that good INPs are mostly insoluble in water. The obvious drawback of a soluble substrate is that it is not rigid to support an ice nucleus and catalyze formation. For example, salt aerosols are not good INPs because they are soluble in water, thus disintegrate upon interaction with water and cannot provide a surface to form ice. Salt ions also reduce the effective freezing temperature. In contrast, dust particles are insoluble, thus providing a rigid surface to support the critical embryo formation. However, numerous exceptions exist to this condition. For instance, ammonium sulphate, a crystalline soluble salt, has been seen to nucleate ice in saturated solution droplets [27]. As a result, it has been suggested to be reintroduced this criterion as a solid requirement instead of an insolubility requirement [28]. The size criterion states that larger aerosols are more efficient INPs. The chemical bonding requirement of a good INP states that the particle should have hydrogen bonds available at its surface because ice crystal hydrogen bonds hold them together. Therefore, an excellent INP should also have hydrogen bonds available at its surface.

Particle's ice nucleation behavior can also be affected by the active sites, which include surface cracks or chemical impurities [14]. According to that requirement, the crystallographic structure of a surface is also important like chemical composition. It is generally accepted that the closer a material's crystallographic match to ice, the greater the material's ice nucleating capacity will be. For example, muscovite mica's basal surface has a pseudo hexagonal structure close to the ice structure. But several studies showed mica's poor ice nucleation ability [29, 30]. On the other hand, organic aerosols [31], and soot [32] are examples of amorphous materials that can aid ice production but exhibit no similarity to ice's crystal structure. However, only these criterions have not been effective in finding more efficient INPs or in advancing our understanding of ice nucleation significantly.

In the atmosphere, chemical and physical changes may occur in aerosol particles because of things like aging from photochemical reactions and chemical reactions with other gases and inorganic species [33]. During these processing, the chemical species react or accumulate on the aerosols which affects the physicochemical properties [34, 35, 36]. During transportation, the particles come into contact with reactive gases or semivolatile species; they may develop a protective coating. The IN ability of aerosol particles can be increased [26] or decreased [34, 35, 37, 38] as a result of aging processes. How the evolution of physicochemical properties of aerosols upon short range and long range transport affects ice nucleation propensity is crucial to improve our understanding of the effect of physicochemical properties on ice nucleation.

1.3 Research Objectives and Organization of the Dissertation

Ice in clouds affects microphysics and is an important component of weather and climate modeling. A huge variation between predicted rates of ice nucleation and the actual crystal concentration measured in clouds is partly due to inefficacy in accurate modeling of heterogeneous ice nucleation [39, 40]. This inefficacy is caused by the inability to predict the effect of surfaces on the kinetics and thermodynamics of ice nucleation. Thus, detailed study is required to understand the effect of surface characteristics such as chemical composition, surface functional groups and topography on ice nucleation, which affect the ice nucleation efficiency of a surface by changing the interaction of water with it. So, it is necessary to investigate the effect of surface properties on ice nucleation to get a mechanistic explanation of ice formation in cloud.

To elucidate the effect of surface properties on ice nucleation, the most significant experimental data have come from atmospheric chemistry and surface science. The two fields, on the other hand, examine a wide range of length scales and environmental variables. For example, researchers in atmospheric chemistry study the effects of complex atmospheric particles such as mixed dusts, different internally mixed aerosols on ice nucleation, whereas surface scientists work under carefully controlled settings on well-known surfaces such as muscovite mica, feldspar etc. Both fields provide valuable

insights to understand the IN in atmosphere. Though atmospheric chemists measure the IN propensity of different types of complex aerosols, the molecular detail of ice formation is not known. In contrast, surface scientists investigate the IN propensity on known substrates under controlled experimental conditions and provide a better understanding of the molecular details of ice formation on a surface. However, the contribution of both of the fields are crucial to understand atmospheric ice nucleation. This dissertation discusses both of these approach to elucidate the effect of physicochemical properties of aerosols on ice formation. This section describes the objectives of the dissertation and gives a quick overview of the dissertation's structure and chapter arrangement.The following is a list of chapters, along with a short explanation of what each one contains:

1.3.1 Chapter 2

Surface ions play a vital role on the adsorption of water [41]. The presence of different ions on the same surface affect the structure of water differently [42]. This chapter describes the findings from controlled laboratory experiments on a known substrate muscovite mica, probing the effect of surface properties, e.g., surface cations, on water structure. We use Fourier transform infrared spectroscopy to investigate thin layers of water at the mica-air interface.

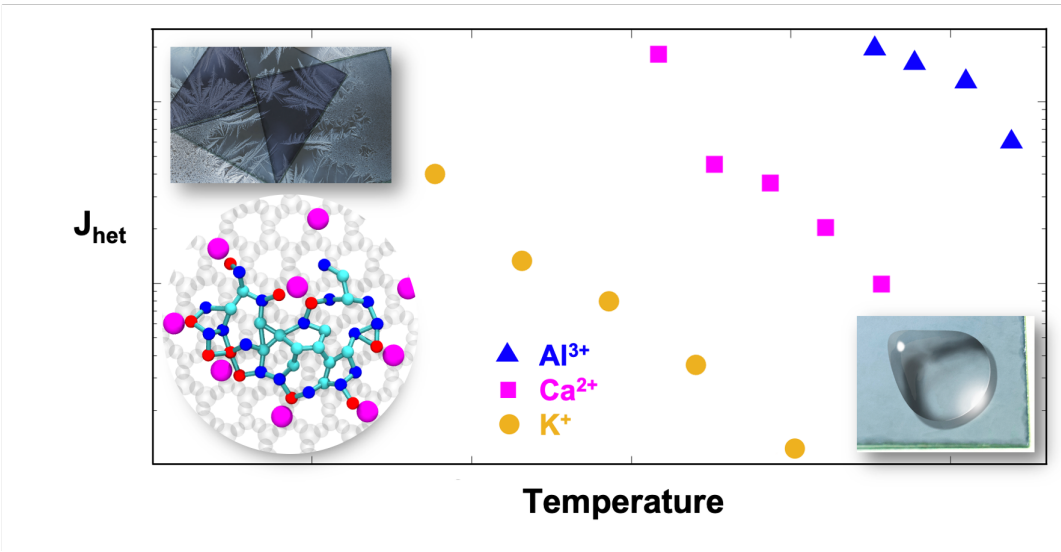

Figure 1.1: Adopted with permission from Lata et al, 2020 [43]. Copyright 2020 American Chemical Society. Schematic showing the synergistic experiment and simulation study to elucidate the role of surface cations on IN.

1.3.2 Chapter 3

The presence of different surface cations affect the water adsorption which may also affect the ice nucleation propensity. This chapter discusses the results from controlled laboratory experiments and molecular dynamic simulations on a known substrate to investigate the effect of surface cations on heterogeneous freezing of water (Figure 1.1). This study is already published in a peer reviewed journal [43]. In this study, we choose muscovite mica as a model substrate because in mica, the exposed ions on the surface may be easily swapped without impacting other characteristics such as surface roughness. This study reveals that liquid water freezes at higher temperatures when ions with higher valency are present on the surface. In addition, our findings indicate that the size of the ion has an effect on the typical freezing temperature. We also

investigate how ion valency and an exposed silica layer affect surface water behavior using molecular dynamics simulations. According to the findings, large clusters of hydrogen-bonded water molecules are more likely to form when multivalent cations are present. Additionally, these clusters contain a significant amount of free water that can reorient into ice-like configurations, which are favored by the ion-free regions on mica.As a result, these clusters may act as seedbeds for the formation of ice nuclei.

1.3.3 Chapter 4

Atmospheric aerosols are complex mixture of different types of particles. The physicochemical properties of these aerosols may vary from near the emission source to far from it. Because, these aerosols undergo atmospheric processing or aging as they travel through the atmosphere, interacting with other chemical species and reacting or building up, changing their properties. This in turn affects the ice nucleation propensity. This chapter focuses on the effect of physicochemical properties of free tropospheric aerosols on ice nucleation. This study is already published in a peer reviewed journal [3]. Figure 1.2 shows the schematic of evolution of physicochemical properties of aerosols and their effect on ice nucleation. Here, we investigated free tropospheric particles collected at the remote Pico Mountain Observatory at 2225m a.s.l. in the North Atlantic Ocean using multimodal micro-spectroscopy and chemical imaging techniques. We probed their ice formation propensity using an ice nucleation stage interfaced with an environmental scanning electron microscope.

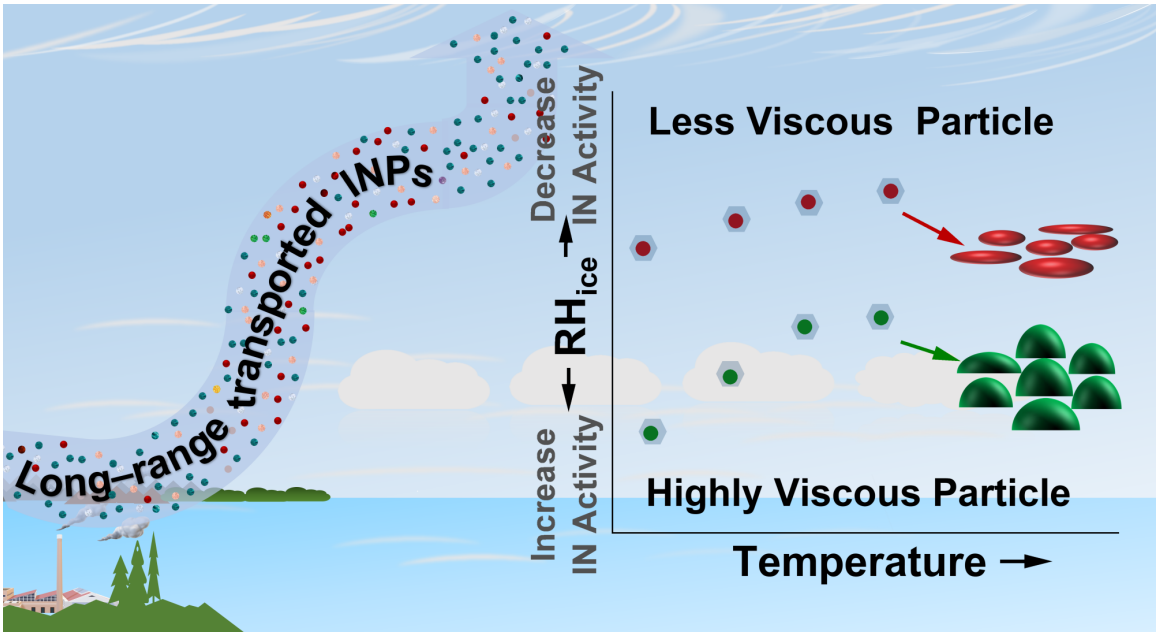

Figure 1.2: Adopted with permission from Lata et al, 2021 [3]. Copyright 2021 American Chemical Society. Schematic showing the evolution of physicochemical properties of aerosols upon long range transport and and their effect on ice nucleation

Retroplume analysis, chemical imaging, and micro-spectroscopy analysis indicated that the size-resolved chemical composition, mixing state, and phase state of the particles with similar aging times but different transport patterns were substantially different. Relative humidity-dependent glass transition temperatures estimated from meteorological conditions were consistent with the observed particles' phase. More viscous (solid and semi-solid-like) particles nucleated ice more efficiently compared to those less viscous. This study provides a better understanding of the phase and mixing state of long-range transported free tropospheric aerosols and their role in ice cloud formation.

1.3.4 Chapter 5

The physicochemical properties of aerosols play a vital role in affecting the Arctic climate via both aerosol-radiation and aerosol-cloud interactions [44]. Several ground-based observations demonstrate the climatic impacts of seasonal variation of Arctic aerosol [45, 46]. However, the current understanding of aerosol-cloud interactions in the vertically stratified Arctic atmosphere is still limited. Moreover the physicochemical properties of aerosol is also modified upon interaction with clouds. However, this process is poorly understood due to lack of our understanding about the aerosol cloud interaction. So, it is necessary to characterize the aerosols before interaction with cloud and also after interaction with cloud. Chapter five discusses the vertical profile of aerosols over the Arctic where aerosol particles were collected in between the cloud and above the cloud to understand the change of physicochemical properties. Figure 1.3 is a schematic showing the change of physicochemical properties along vertical direction. A tethered balloon system (TBS) was deployed at the U.S. Department of Energy Atmospheric Radiation Measurement Program's facility at Oliktok Point Alaska on the coast of the Arctic Ocean (2m above sea level) to study the vertical profile of the aerosols. The aerosol sampling was performed at different altitudes, ranging up to 1100m employing a cascade impactor during August 2019. We aim to understand the sources and atmospheric processing of aerosol by investigating ground-based in-situ and remote sensing data, backward trajectory analysis, and off-line size-resolved chemical composition analysis. We perform single-particle

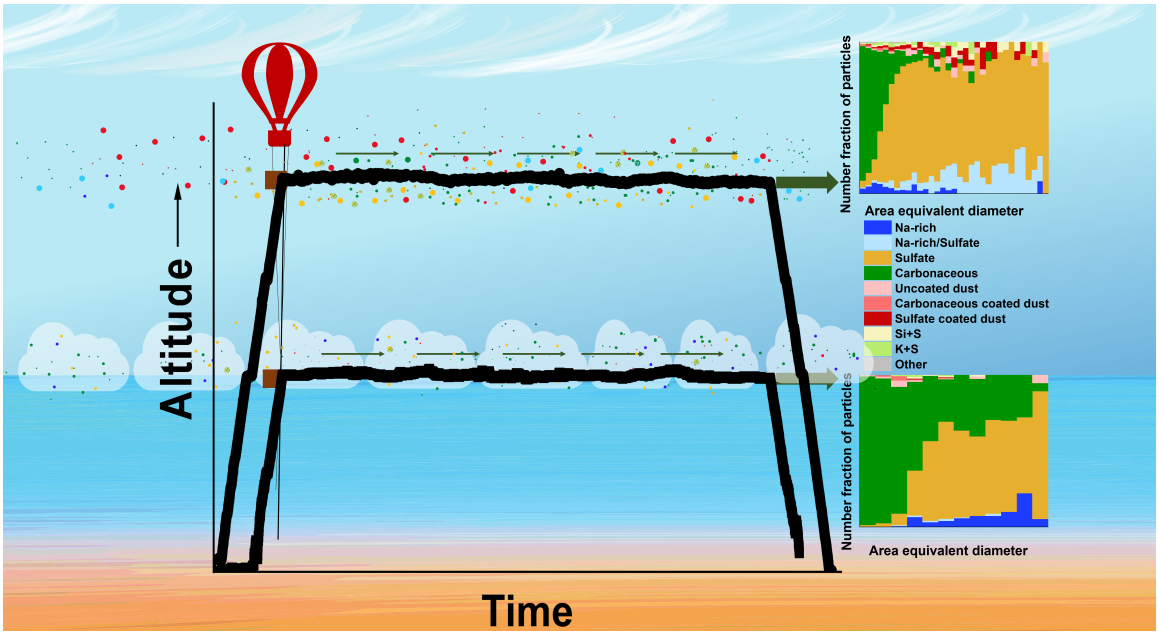

Figure 1.3: Schematic showing the evolution of physicochemical properties of aerosols along the vertical direction

analysis using chemical imaging and multi-modal micro-spectroscopy techniques such as computer-controlled scanning electron microscopy with energy-dispersive X-ray spectroscopy, transmission electron microscopy and scanning transmission X-ray microscopy with near-edge X-ray absorption fine structure spectroscopy. Our results show a clear difference in aerosol chemical compositions at various altitudes on the same day and also on different days. Broadening of the size distribution of the particles at high-altitude was observed in comparison to low low-altitude particles on the same sampling day. A relatively higher percent of sulfate and sulfate coated dust aerosols were observed at higher altitudes which suggests the possibility of cloud processing of aerosols. Altogether, the findings from this study will improve the understanding of the implication of Arctic aerosol on Arctic cloud formation and

radiative properties.

Chapter 2

Water structure on mica surfaces: Investigating the effect of cations

[1]

2.1 Introduction

A single water molecule has a deceptively simple structure but, in the aggregate, water is highly complex. Even though immense effort has been invested in studying water, we still do not know enough to uncover its role in many physical or chemical processes. This is despite the fact that efforts to understand it span early experimental spectroscopy to uncover its anomalies to the most recently developed water

[1]This chapter contains the portion of a paper in preparation by Zhou J, Lata NN, Sarupria S, cantrell will. Water Structure on Mica Surfaces: Investigating the Effect of Cations. ChemRxiv. Cambridge: Cambridge Open Engage; 2019; This content is a preprint and has not been peer-reviewed. The license information is attached in Appendix A.1. The content is available under CC BY NC ND 4.0 License CreativeCommons.org

models encompassing classical dynamics and quantum effects. A simple example is elaborating the mechanisms through which water sticks to surfaces – what factors govern the amount of water that adsorbs to a surface for a given set of conditions? The answer(s) to this seemingly innocuous question has consequences for fields ranging from biology, tribology, and cloud physics. The complexity of water's interactions with solid surfaces stems in part from the fact that a surface's structure and chemistry affect the water molecules adsorbed to it while simultaneously, adsorbed water molecules can change the surface.

Early investigators in the field identified muscovite mica as one of the best natural substrates for experiments [47] because the basal plane is almost atomically flat when cleaved [48, 49, 50], reducing the complication of interpreting the effects of defects on water-surface interactions. The thickness of water films adsorbed on mica's basal surface ranges from one to several molecular layers [51, 52, 53, 54, 55], varying as a function of the partial pressure of water vapor, or relative humidity, RH. ($RH \equiv \frac{p_v}{p_s(T)}$, where p_v is the partial pressure of water vapor and $p_s(T)$ is the equilibrium vapor pressure for the temperature, T, given by the Clausius-Clapeyron equation.) Like many vapors adsorbed to solid surfaces, the structure of water adsorbed on mica departs from that of the bulk liquid [50, 56, 57, 58, 59, 60, 61, 62, 63, 64, 65, 66, 67, 68, 69, 70, 71, 72, 73, 74, 75, 76]. Some experimental and simulation studies indicate that, even at room temperature, the mica-water interface has ice-like character [59, 77, 78]. In addition, layering of water on top of mica's surface has been observed and could

extend to nanometer range as RH increases [65, 68, 70, 79].

One intriguing aspect of adsorption of vapor onto mica is the effect of the cations on the surface. Muscovite mica is a layered aluminosilicate. Al/Si tetrahedral substitution creates a net negative charge for the structure that is balanced by K^+ cations between the two layers of the Al/Si structure. Mica cleaves most easily along this plane. When cleaved, the newly exposed surfaces are charge-neutral because the K^+ ions are distributed equally between the two exposed surfaces [80]. These surface cations are found to have an impact on the adsorbed water structure, as the water molecules must solvate the exposed K^+ [59]. The K^+ ions are relatively loosely bound on the surface, and thus, can be exchanged for other ions with suitable treatment [60, 81]. For instance, simply rinsing the mica with water exchanges the K^+ ions for H^+. Such an exchange has observable consequences for water adsorption [42, 70, 82, 83]. On K^+-mica, at low RH (< 0.1), strong water adsorption is observed; from RH = 0.1 to 0.7, the adsorption presents a linear behavior followed by rapid layer growth due to the adsorption of bulk-like water molecules at RH >0.7. Only the latter two regimes have been observed for water adsorption on H^+-mica. Computational studies have attributed this behavior to the differences in the hydration of H^+ and K^+ ions [65, 70].

While the cations change the water adsorption behavior, the adsorbed water also affects cation dynamics and structure [60] and further adds to the difficulty of elucidating mica-water interactions. This is illustrated in the inconsistencies in the reported locations of the cations on the mica surface in the presence of water. Some results show that the monovalent ions (e.g. K^+, Li^+, Na^+, and Rb^+) prefer to remain in the cavities [61, 62, 63, 65, 66, 70, 75, 76, 84]. However, some studies have observed these ions at other locations on the surface, or even in the second layer of the adsorbed water [75, 85, 86]. There is a similar disagreement in the literature concerning the locations of divalent ions (*e.g.* Mg^{2+}, Ca^{2+}, and Sr^{2+}), though there is more evidence that the divalent ions may be found away from the surface, in the second layer of the adsorbed water [63, 67, 76, 84, 85, 87].

In this work, we report results probing water adsorption and structure on K^+, H^+, Ca^{2+}, and Mg^{2+} substituted mica surfaces using infrared spectroscopy. Specifically, we investigate the interplay of water and cation interactions to elucidate their effects in governing both water adsorption and cation behavior on mica surfaces. Infrared measurements indicate that while the amount of water adsorbed changes with the cation, the overall hydrogen bonding network of the adsorbed water is the same for a given water coverage. The presence of different ions on the surface causes different adsorption behavior. Stronger interactions between water and divalent ions also affect the spatial and temporal extent of the hydrogen bond networks. Collectively, our results shed light on the role of water-cation interactions in governing water structure

on mica surfaces.

2.2 Methodology

We study the adsorption of water on mica surfaces using Fourier Transform Infrared (FTIR) spectroscopy to probe the macroscopic signatures of the adsorbed water.

2.2.1 FTIR Spectroscopy

We have used FTIR spectroscopy to measure the effect of surface ions on the adsorption of water on mica surfaces, using a Bruker IFS 66 with an indium antimonide detector. Spectra were taken at a resolution of 4 cm^{-1}. The external beam option was used to accommodate the custom-built sample cell. Both the spectrometer and the external sample compartment were purged with dry air to reduce interference of water vapor. To amplify the signal, we used ten sheets of mica (Tarheel Mica Co.) in the sample cell, each separated by thin pieces of aluminum foil, ensuring each of the 20 surfaces were exposed to water vapor. The water vapor pressure over the mica surfaces was controlled through the relative humidity in the sample cell. We varied the relative humidity by mixing streams of dry (dew point $<$ -40 °C) and humid air. Humid air was generated by passing a stream of the dry air across a bath of HPLC grade water (Sigma Aldrich). The flow rate through the sample cell was 1 lpm. The temperature of the sample cell is controlled by circulating cold fluid from a chiller (Julabo CF 15) through the shell. The absorption from a single layer of water adsorbed to mica is exceedingly small.

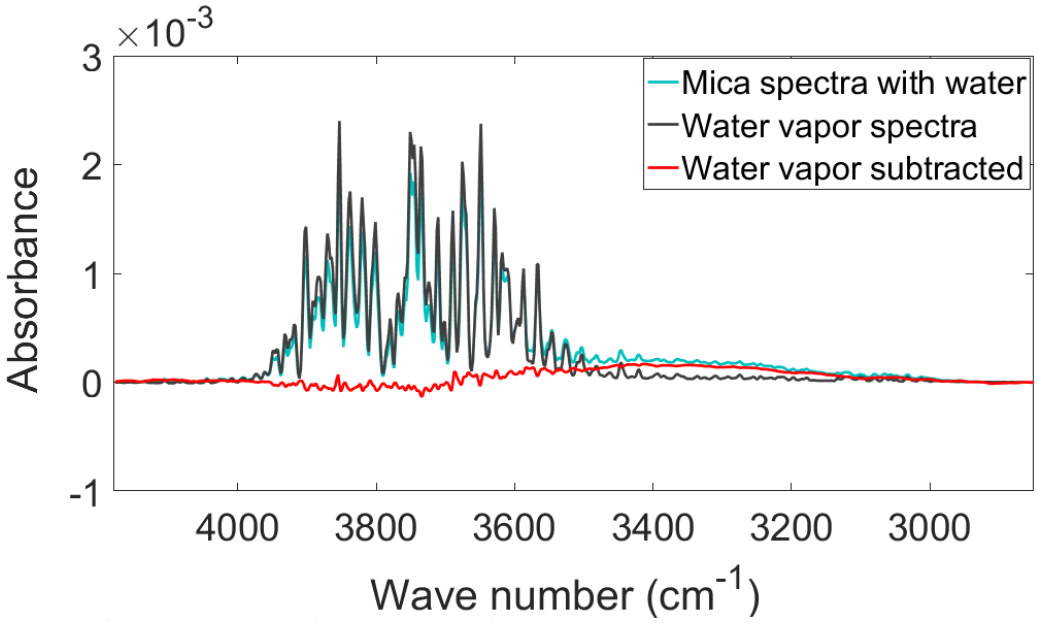

Figure 2.1: Procedure for isolating the absorption features of liquid-like water on mica. A spectrum of only water vapor in the sample cell is subtracted from the sample spectrum, leaving only the signal from adsorbed water.

Temperature and relative humidity in the sample cell are monitored with a hygrometer (Rotronic, Hygroclip HC2 sensor). Our goal is to examine the effect of different ions on the mica surface on the adsorption of water to it. In the data shown below, we have treated mica with HPLC grade water, a saturated $CaSO_4$ solution, and a 0.1M $MgSO_4$ solution to replace the K^+ by H^+, Ca^{2+} and Mg^{2+} ions, respectively [60].

Finally, the spectra are processed as shown in Figure 2.1. The absorption features of liquid-like water can be seen in the region between 3600 and 3000 cm^{-1}, but they are obscured by the absorption of water vapor. To isolate the feature of interest, we subtract a spectrum of water vapor. The result is the red line in Figure 2.1.

2.3 Results and discussion

2.3.1 Measurements using infrared spectroscopy

Figure 2.2 shows our measured spectra of adsorbed water on four different mica surfaces for film thicknesses of 0.125 (left panel) and 0.25 nm (right panel). (Those thicknesses correspond to approximately half a monolayer and a monolayer respectively.) We first note that all of the spectra are quite broad with prominent features at 3390 and 3350 cm^{-1}, respectively. This spectral region, encompassing water's OH symmetric and asymmetric stretching vibrations, is a measure of heterogeneity in the water molecules' local molecular environments [53]. The stretching vibrations for isolated water molecules are responsible for absorption features at 3657 and 3756 cm^{-1}. In the liquid or solid phases, where molecules are coupled, those absorption features collapse into a broad band [88]. (Peak absorption is at 3390 cm^{-1} in the liquid and 3220 cm^{-1} in ice Ih [89].)

The features of the absorption spectra due to a thin film of condensed water are expected to show features of both the bulk phase liquid and ice. At temperatures greater than the melting point, water will be liquid, but the influence of the surface is expected to impose structure. Even hydrophobic surfaces induce a degree of ordering in the adjacent water [90], and mica is known to template adsorbed water into an ice-like structure [53, 54]. Figure 2.2 shows that the spectra for K^+, H^+, Ca^{2+}, and

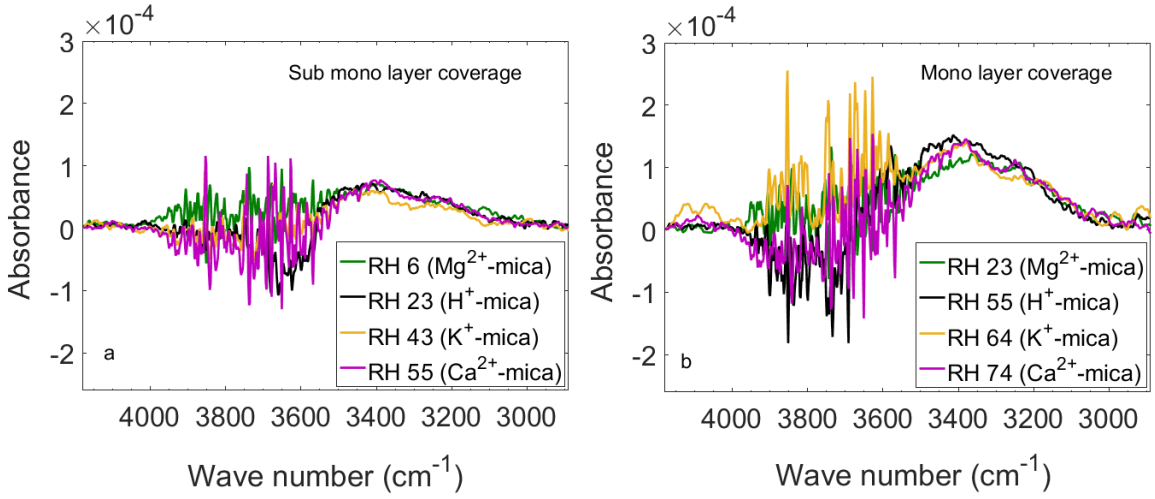

Figure 2.2: Absorption spectra of water adsorbed on K^+, H^+, Ca^{2+}, and Mg^{2+}-mica at room temperature. The spectra shown reflect water adsorbed to 10 mica sheets in the sample cell. The indicated film thicknesses are for water adsorbed on a single surface. The spectra for less than a statistical monolayer, $t = 0.125$ nm are shown on the left; the right panel for is for a coverage of approximately 1 monolayer, $t = 0.25$ nm (t is the film thickness). In both panels, the dominant features of bulk water are present as well as a shouldering near 3350 cm^{-1}, which is an indication of the presence of more strongly hydrogen bonded water on the surface. The chaotic appearance of the region between 4000 and 3600 cm^{-1} is the result of a strong absorption band from mica and a residual water vapor signal.

Mg^{2+} are all broad, with a major peak at approximately 3390 cm^{-1}, and a shoulder at approximately 3350 cm^{-1}, consistent with the ice-like ordering in the adsorbed water.

It is also clear from Figure 2.2 that all of the absorption bands have essentially the same shape for a given film thickness or coverage, indicating that the overall hydrogen bonding environment is similar for all of the surface treatments that we tested. Note, however, that the same film thickness occurs for different values of the

relative humidity, RH. For example, a monolayer coverage is achieved for the Mg^{2+}-mica at an RH value of 23%, whereas the same amount of water is not condensed on a surface of the Ca^{2+}-mica (at the same temperature) until the RH reaches 74%. This is a direct indication of the strength of the interaction between the surface of the mica and the adsorbed water. The difference in the RH required for a monolayer of water on Mg^{2+}-mica vs. Ca^{2+}-mica shows that water has a higher affinity for the Mg^{2+}-mica.

The adsorption isotherms, shown in Figure 2.3, reinforce this point. All of the mica surfaces exhibit a gradual increase in the amount of water adsorbed to them, from 0 to approximately 50% RH. However, for a given RH, the amount of water adsorbed to the Mg^{2+}-mica is greater than any of the others. The figure also shows that, up to 25% RH, the H^+, K^+ and Ca^{2+}-mica isotherms coincide; above this, the H^+-mica isotherm is slightly steeper than the K^+-mica or Ca^{2+}-mica. This is in contrast to the study by Balmer et al.[42], who found less water on H^+-mica at lower RH and no difference between H^+ and K^+-mica at higher RH. (To our knowledge, this is the first measurement of an adsorption isotherm for Ca^{2+} and Mg^{2+}-mica.) The general shape and magnitude of the film thickness is consistent with other studies using FTIR [53], ellipsometry [42, 51] and, simulation [91].

The preceding discussion shows that the strength of the interaction of water with mica changes, depending on the ion on the surface. We show this difference as well as

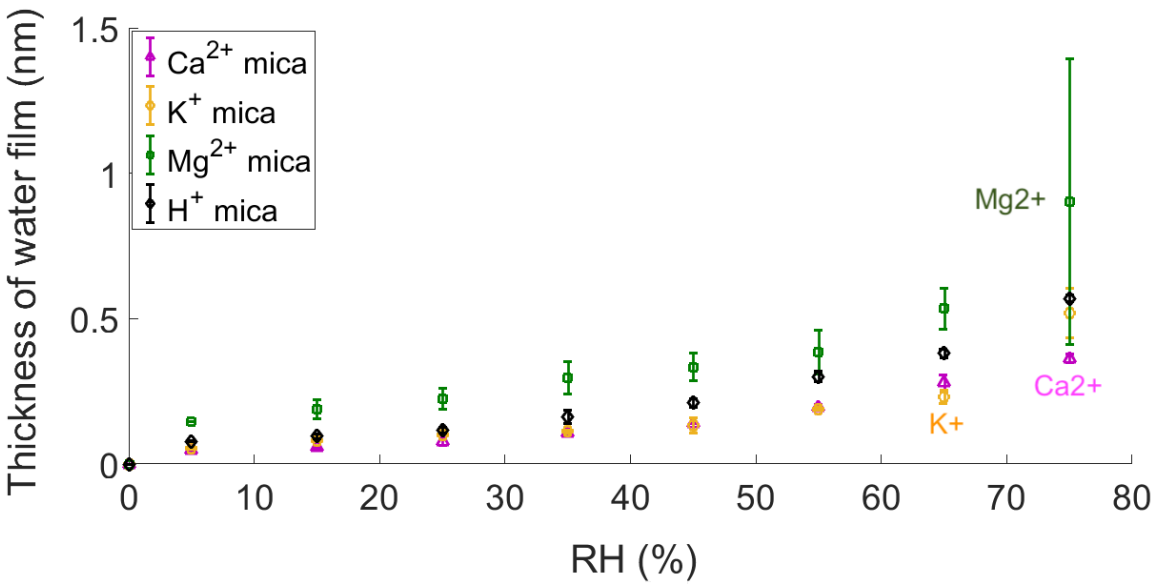

Figure 2.3: Adsorption isotherms of water on K^+, H^+, Ca^{2+}, and Mg^{2+}-mica at 17°C). Isotherms for other temperatures show the same trend.

the change in the strength of interaction with temperature through the relationship [92]

$$\Delta\mu = kT \ln\left(\frac{p}{p_s}\right) \tag{2.1}$$

where the difference in chemical potentials is defined as $\Delta\mu \equiv \mu_v - \mu_{bulk\,water}$. μ is the chemical potential of the vapor or bulk liquid respectively and k is Boltzmann's constant. In the general form, p is the vapor pressure and p_s is the saturation vapor pressure, which we recognize from our previous definition of the relative humidity.

For our measurements, the vapor is in equilibrium with the adsorbed film of water so $\mu_v = \mu_{film}$. With that, Eq. 2.1 becomes

$$\frac{\mu_{film} - \mu_{bulk\,water}}{kT} = \ln(RH) \tag{2.2}$$

In Figure 2.4, we have plotted the absolute value of $\ln(RH)$ as a function of temperature for the Mg^{2+} and K^{+}-mica surfaces for a coverage of approximately 1 monolayer. At 10°C, the difference in chemical potential between a water molecule in the film adsorbed to the Mg^{2+} mica and water in the bulk is nearly 2 kT. Apparently, the Mg^{2+}-mica stabilizes adsorbed water by $2kT$. In contrast, the strength of the interaction between the K^{+} mica and water at 10°C is closer to 0.5 kT. With increasing temperature, the strength of the interaction between the surface of the mica and the adsorbed water weakens. The increase in the strength of interaction between the surfaces and water with decreasing temperature may play a role in mica's ability to catalyze ice formation. While a strong interaction between surface and water may improve templating, it may also contribute to overtemplating, trapping water which is interacting strongly with the surface into a configuration which is not favorable for ice formation.

2.4 Conclusion

The FTIR results collectively indicate that while the strength of interaction between mica and water is dependent on the cation, the overall hydrogen bonding network appears to be similar across the different mica surfaces. In the case of the H^{+}, K^{+} and Ca^{2+}-mica surfaces, changes in the details of the structure of water around the ions do not result in substantial changes in the overall film thickness as a function of RH.

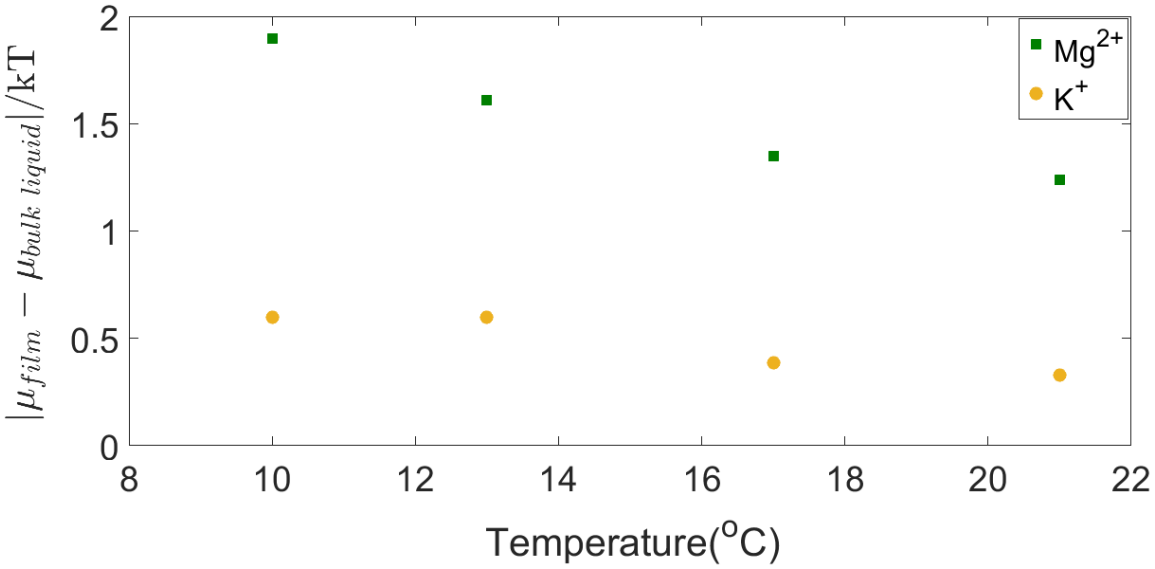

Figure 2.4: Strength of adsorption of water on mica as a function of temperature for the Mg^{2+} and K^{+} mica surfaces.

Chapter 3

Multivalent Surface Cations Enhance Heterogeneous Freezing of Water on Muscovite Mica

[1]

The formation of ice plays a central role in our daily life in areas as disparate as food preservation [93], the global radiation budget [94], and precipitation [95]. For example, the initial formation of ice in mixed phase clouds (*i.e.* both liquid water droplets and ice crystals are present) is governed by heterogeneous ice nucleation [96]

[1]Reprinted (adapted) with permission from Lata, Nurun Nahar, Jiarun Zhou, Pearce Hamilton, Michael Larsen, Sapna Sarupria, and Will Cantrell. "Multivalent Surface Cations Enhance Heterogeneous Freezing of Water on Muscovite Mica." The Journal of Physical Chemistry Letters 11, no. 20 (2020): 8682-8689. Copyright (2020) American Chemical Society. See Appendix A.2 for documentation of permission to republish this material.

and mineral surfaces are one of the dominant sources of atmospheric ice nucleating particles [97]. Numerous laboratory experiments, simulations, and field studies have been conducted to explain the effect of these catalysts on ice nucleation [14, 96, 98, 99, 100].

Despite these efforts, we still have no satisfactory understanding of the microscopic details of ice formation by different surfaces. An open question in this regard is the role of ions on heterogeneous ice nucleation. While recent studies [101, 102, 103, 104] have shown that cations can affect ice nucleation, no clear picture has emerged. This has been hindered due to the other surface properties at play – for example, defects dominate ice nucleation behavior in feldspar making it difficult to delineate ion-specific effects [105]. In other cases [102], the ice nucleation occurred in a diffuse ion layer near a surface, where heterogeneous effects are conflated with the freezing point depression of a solution [106]. We use muscovite mica to avoid such issues, and focus on cation effects on ice nucleation.

Mica offers the advantage that K^+ on the surface can be readily exchanged for other ions [60, 81] without changing other surface characteristics such as roughness. The ability to vary one factor (*i.e.* the ion on the surface) independent of other characteristics of the substrate is unique in ice nucleation research. Further, mica also facilitates comparison between experiment and simulation since when cleaved the basal plane is almost atomistically smooth, reducing the influence of defects [107, 108, 109].

Mica has been established as a rather ineffective ice nucleating agent [30, 110, 111, 112, 113], though in very high concentrations it catalyzes freezing at ≈ -10 °C [114]. The near atomic smoothness of the surface has facilitated studies into the mechanism of freezing via the interaction of water with the substrate, but no definitive conclusions have resulted [115, 116, 117, 118, 119, 120, 121, 122, 123]. In our study, we use a combination of experiments and molecular dynamics (MD) simulations to investigate the role of surface cations on heterogeneous freezing of water. We study K^+, Ca^{2+}, Mg^{2+}, Sr^{2+}, and Al^{3+} – cations that span a range of valency. Our results indicate that multivalent cations lead to enhanced freezing. Our results also show that the size of the ion affects freezing; in this paper we focus on the intertwined effects of valency and the fraction of the surface not covered by ions. Our simulations indicate that ice nucleation near the multivalent ions could be facilitated by the clusters of hydrogen bonded water molecules formed at these surfaces, and anchored (and thus facilitated) by the water molecules in the hydration shell of the cations. These clusters have larger fractions of free water that can adopt ice-like configurations. Such ice-like configurations are promoted by the regions of mica devoid of the cations. These clusters could thus serve as seedbeds for ice nuclei. (We are unable to observe nucleation events on the surface in the simulations because the time scale for nucleation on mica is very long.)

Figure 3.1 shows the heterogeneous freezing rate coefficients, J_{het}, of water on K^+, Mg^{2+}, Ca^{2+}, Sr^{2+}, and Al^{3+}-mica surfaces. The data shown here is for mica from

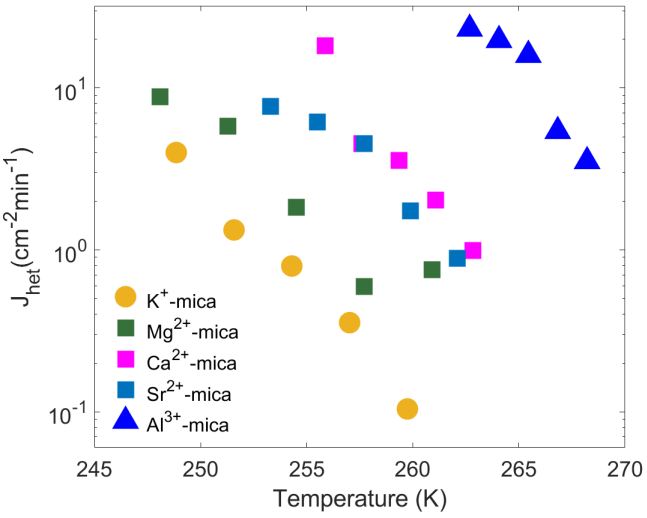

Figure 3.1: Heterogeneous freezing rate coefficients on different ion exposed Ashville micas. Note that the time base is minutes. J_{het} increases with the valency of the exposed ion.

Asheville Mica Co. (A comparison among micas from different suppliers, details of the experimental procedure, and method of calculating J_{het} are in the Supporting information B.1). Clearly, the ion exchange reaction affects ice nucleation on the surface. The freezing curves are shifted to higher temperatures and higher nucleation rate coefficients for the divalent ion exposed surfaces; that trend is amplified further for the trivalent ion exposed surface that we tested. The data for the divalent ions suggest that the size of the ion may be playing a role. We focus on the effect of the ions' charge in this manuscript.

J_{het} is the nucleation rate normalized by the contact area between the droplet and the substrate. We find that water spreads differently on untreated vs. ion exchanged micas. Freshly cleaved mica is a hydrophilic surface. Water deposited onto the

basal plane spreads such that its contact angle is approximately 2° [107, 124]. This behavior changes dramatically upon ion exchange. We quantify this change through measurement of the surface area of a 1 μL droplet deposited onto the mica surface. Results for the micas we tested are shown in Table 3.1. (See B.1 for details.)

On the monovalent ion exposed surface (*i.e.* the K^+-mica), water spreads more than on the divalent and trivalent ion exposed surfaces. The wetting decreases in the order $K^+ > Sr^{2+} > Ca^{2+} > Mg^{2+} > Al^{3+}$. This trend is consistent with observations by Bera et al.[125], who observed a change in the contact angle of droplets of aqueous chloride solutions on mica immersed in alkane. $CaCl_2$, $MgCl_2$ and $BaCl_2$ solutions had the highest contact angles. Solutions with monovalent cations all had smaller contact angles.

Table 3.1
Surface area of a 1 μL droplet on different ion exposed mica surfaces

Exposed ion	Surface area of droplet (cm^2)	Size of ion (Å) [126]	Charge density of ion ($eÅ^{-3}$)
K^+	0.31±0.01	1.38	0.091
Sr^{2+}	0.143± 0.004	1.18	0.291
Ca^{2+}	0.131±0.005	1.00	0.477
Mg^{2+}	0.081±0.004	0.72	1.279
Al^{3+}	0.068±0.003	0.535	4.677

J_{het} and the surface area of the water droplet on different ion exposed mica surfaces can be correlated with the size and charge density of the cations, shown in Table 3.1. Larger cations are associated with a greater surface area of the droplet (*i.e.* the

droplet spreads more) and in a shift of J_{het} to lower temperature. This is also reflected in the correlation with the charge density of the ion. Though we do not have a firm explanation for this behavior, we note that ions with a high charge density are associated with more tightly bound water molecules. Strong adsorption of ions to the mica surface and alteration of the hydration structure of water at the interface is one explanation for the change in the wetting behavior [125].

Why does the ion substitution result in such a dramatic shift in the heterogeneous freezing rate coefficient? Surface roughness, or the presence of defects, can be the dominant factor in heterogeneous nucleation of crystals [127, 128]. Previous work has shown that mica is remarkably smooth [108] and that ion substitution on the surface of mica does not result in an appreciable change in surface roughness [81], but to investigate this possibility more quantitatively, we characterized surface roughness of K^+ and treated micas using atomic force microscopy (AFM).

Our AFM images for K^+- and Mg^{2+}-mica are shown in Figure 3.2. The difference between the highest "peak" to the lowest "valley" in these samples is less than 0.3% of the horizontal extent of the sample. The image makes it clear that the surface treatment did not meaningfully change the surface morphology. The only surface features that are present seem to occur on scales of at least several μm, and comparison between multiple samples shows that the K^+ images are not consistently rougher or smoother on these scales than the images associated with the Mg^{2+} treated surfaces.

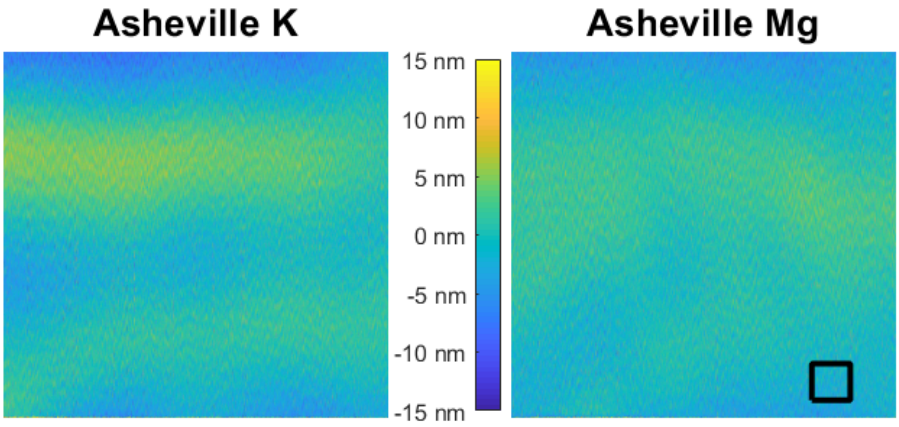

Figure 3.2: False-color AFM images of 10 μm $\times$ 10 μm regions of the surface of an untreated, cleaved muscovite mica surface (left panel) and a sample of the Mg^{2+}-mica (right panel). The black square encompasses a 1 μm $\times$ 1 μm region.

Thus, dependence of freezing rates of cations cannot be explained from surface roughness differences. More quantitative measures of surface roughness (or lack thereof) are described in B.1 and given in Table 3.2.

Table 3.2
RMS roughness measurements for Asheville K^+- and Mg^{2+}-mica samples. Other measures of surface smoothness and the lack of change upon treatment are given in the B.1

Sample	Full Domain (nm)	$(1.25\ \mu m)^2$ Sub-domains (nm)	Box-Filtered Sub-domains (nm)
K^+-mica	2.58	1.24 $\pm$ 0.35	0.68 $\pm$ 0.05
Mg^{2+}-mica	1.86	0.99 $\pm$ 0.16	0.66 $\pm$ 0.03

Having eliminated differences in surface roughness as a cause for the change in J_{het}, we are left with the ions exposed on the surface as the most natural explanation. Ions at or near the surface have been proposed as important aspects of heterogeneous nucleation of ice. In a study of ice nucleation activity of a wide variety of substances,

Shen et al. [114] found that fluorine phlogopite (a fluorine substituted mica) catalyzed freezing at temperatures as high as -1 °C, higher than any of the other substances that they tested, including silver iodide. (Ground muscovite had a characteristic freezing temperature of -5.1 °C in those tests.) They hypothesized that the fluorine ions stabilized water cages on the surface of the mineral, leading to a higher characteristic freezing temperature. This has also been indicated in studies of water on mica surfaces where it has been hypothesized that ice-like water structure is supported on mica. This has mostly been studied when few water layers are adsorbed on the mica surface [77, 120, 129].

The influence of ions on water structure has also been proposed as a mechanism to explain the difference in freezing efficacy between K-feldspar and Na/Ca-feldspars [103]. In that case, the higher ice nucleation activity for K-feldspar is explained in terms of the mobility of water molecules in the vicinity of the ion. Zolles et al. argue that because potassium is larger, with a smaller charge density, it does not restrict and/or disrupt the structure of water as much as sodium or calcium, two other ions that can be present in feldspar; since water is tightly bound to the high charge density ions, it cannot reorient to adopt an ice-like structure, whereas water close to K^+ ions is not as tightly bound and can reorient to adopt an ice-like structure during nucleation. Similar arguments were employed in an attempt to explain the cation effects on ice nucleation observed on polyelectrolyte surfaces [101, 102].

To explore these ideas more completely, we used MD simulations to probe the water structure and dynamics near the mica surfaces with different cations. We performed simulations of water on K^+-mica and Ca^{2+}-mica at 243.5 K (see B.1 for methodological details). Recent simulation studies of heterogeneous ice nucleation [130, 131, 132, 133, 134, 135, 136, 137, 138, 139, 140] have highlighted various factors such as lattice match, water orientation, and water-surface interaction energy to play an important role in catalyzing ice nucleation near surfaces. These studies have also demonstrated that interfacial water structure and dynamics can provide insights into the observed experimental behavior of heterogeneous ice nucleation. For example, our previous studies indicate that orientations of interfacial water molecules in the metastable liquid phase can provide a measure of ice nucleating propensity of a surface [138, 139]. To this end, we calculated the distribution of water dipole orientations in the first few hydration layers. We did not observe any consistent trend, in contrast to those observed near kaolinite and AgI surfaces. This can arise either because of the heterogeneity of the surface coming from the cations or because the mica surfaces do not promote ice nucleation through facilitating ice favorable water orientations.

Nucleation on these surfaces is slow precluding the possibility of observing ice formation in the simulations. For example, the nucleation on kaolinite is $\sim$1000 times faster than on mica [141, 142]. At extreme supercooling, ice nucleation on kaolinite is observed in several hundred nanoseconds in straightforward MD simulations [136, 139, 143]. This implies we would require several hundred microsecond long

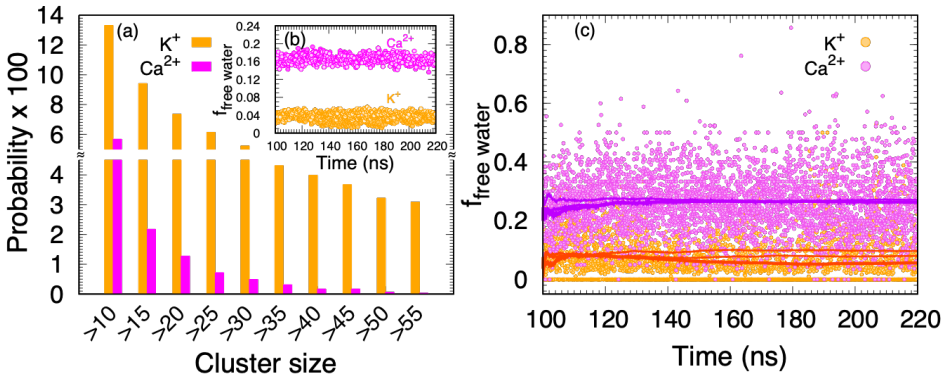

Figure 3.3: Panel (a): Probability of observing clusters greater than a given size on the surface of Ca^{2+}-mica and K^{+}-mica. The data corresponds to cutoff of 80% and observation window of 2 ns for determining hydrogen bonded water molecules. See B.1 for more details. Panel (b): Fraction of free water ($f_{freewater}$) within 0.8 nm of the surface as a function of time. Panel (c): Fraction of free water in the largest cluster identified on Ca^{2+}-mica and K^{+}-mica surfaces as a function of time. The solid lines indicate the running averages for the three runs performed for each surface. The points represent data from one of the runs. The appearance of line at 0 is just the points at $f_{freewater}$=0, and not a running average.

simulations to observe one nucleation event on mica. Due to limited statistics of ice-like clusters, we instead focus on clusters of hydrogen bonded water molecules on the various surfaces. We hypothesize that formation of such clusters could facilitate the birth of ice nuclei. To eliminate the effect of thermal fluctuations on our cluster determination, we evaluate the clusters based on hydrogen bonds that exist for more than 80% of the times within a 2 ns observation window of the simulation. Note that in this criterion the hydrogen bonds can break and re-form but need to exist for at least 80% of the observation window (similar to the history-independent hydrogen bonds described in Ref.[144]). Thus, we eliminate the bonds that might break or form for short periods of time through thermal fluctuations [144]. Geometric criteria

of O-O distance less than 0.35 nm and the O_{donor}-H_{donor}-$O_{acceptor}$ bond angle greater than 110° [145] were used to identify hydrogen bonds between water molecules. Only the interfacial water molecules (within 0.8 nm of the surface) were considered for this analysis. Clusters were identified using Cytoscope network analysis software [146] after the hydrogen bonded water molecules were identified. Results presented here are averaged over ten 2 ns observation windows from 200 ns long MD simulations. We tested the effect of the length of observation windows (0.5, 1, 2, and 5 ns) and the cutoff values for hydrogen bond existence (70%, 80% and 90%) on the distribution of the cluster sizes. These parameters change the probability of observing various cluster sizes but the relative trend between the different cations remains the same. Thus, the discussion provided here does not change with these parameters. Further details of the calculations and parameter sensitivity analysis are provided in the B.1.

The distributions of the cluster sizes are shown in Figure 3.3. Interestingly we find that larger clusters are more likely to form in case of K^+-mica compared to Ca^{2+}-mica. For instance, the probability of observing cluster sizes >45 water molecules is ∼0.002 for Ca^{2+}-mica while it is ∼0.036 in case of K^+-mica. This indicates that hydrogen bonded clusters alone are insufficient to explain the experimental observations. It has been argued that ions hinder ice nucleation because the tightly bound water molecules in their hydration shells cannot orient to give ice-like configurations [103]. Thus, we calculated the fraction of free water in the interfacial region, as well as in the clusters of hydrogen bonded water molecules, where free water is defined as those

water molecules that do not belong to the first or second hydration layer of the ions. The bounds of the first and second hydration layers were determined from the ion-water radial distribution functions obtained from simulations of single ions in water (see B.1). The amount of free water in the interfacial region (Figure 3.3(b)) is higher in case of Ca^{2+}-mica than K^{+}-mica. Furthermore, the fraction of free water in the hydrogen bonded clusters is also consistently higher for Ca^{2+}-mica (Figure 3.3(c)).

To evaluate this trend across valency, we performed simulations of hypothetical ions – K^{2+}, K^{3+}, Ca^{+} and Ca^{3+}. The choice was guided by two reasons – Firstly, no well-calibrated force field parameters are available for Al^{3+} on mica. Thus, we did not perform simulations of Al^{3+}-mica. Secondly, simulations of the hypothetical ions provide insights into the effect of charge on water structure (and cluster formation) while the size of the ions is unchanged. Results for $Ca^{i+}, i = 1, 2, 3$ are shown in Fig. 3.4(a) (see SI for results for $K^{i+}, i = 1, 2, 3$ mica, Fig. B.10). We observe that the probability of observing large clusters of hydrogen bonded water molecules increases with the charge. In addition, the fraction of free water in the interfacial region as well as fraction of free water in the hydrogen bonded clusters increases with the valency of the cation. In fact, the fraction of free water is <0.2 in case of Ca^{+} but increases to >0.6 for Ca^{3+}. Snapshots illustrate that the hydration shell water molecules act as anchors for the formation of large clusters. Based on our observations, we surmise that the slow dynamics of the water molecules in the hydration shell of the higher valency ions [147, 148] contributes to the longer lasting hydrogen bonds and facilitates

the formation of larger networks of water molecules. The higher valency also results in larger fraction of free water which will have faster reorientation times than hydration shell water molecules, enabling them to adopt ice-like conformations. Thus, these clusters could serve as seedbeds for ice nuclei. The trends observed suggest that Al^{3+}-mica would have clusters of hydrogen bonded water molecules with greater fraction of free water. Based on our hypothesis, this would result in a higher ice nucleation rate near Al^{3+}-mica relative to Ca^{2+}- and K^{+}-mica, as observed in the experiments. We note that K^{+}-mica does not follow this trend, indicating that other factors beyond valency might be at play. This will be probed in future work.

We further analyzed whether ice-like structures were observed in the clusters described above. We used tetrahedrality-based criterion [149, 150] to identify ice-like clusters (see SI (B.1) for further discussion). We found clusters of ice-like water molecules originating from the hydrogen bonded clusters providing further support to our hypothesis. Stricter criteria for identifying ice-like molecules, like that used in a recently developed PointNet based method [151], also found ice-like particles in the hydrogen bonded clusters (see Figure B.12). Lastly, we performed microsecond long simulations of 3×3 nm^2 surface for Ca^{2+}- and Ca^{3+}-mica. Larger clusters of ice-like particles consistently form on Ca^{3+}-mica relative to Ca^{2+}-mica (see Figure B.11).

What promotes the larger clusters of hydrogen bonded water molecules on surfaces with higher valency cations? It can be surmised that the regions on the mica surface

without ions promotes these clusters. To investigate this we created surfaces where the ions were shifted to limited section of the surface (see Figure B.13), thereby creating a large region of mica surface devoid of cations. We performed simulations of water at 243.5 K on these surfaces. We observed that large clusters of hydrogen bonded water molecules, and large clusters of ice-like particles formed on these surfaces. The clusters were primarily located in the region devoid of ions on the mica surface (Figures B.14 and B.15). This suggests that the regions of mica surface without ions could promote the clusters and ice-like configurations.

Based on the simulation results presented here we propose the following mechanism through which ions can enhance heterogeneous ice nucleation – the water molecules in the hydration shell of the ions provide anchoring for the formation of large clusters of hydrogen bonded water molecules in the interfacial region. With increasing valency, the fraction of free water (i.e. not belonging to the first or second hydration shell of the ions) increases in these clusters. This allows them to adopt ice-like conformations which are facilitated by the regions on mica surface devoid of ions, and could enhance the likelihood of the appearance of ice nuclei. Indeed, previous studies indicate that nucleation can proceed through large clusters with low crystallinity as well as small clusters with high crystallinity [152, 153, 154, 155]. The former scenario appears to be enhanced on the mica surface. Investigations combining the MD simulations presented here with enhanced sampling techniques like forward flux sampling [156, 157, 158, 159], and transition interface sampling [160, 161] are currently underway to

further explore this hypothesis. While our focus is primarily on the effect of valency on ice nucleation on mica, some additional observations are noteworthy. Within the divalent ions we observe that Mg^{2+}-mica has lower J_{het} than Ca^{2+}- and Sr^{2+}-mica. In simulations, K^{+}-mica has larger clusters of hydrogen bonded water molecules than K^{2+}- and K^{3+}-mica. These observations suggest that other factors such as ion size can also affect ice nucleation.

In summary, by taking advantage of ion exchange on a near defect-free mica surface, we study the effect of cations on heterogeneous ice nucleation. Our experiments show that mica surfaces with a multivalent cation exposed on the surface are better ice nucleators, in the order $Al^{3+} > Ca^{2+} \simeq Sr^{2+} > Mg^{2+} > K^{+}$. The data show that the size of the exposed ion affects the nucleation rate; here we have focused on the linked effects of valency and fraction of the silica surface exposed to water. Simulations show that the multivalent ions on the surface are associated with clusters of hydrogen bonded water molecules anchored by the ions, and with higher fraction of free water. To our knowledge, this is the first study to show such a clear correlation in both experiment and simulation for a naturally occurring substrate. These are also the first experiments to show unambiguously that multivalent cations on a surface promote ice nucleation; our simulations of this motivate a new mechanism for ice nucleation wherein the hydration shells of the ions anchor large hydrogen bonded water clusters with high fraction of free water which can adopt ice-like configurations promoted by the underlying regions of mica surface devoid of ions. These clusters could be

precursors to the critical ice embryo. The studies have implications in understanding the role of ions in heterogeneous ice nucleation relevant to atmospheric chemistry as well as for design of anti-icing surfaces.

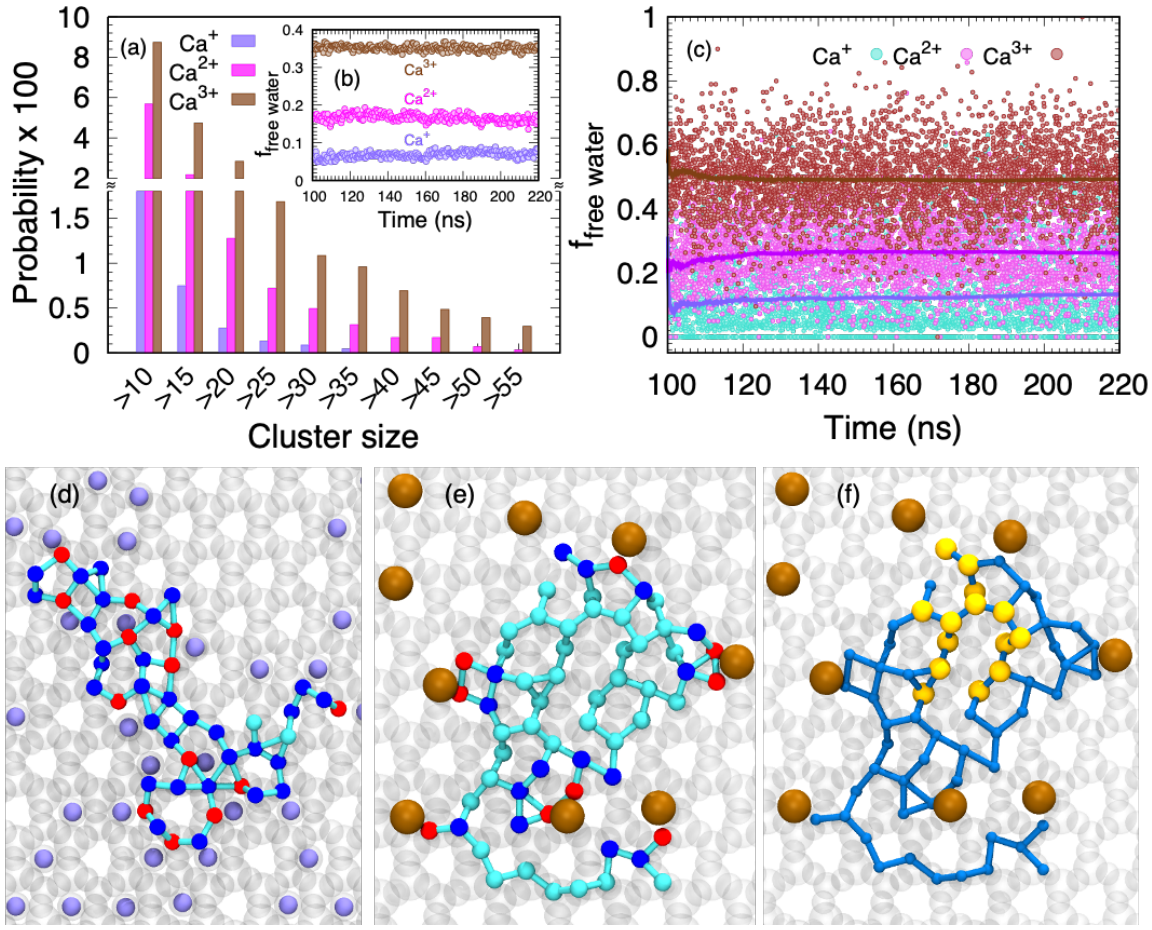

Figure 3.4: Panel (a): Probability of observing clusters greater than a given size on the surface of Ca-mica with various charges. The data presented here uses the cutoff of 80% and observation window of 2 ns for determining hydrogen bonded water molecules. Panel (b): Fraction of free water within 0.8 nm of the mica surface. Panel (c): Fraction of free water in the largest cluster of hydrogen bonded water molecules. The solid lines indicate the running average. Panel (d): Snapshot of a largest cluster identified on Ca^{+}-surface. Panel (e): Snapshot of a largest cluster identified on Ca^{3+}-surface. Panel (f): The same cluster as panel (e) with the ice-like water molecules marked using yellow spheres. Color code: gray: mica surfaces, slate blue: Ca^{+} ions, sienna: Ca^{3+} ions. Water molecules are shown as spheres, red: in ion first hydration shell, blue: in second hydration shell, cyan: free water, and yellow: ice-like water.

Chapter 4

Aerosol Composition, Mixing State and Phase State of Free Tropospheric Particles and Their Role in Ice Cloud Formation

[1]

[1]Reprinted (adapted) with permission from Lata, Nurun Nahar, Bo Zhang, Simeon Schum, Lynn Mazzoleni, Rhenton Brimberry, Matthew A. Marcus, Will H. Cantrell, Paulo Fialho, Claudio Mazzoleni, and Swarup China. "Aerosol Composition, Mixing State, and Phase State of Free Tropospheric Particles and Their Role in Ice Cloud Formation." ACS Earth and Space Chemistry (2021). Copyright (2021) American Chemical Society. See Appendix A.3 for documentation of permission to republish this material.

4.1 INTRODUCTION

Atmospheric ice nucleation (IN) plays a crucial role in regulating cloud properties such as lifetime, radiative forcing, and electrification, affecting the hydrological cycle, precipitation, and the climate system [98]. Only a small fraction (e.g., one out of 10^5 to 10^6 particles) of atmospheric aerosol particles can serve as ice nucleating particles (INPs) [14, 15, 16, 17]. However, diverse physicochemical characteristics of the INPs and complex atmospheric interactions make it challenging to accurately model heterogeneous IN processes [12, 162, 163].

Recent studies suggest that free tropospheric particles can affect the properties of high-altitude clouds in the Northern Hemisphere by acting as INPs [164, 165, 166]. Previous high-altitude studies highlighted the heterogeneity of the composition of INPs in the upper troposphere [167, 168, 169]. For example, a study from tropical cumulus clouds over the Atlantic Ocean found that dust particles transported from the Sahara desert acted as INPs [170]. Observations from low-level mixed-phase clouds at the Jungfraujoch observatory (3580 m a.s.l.) in Switzerland showed a considerable fraction ($\sim$ 27%) of soot and biomass burning particles in ice residuals [165]. In contrast, another study found biomass burning soot to be a minor fraction of INPs [167, 168, 169, 170, 171]. The INPs heterogeneity appeared to be evident also from a previous analysis of samples collected at the Observatory of Mountain Pico (OMP) at 2225 m a.s.l. in the North Atlantic Ocean, with INPs mostly being constituted by

a mixture of dust, aged sea salt, and soot coated with organic material [164].

Atmospheric particles are complex mixtures of chemical compounds [172, 173]. The physicochemical properties of mixed aerosol particles are evolve during transport due to the aging process [174, 175], chemical modifications [176, 177], and coagulation [178] imparting additional complexity to the atmospheric aerosol [179, 180]. The internal mixing state represents the distribution of different chemical elements in single particles across a population. It may play a vital role in determining the IN activity of atmospheric particles [34, 181, 182], where the IN activity is defined as the potential of a particle to nucleate ice. Limited studies addressed the effect of internal mixing state on IN, especially for free-tropospheric aged particles that are transported over long distances [183, 184]. Therefore, a comprehensive analysis of individual particles is crucial to understand the effect of the mixing state on the properties of INPs in the atmosphere. A recent study highlighted that frequent new particle formation and subsequent growth of these particles can take place in the remote marine boundary layer (MBL) following the passage of cold fronts [185]. These particles further can participate in warm and cold cloud formation.

Laboratory and field investigations have shown that the IN activity is affected (often reduced) by different coatings on preexisting particles, for example, organic, sulfate, or nitrate coating [33]. In particular, organic matter is a common type of aerosol found in the atmosphere [186], but its effect on IN is poorly understood because its

abundance in INPs has been confirmed only using advanced analytical techniques [186, 187, 188, 189]. The reduction of INP activity is believed to be caused by reducing the availability of IN active sites or changing the water activity of the core particle [189, 190, 191]. Conversely, some coating materials are found to enhance IN activity [192, 193]. For example, several studies reported the significant potential of organic aerosol to act as INPs, although not as efficiently as mineral dust particles [190, 192, 194, 195, 196]. The ubiquity of organic matter in a photochemically active environment affects the IN properties of aerosol by influencing their phase state (liquid to solid) and morphology [29, 194, 197, 198]. The phase of organic aerosol affects the IN activity and the pathway to form ice. It is widely accepted that INPs contain insoluble and/or solid substrates that aid in the formation of ice crystals [199]. Several studies demonstrated that some organic aerosols could exist as amorphous glasses or semi-solids at colder temperatures because the diffusion rate of water is much slower at colder temperature [200, 201, 202]. These aerosols can be more ice active at colder temperatures by providing solid surfaces that facilitate ice formation via deposition IN (DIN) [203, 204]. Phase transition for complex organic matter/inorganic (INO) mixture particles is not well understood and further complicates understanding their role on IN activities [189]. Therefore, it is necessary to further investigate the IN potential of aged ambient organic aerosols.

In this study, we elucidate the physicochemical properties of free-tropospheric particles that are transported over long distances to the high elevation of the OMP and

their effects on the IN activity. We investigated particles collected in three events with different transport patterns during the summer of 2014. We probed size-resolved chemical composition, phase state, and mixing state of free tropospheric aerosol and INP populations (over 23,000 particles) and investigated the IN ability of collected particles in simulated mixed-phase and cirrus cloud conditions. Though a previous OMP study the IN activity and provided some hints of particle population, [164], the detailed size-resolved composition and phase state of individual particles are missing, which warrants further investigation of the physicochemical properties of the OMP particles and their effect on ice cloud formation. Furthermore, this study utilizes an IN environmental scanning electron microscope, which enables us to directly observe IN on individually internally mixed particles at mixed and cirrus cloud conditions.

4.2 MATERIALS AND METHODS

4.2.1 Sampling Site and Measurements

Aerosol particles were collected during June-July 2014 at the OMP, situated in the summit caldera of Pico Mountain at 2225 m above mean sea level on Pico Island in the Azores archipelago in the North Atlantic. The OMP is typically above the MBL; therefore, samples collected at the site often contain particles transported over long distances in the free troposphere. Table B.2 shows the sampling time and conditions. Samples from three events were selected named SA1, SA2, and SA3. The samples were selected based on the particle loading on the substrates and the back trajectory

analysis to identify specific events. Particles were collected on silicon nitride coated disks and carbon B-type TEM grids (TedPella, Inc), on the third stage of a four-stage cascade impactor (MPS-4G1) with a 50% collection efficiency between the size ranges of 0.50 and 0.15 μm. The particle samples were stored at room temperature in the sample storage box. The storage box was wrapped with aluminum foil and parafilm to avoid the interaction of the samples with light and moisture. Bulk samples were collected on quartz filters using high volume samplers (Ecotech HiVol 3000) equipped with a PM2.5 cascade impactor [174] for quantification of organic carbon (OC) using an EC-OC analyzer (Sunset Laboratory Inc., Model 4), and for quantification of common cations and anions using an integrated ion chromatography system (Thermo Scientific ICS-1100/ICS-2100). A two-channel optical particle counter (50% cutoff diameters > 0.3 μm and > 0.4 μm) was deployed to monitor the number concentration of particles.

To understand the origin and transport pattern of the air masses arriving at Pico Mountain, we performed backward mode simulations of the Lagrangian Flexible Particle (FLEXPART) dispersion model [205, 206, 207]. The details of the FLEXPART simulations are reported in the Supporting Information B.2. The matrices of residence time were integrated over time and altitude to indicate the transport pattern (e.g., Figure 4.1). We estimated the CO contributions from anthropogenic and wildfire sources and air mass origins and ages [208]. The air mass ages were calculated from the average time of CO transported in FLEXPART. Details of the FLEXPART

products and applications can be found in previous work [208, 209].

4.2.2 Chemical Imaging and Single Particle Analysis

The chemical composition, morphology, size, and mixing state of the particles were probed using a computer-controlled scanning electron microscope system (CCSEM) coupled with an energy-dispersive X-ray (EDX) spectrometer [210]. We note that the SEM-derived 2D projected geometric diameter may differ from the aerodynamic diameter of the impactor. In this study, C, N, O, Na, Mg, Al, Si, P, S, Cl, K, Ca, Mn, Fe, and Zn were considered in the X-ray analysis. Particles were then classified into eight different classes such as "Na-rich", "Na-rich/sulfate", "sulfate", "carbonaceous", "uncoated dust", "carbonaceous coated dust", "sulfate coated dust", and "other" based on the atomic percentages using the particle classification scheme shown in Figure B.16. The aspect ratio of the particles from the tilted view of SEM images and the surface area of the particles was measured using ImageJ software. We note that tilted view imaging was performed under low-pressure condition ($\sim 2 \times 10^{-6}$ Torr), which can result in loss of volatile and semivolatile materials. In addition, temperature and dry condition inside the ESEM chamber may affect the particle's phase. These caveats need to consider while interpreting the results.

We characterized the carbon feature of the particles using scanning transmission X-ray microscopy coupled with near edge X-ray absorption and fine structure spectroscopy (STXM/NEXAFS) (beamline 5.3.2.2) located in the Advanced Light Source

at Lawrence Berkeley National Laboratory collected at 111 energies around the carbon K-edge. STXM/NEXAFS was conducted on a subset of particles analyzed on CCSEM/EDX. STXM/NEXAFS provides information about different types of internally mixed particles like OC where the organic mass is homogeneously distributed throughout the entire particle, EC mixed with OC (EC+OC) where particles possess soot-like properties (higher C=C, sp^2 hybridized bonds) along with organic functionalities, OC infused with inorganics (INO+OC), and particles containing mixtures of OC, EC, and INO inclusion (OC+EC+INO) [196, 211]. The organic nature of a particle containing OC+INO, OC+INO+EC, and EC+OC components can be revealed from organic volume fraction (OVF) maps [212, 213].

4.2.3 Ice Nucleation Experiments and INP Identification

The IN experiments were performed using a custom-made temperature and humidity-controlled cryo-stage that is accommodated within an environmental scanning electron microscope (IN-ESEM). The environmental scanning electron microscopy (IN-ESEM) platform is described in detail elsewhere [214]. IN experiments were performed under isobaric (constant dew point temperature, T_d) as well as isothermal conditions, meaning constant particle/substrate temperature (T_p). The pressure in ESEM during experiments ranges between 10 and 600 Pa. This study used a cooling rate of 0.1-0.2 K min^{-1}, comparable to rates reported for cirrus clouds at mid and low-latitudes [215]. The ESEM images were recorded every 3 seconds. Isothermal conditions (constant T_p while increasing water vapor partial pressure) were used during experiments

at higher magnification, focusing on one region to detect single particle freezing events by looking at the growth and shape of the forming crystal. During isothermal experiments, water vapor partial pressure was increased from 10 Pa at a rate of 15 Pa min^{-1} [214]. The identification of INPs after ice crystal formation was performed by warming the sample at a rate of 1 K min^{-1}. The images were recorded until the ice crystals were completely sublimated and only the residual INPs remained. The identified INPs were then characterized utilizing SEM/EDX.

4.3 RESULTS AND DISCUSSION

4.3.1 Airmass back trajectories and origin

Representative FLEXPART trajectories show column integrated horizontal residence time distributions from the surface to 15,000 m a.s.l.,(Figure 4.1, left panel). The right panel shows vertical distributions of the FLEXPART simulated residence times at given upwind times. The air masses for SA1 (Figure 4.1(a-b)) were mostly from Eastern U.S. and reached OMP approximately after 14 days. The transport of SA2 was impacted by air masses from Africa that circulated over the North Atlantic Ocean (Figure B.17). During the upwind days, the air masses traveled at different altitudes before reaching OMP. The SA3 air masses were mostly originated from North America and recirculated over the North Atlantic. Air masses during sampling of SA1 and SA3 traveled at higher altitudes compared to air masses during SA2. Plume ages (Table B.2) were similar ($\sim$ 16 days) for three events. The MBL height during each of

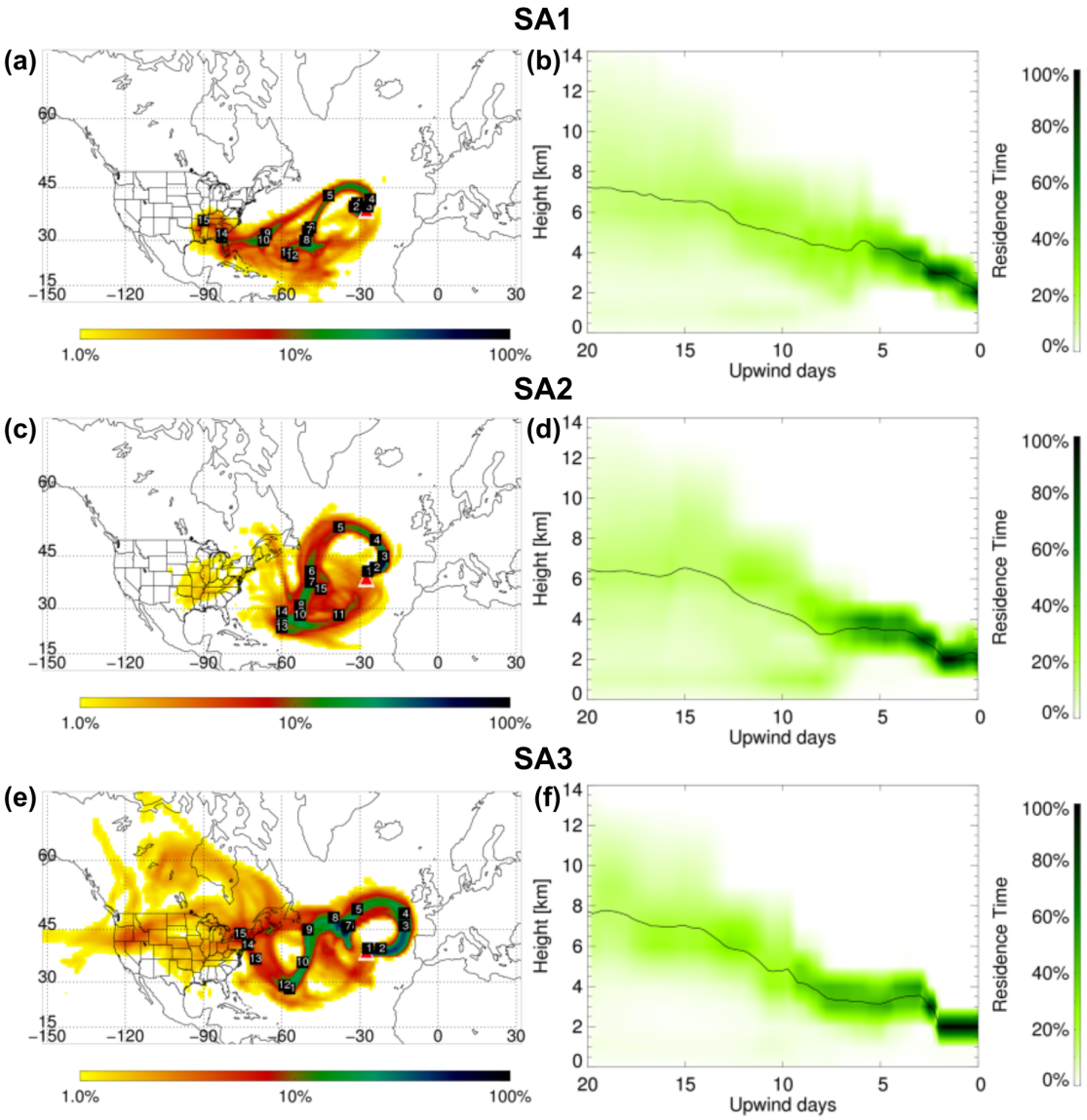

Figure 4.1: FLEXPART simulated air parcel residence time for July 4, 2014 [SA1, (a,b)]; July 10, 2014 [SA2, (c,d)]; and July 12, 2014 [SA3, (e,f)]. (a,c,e) Residence time integrated over the vertical column for 20 days of transport time. Residence time is color-coded by logarithmic grades representing its ratio to the location of maximal integrated residence time (100 %) (a,c,e). The white labels indicate the approximate locations of the center of the plumes on given transport days. (b,d,f) Vertical distribution of the residence time at given upwind times. The black lines in (b,d,f) show the mean height of the plume during transport.

the sampling period was estimated from FLEXPART/Global Forecast System (GFS) data. MBL height of 577, 911, and 863 m was observed for sample SA1, SA2, and SA3, respectively.

4.3.2 Micro-spectroscopic Analysis of Individual Particles

The size-resolved chemical composition using CCSEM/EDX (Figure 4.2(a) and 4.2(c)) shows SA1 and SA3 were dominated by carbonaceous particles with a size ranging from 0.1 to 0.5 μm, whereas SA2 (Figure 4.2(b)) was dominated by larger carbonaceous particles ranging from 0.1 to 1 μm. The larger size bin (>0.5 μm) of SA1 and SA3 was dominated by sulfate, coated dust, uncoated dust, and sulfate, respectively, whereas for SA2, Na-rich particles were dominant. Figure 4.2(d) shows the normalized contribution of the particle classes for each sample where the variety of chemical composition becomes clear and shows a high number fraction of carbonaceous aerosol, specifically 68%, 57%, and 67% for SA1, SA2, and SA3, respectively. Other than carbonaceous aerosol, SA1 and SA3 contain a higher percent of sulfate ($\sim$14 and 23%, respectively), suggesting potential cloud processing of aerosol during transport [216]. The back trajectory analysis also shows the air masses for these samples traveled at higher altitudes during upwind days before reaching the OMP (Figure 4.1(b) & 4.1(d)). The dust particles ($\sim$11%) in SA1 may have been transported from dust storms in Africa, as suggested by FLEXPART (Figure 4.1(b)). The higher percent of Na-rich particles ($\sim$23%) in SA2 may have been due to entrainment from the marine boundary layer during transport. Both the bulk chemical analysis

from ion chromatography (Figure B.18) and the size-resolved chemical composition obtained from CCSEM/EDX indicate that SA1 and SA3 are richer in carbonaceous and sulfate material.

Figure 4.2(e) illustrates the mixing state obtained from STXM/NEXAFS. SA1 contained the highest number fraction of OC+INO followed by SA2 and SA3, respectively. Contrarily, we observed the highest number fraction of OC+EC+INO and OC+EC in SA3 followed by SA2 and SA1, respectively. The presence of relatively higher OC+EC-containing particles in SA3 suggests that SA3 was more affected by biomass burning than the other two samples. Similarly, FLEXPART CO source apportionment suggests this sample was influenced by fires (Figure B.19). All the OC particles present in SA1 were internally mixed with INO and EC, whereas SA2 and SA3 contained major fractions of OC particles internally mixed with INO and EC and a small fraction of OC (0.5-1.3%) as single species. We also observed a size-dependent mixing state class of the particles from STXM/NEXAFS (Figure B.20). OC + INO dominate at almost all the size bins ($0.15 - 0.5$ μm) in the case of SA1. In contrast, OC + EC + INO particles dominate at almost all size ranges. In addition, we calculated the mixing state index (χ), average particle diversity (D_α), and bulk particle diversity (D_γ) from the CCSEM/EDX data [217]. The detail of mixing state calculation is reported in Supporting Information B.2. D_α measures the average species diversity within a single particle, D_γ measures the overall diversity in the bulk population, χ measures the degree to which the particle population is externally

mixed (χ= 0% versus internally mixed (χ= 100%) [218]. At least 10000 particles are

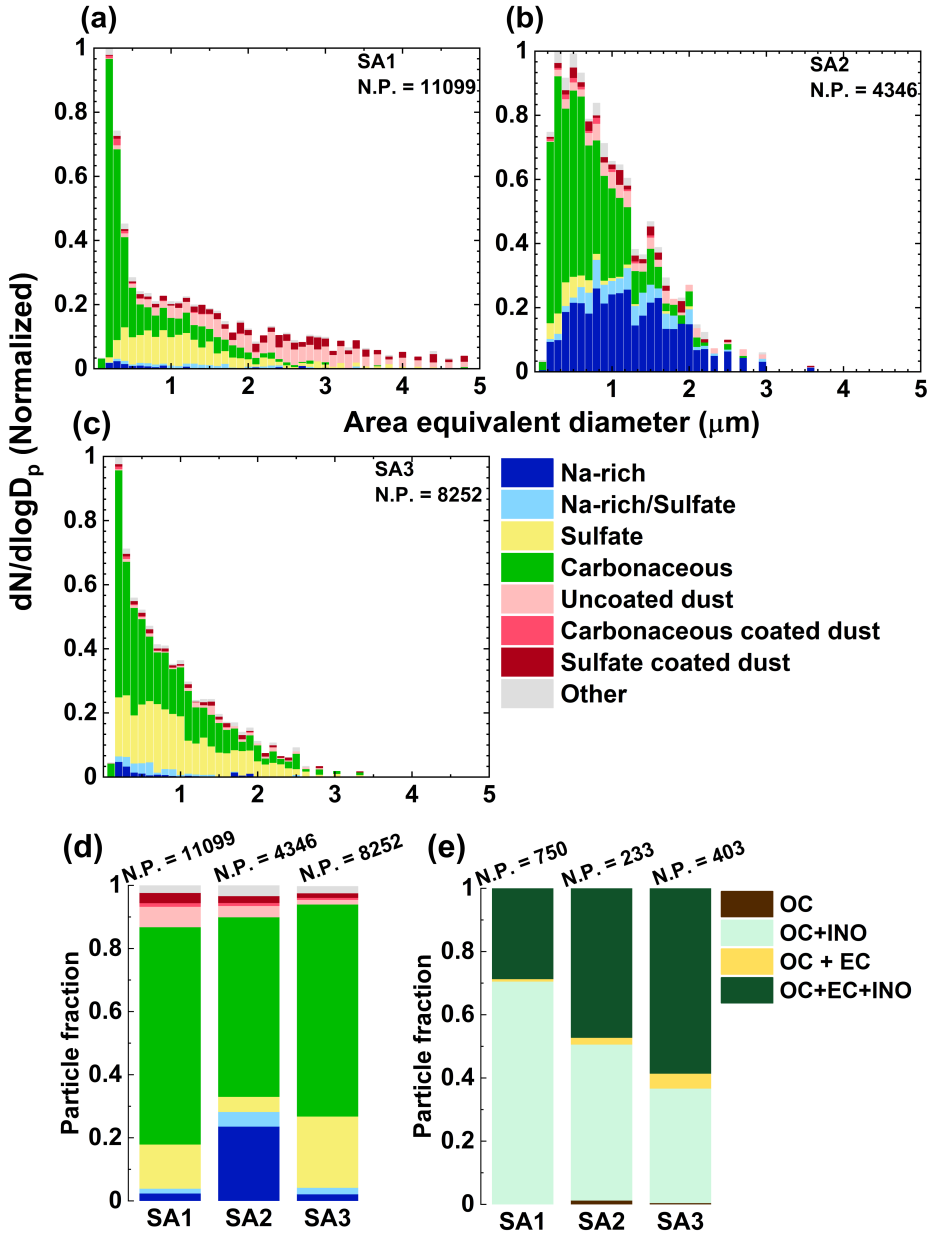

Figure 4.2: Panels (a-c) show size-resolved particle classes obtained from CCSEM/EDX; (d) shows the number fraction of particle classes. N.P. stands for the number of particles analyzed; (e) shows the particle classes obtained from the STXM/NEXAFS where the particles are classified by different combinations of organic carbon (OC) and other internally mixed components such as inorganic (INO) and elemental carbon (EC).

necessary to determine χ within 10% confidence interval [219]. Here, ∼4000-11000 particles (for different samples) were used to calculate χ. Figure B.21 shows D_γ as a function of D_α with lines indicating different χ values; χ lies between 60 to 65% suggesting that a significant fraction of the particles were internally mixed during all three events.

Figure 4.3(a-c) shows spatially resolved STXM/NEXAFS spectra of representative internally mixed particles. Carbon speciation maps (C-maps) are shown on the right of each spectrum; green, red, and cyan indicate organic-rich, elemental carbon-rich, and inorganic-rich areas, respectively. We selected representative types of particles based on the organic volume fraction (OVF). From the C-maps, we observed heterogeneous distributions of organic and inorganic components. Different functional groups absorb at specific energies with overlaps between different carbon transition energies; we performed spectral deconvolution Figure B.22 to determine the relative contribution from each of the observed functional groups [210, 220]. Details regarding the functional group estimates are discussed in the B.2 and fit parameters are reported in Table B.3. Figure 4.3(d-f) shows the relative contribution obtained from each of the spectra. We observed variations of relative contributions of each carbon functionalities. Particles contain a substantial percentage of C=C (285.1 eV), C=O (286.6 eV), COOH (288.6 eV), C-OH (289.5 eV), and C-H (287.7 eV) functionality. The majority of the particles observed in SA1 contain a higher percent of C=C, C-H, COOH functionality, whereas SA2 and SA3 contain a higher percent of C-H,

COOH, and C-OH functionality. The contribution of different C-functionalities affects the particle viscosity, following a decreasing trend from carboxylic acid (COOH) ∼ hydroxyl (OH) > nitrate (ONO2) > carbonyl (CO) > methylene (CH2) [221].

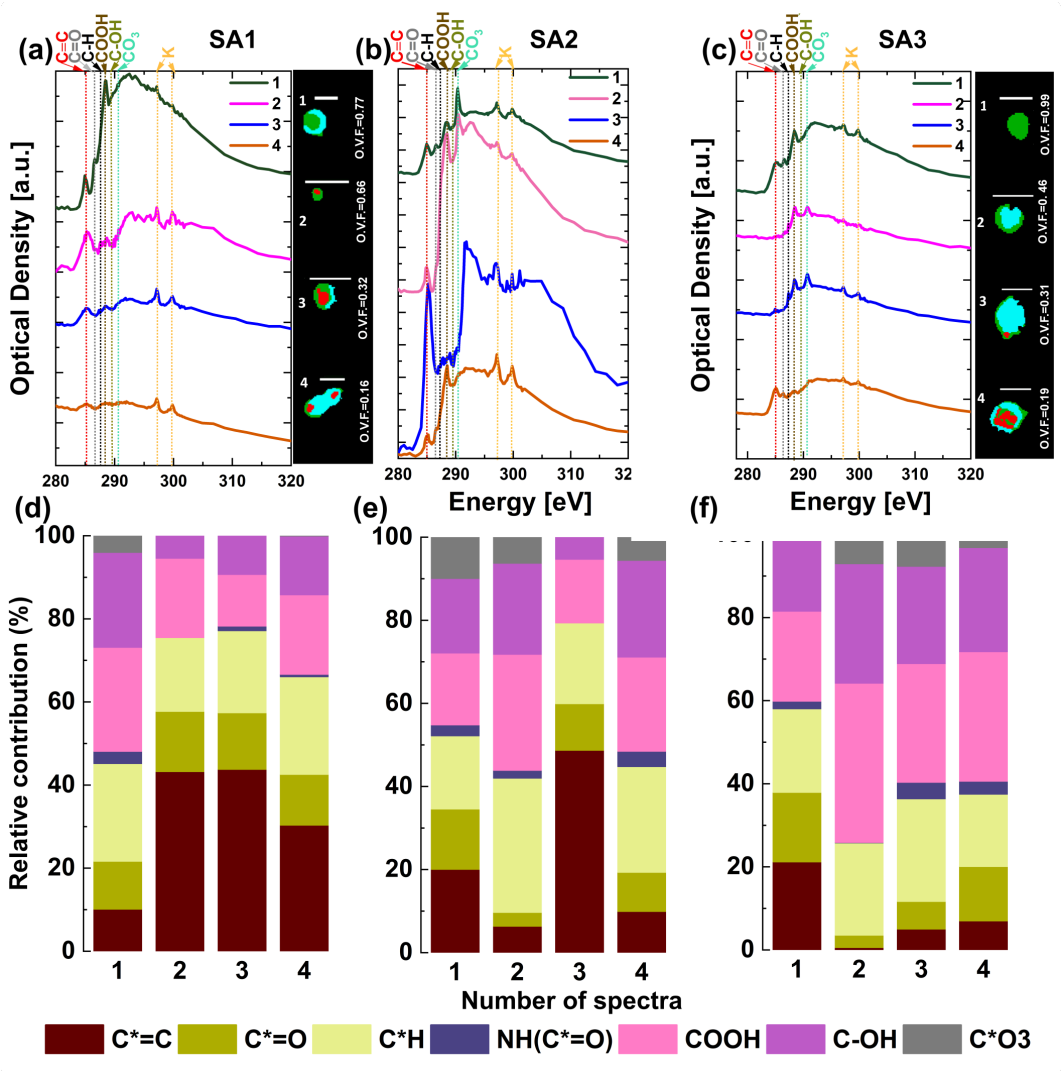

Figure 4.3: (a-c) C-K edge STXM/NEXAFS spectra obtained from four representative types of particles for each sample. The carbon map to the right of each spectrum shows the STXM/NEXAFS composition illustrating the internal particle heterogeneity. The areas dominated by organic carbon constituents are green, soot constituents are red, and inorganic regions are cyan. Each of the scale bars represents 1μm. (d-f) Relative contribution obtained from each of the C-functionalities observed for the respective spectra.

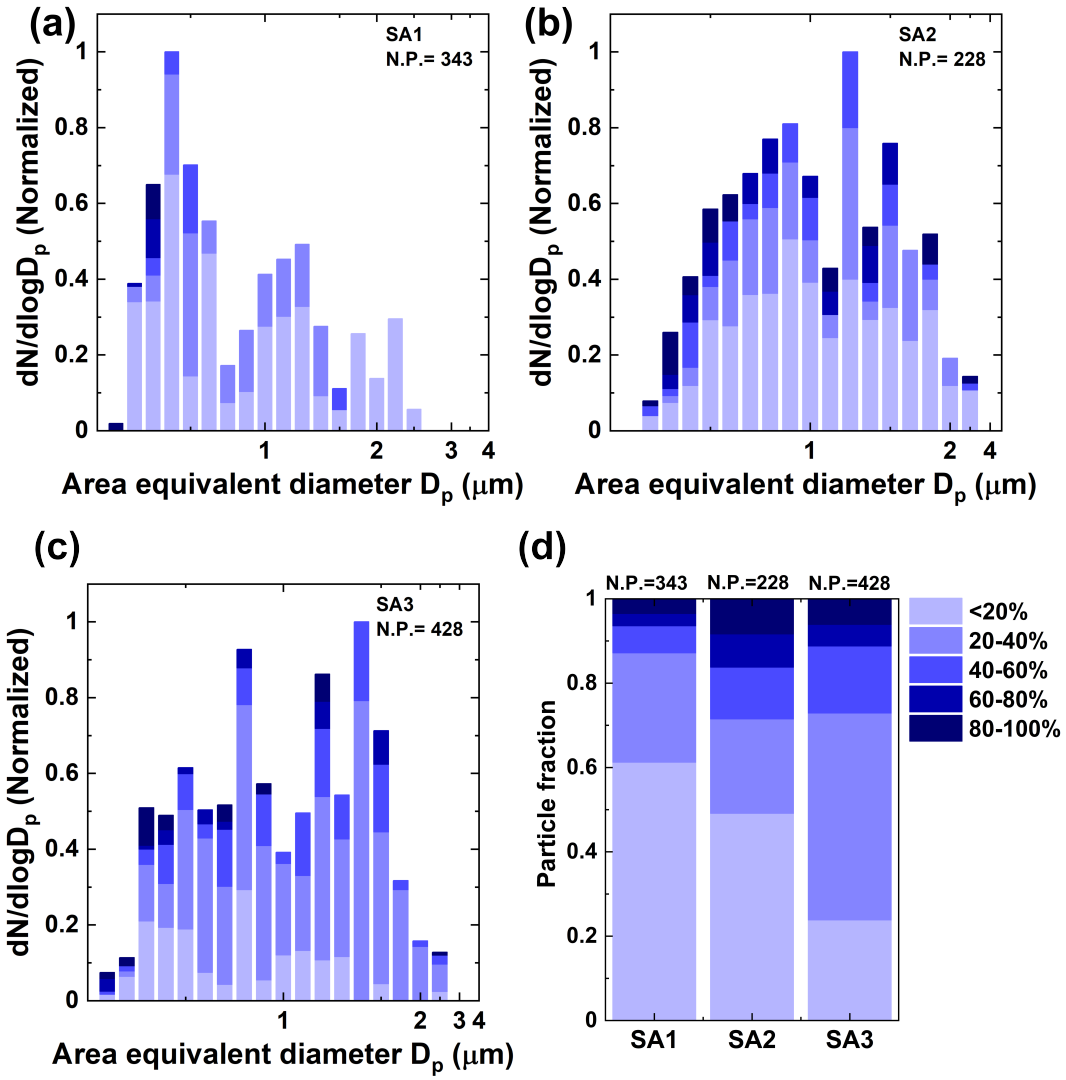

Figure 4.4: Histograms (a-c) show the distribution of organic volume fraction observed in samples SA1, SA2 and, SA3. The darker shade represents the particles with a higher organic volume fraction and the lighter shade shows the particle with a lower organic volume fraction. Figure (d) shows the normalized contribution of the organic volume fraction obtained for each sample. Here, the numbers indicate the identity of particle's spectra, C-map, and relative contribution in each sample.

Figure 4.4 shows the size-resolved OVF of the particles containing each of the samples.

The size-resolved OVF plots (Figure 4.4(a-c)) indicate that the smaller size particles (< 1 μm) are organic rich. Estimated OVF demonstrated that a significant fraction of particles ($> 40\%$) was associated with organics (20-100%). Particles with OVF $< 20\%$ dominated SA1 indicating a larger amount of inorganic (INO) species, likely due to the presence of thin organic coating, with respect to SA2 and SA3 that were dominated by organic-rich particles. The detail of OVF calculation is reported in the Supporting Information B.2. The population mixing state analysis further supports this trend (Figure 4.2(e)). Representative OVF maps are shown in Figure B.23.

The distribution of organic matter affects the phase state of atmospheric aerosol [189, 221]. We evaluated the particle phase state from tilted SEM images (75°) and STXM/NEXAFS [222, 223]. Figure 4.5(a-c) shows the direct observation of phase state from tilted SEM images where the phase state was obtained from particles' aspect ratio (particle width/height). The viscosity boundary shown is defined from a previous study [224]. High viscosity particles (solid/semi-solid-like) maintain a low aspect ratio (1-1.85) [224] upon impaction on the substrate (Figure 4.5(a)). Low viscosity particles (liquid-like) become more oblate upon impaction, exhibiting higher aspect ratios (>1.85) [224] (Figure 4.5(b-c)). Particles in SA1 have a lower aspect ratio (more viscous). From the STXM/NEXAFS, the height of the particles was inferred from the total carbon absorption (TCA) [225] (Figure 4.5(d-f)). The TCA measures the distance that the X-ray photons travel through the particle and provides an estimation of particle thickness. A higher TCA value indicates a solid-like phase,

whereas a lower TCA indicates a liquid-like phase. As shown in Figure 4.5(d-f), solid, semi-solid, and liquid regions were defined from previously reported measurements of lab-generated and field organic particles [212, 223, 226]. A larger fraction of OC+INO particles from SA1 ($\sim$ 18%) had higher TCA values (more solid) compared to SA2 ($\sim$ 7%) and SA3 ($\sim$ 9%) (Table B.5). Most of the particles from SA3 lie in the liquid region, and more significant fractions of OC+EC+INO from SA2 fall in the solid region.

For a comprehensive understanding of the collected ambient particles' phase state, we extracted the ambient conditions from the GFS analysis along the FLEXPART modeled path weighted by the residence time for each sampling time. Figure B.24 shows the ambient conditions of SA1, SA2, and SA3 for the last five days of transport. Using the ambient relative humidity (RH) and temperature (T_{amb}) and the dry glass transition temperature ($T_{g,dry}$) from a previous OMP study for CHO molecular formulas [227], we estimated the RH-dependent T_g (equation B.2.6 (Figure 4.5(g-i)). The phase state can be predicted from T_g and ambient temperature. For example, if $T_g > T_{amb}$, a solid-state is expected, and if $T_g < T_{amb}$, semi-solid to liquid states are predicted[228]. We used the $T_{g,dry}$ from a previous Pico study [227] because the molecular composition was not available for our samples. The actual molecular composition might be different, which added a significant caveat in estimating the predicted T_g. The overall distribution of T_g exceeds T_{amb} for SA1, whereas for SA2 and SA3, T_g mainly lies below T_{amb}. These findings suggest that most SA1 particles

were more viscous, whereas SA2 and SA3 particles were less viscous at the time of collection, supporting the aspect ratio and the TCA results.

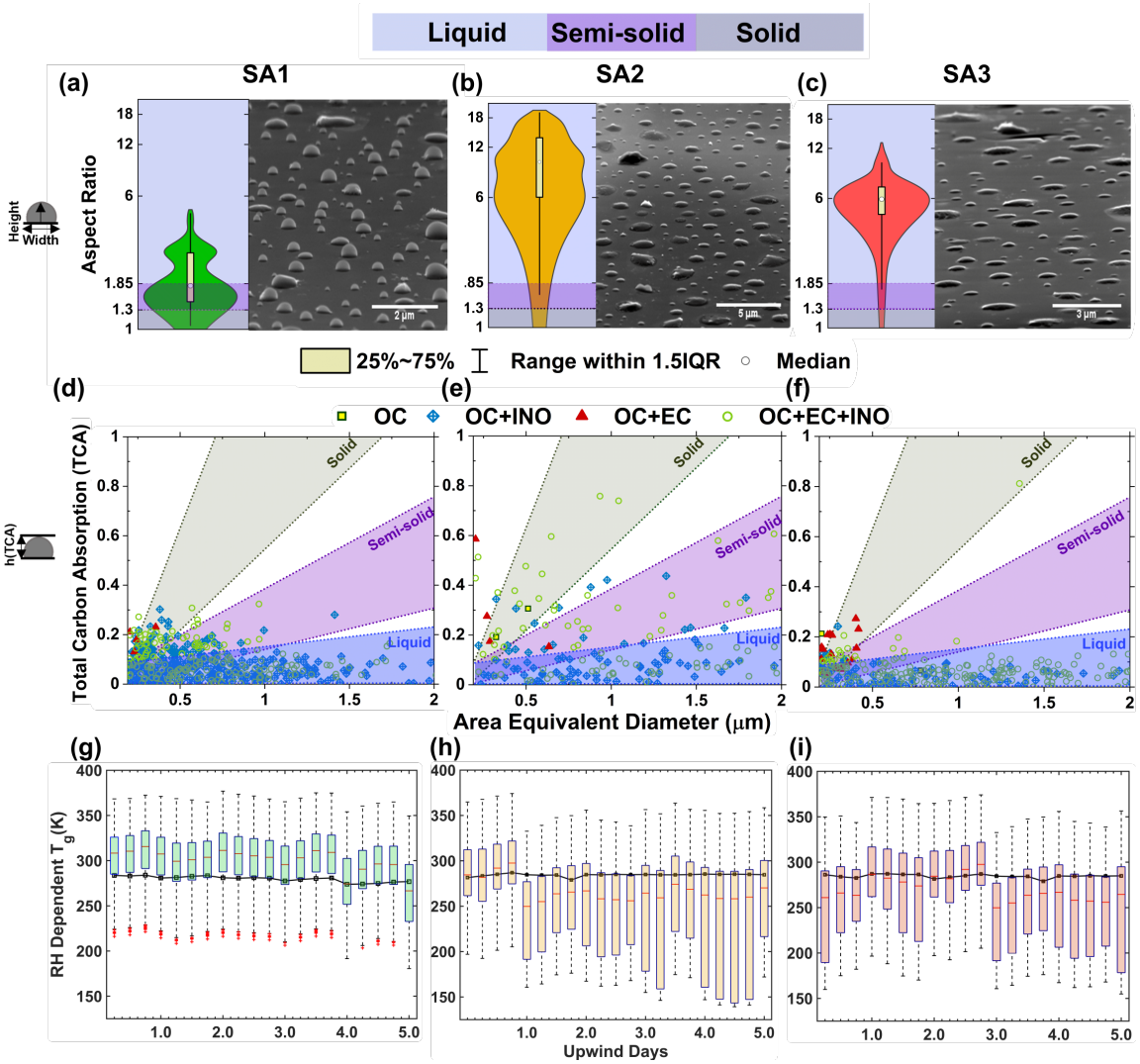

Figure 4.5: Phase state of particles. (a-c) Aspect ratio violin plots for individual particles measured from tilted (75°) SEM images with different viscosity regions [224]. (d-f) The optical thickness of total carbon was obtained from the STXM/NEXAFS [223] with phase state boundaries [212, 223, 226]. (g-i) RH dependent T_g values for the last five days of transport for the maximum, mean, and minimum RH. The black line shows the ambient temperature. The centerline(red) of the box shows the median, and the top and bottom of the box represent the third(Q3) and first quartiles(Q1). The whisker shows $Q3 + 1.5*$ interquartile range (IQR, $Q3$–$Q1$, maximum) and $Q1 - 1.5*$ (IQR, minimum).

4.3.3 Ice Nucleation and INP Identification

Figure 4.6(a) shows direct observations of IN via IN-ESEM of individual internally mixed particles. Figure 4.6(b) illustrates the immersion mode freezing (IMF) and deposition ice nucleation (DIN) conditions at which IN was observed initially for each sample. The temperature and RH with respect to ice (RH_{ice}) at which the first IN was observed for each of the samples are mentioned in Table B.6. We observed IMF at four different temperatures, ranging from 235 to 250K. At the warmest temperature (250K), no significant difference was observed in RH_{ice} among the three samples, and ice nucleated below water saturation (RH_{ice}=122%). However, in this study, we did not investigate the influence of solutes on IN activity of the particles [229].

We investigated DIN at four different temperatures ranging from 205 to 220K. Particles can have microscopic pores, and pore-condensation freezing can be part of the DIN [191]. The particles nucleated ice via DIN at RH_{ice} between 119 and 140%, considerably lower than the water saturation and homogeneous freezing limit [106]. The blue shaded region shows the predicted glass transition temperature obtained using average $T_{g,dry}$ from a previous OMP study [227]. The grey shaded regions show the IN temperatures and RH_{ice} observed from another OMP study [164]. At all temperatures, particles of SA1 show better ice nucleation propensity in deposition mode, requiring lower RH_{ice} to nucleate ice. The uncertainty in the RH_{ice} measurement was derived from the uncertainty of $\Delta T_d < (\pm 0.15$ K) and of $\Delta T_p < (\pm 0.3$ K).

The inter-particle variability in RH_{ice} is smaller than the RH_{ice} error bars from the experimental uncertainties.

We calculated the heterogeneous IN rate coefficients (J_{het}) using the water-activity-based immersion freezing model (ABIFM) [230]. The J_{het} parameterization provides critical information regarding the ice formation mechanism needed for predicting the INP types, cloud modeling and so forth. In ABIFM, the droplet's water activity is considered equal to the ambient RH [230].

Figure 4.6(c) illustrates the experimentally derived J_{het} (Table B.7)along with four parameterizations of previous laboratory particle types, including illite, leonardite, 1-nonadecanol monolayer coatings, and natural Asian, Saharan, Canary Island, and Israel dusts [230, 231, 232] and a previous OMP study [164]. The J_{het} uncertainties arise from a variety of experimental errors or limitations, that is, uncertainties in the number of observed IN events, temperature, RH, and surface area. Compared to previous laboratory-generated and natural dust parameterizations, this study showed shallower slopes because the particles collected at OMP were not a single species; rather, different species were internally mixed. Although OMP samples contain dust INPs, those particles do not have similar slopes as natural dust. This may be because OMP samples comprised various INPs rather than a single particle type and, also, dust particles were atmospherically aged. To predict the IMF of the particles over

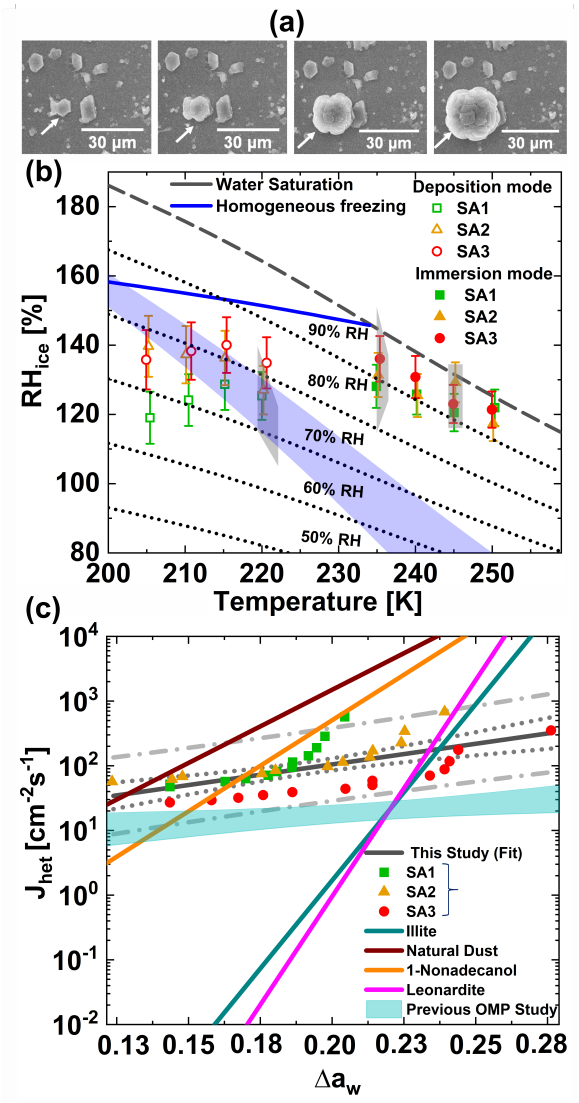

Figure 4.6: a) Dynamic observation of ice nucleation via IN-ESEM of an individual internally mixed particle of SA2 at 210K and 124.5% RH_{ice}. The arrows show the INP before and after nucleating ice and ice crystal growth. (b) The mean onset conditions for ice nucleation. The homogeneous freezing limit for J_{hom}=10^{10} $cm^{-3}s^{-1}$ and $\Delta a_w = 0.31$ is shown with a solid blue line. The error bar on RH_{ice} arises from experimental uncertainties. The gray shaded regions show the RH_{ice} observed from a previous study at Pico[164]. The blue shaded region shows the predicted glass transition temperature. (c) Experimentally derived J_{het} as a function of change of water activity (Δa_w). The solid grey line shows the log-linear fit from J_{het} values, the dotted and dot-dash line indicates the 95% confidence and prediction bands, respectively. The light teal shaded region shows the bounds of J_{het} observed from a previous study at Pico [164]

the Atlantic Ocean, we derived a new J_{het} parameterization of the ABIMF model [230], as shown in Figure 4.5(c) (darker gray line) where $J_{het}=10^{(m\times\Delta a_w+c)}$ with slope m=6.38±1.32 and intercept c=0.74±0.26. This study shows a relatively steeper slope of J_{het} compared to a previous OMP study [164].This difference may arise from the chemical composition of particles and aging. In the previous study, particles were collected during August-September and air masses were comparatively less aged (∼13 days) whereas for this study particles were collected during July and were more aged (∼16 days). We identified 25 individual INPs from two of the three samples (7 from SA2 and 18 from SA3). Though sample SA1 showed better IN activity, unfortunately, we were not able to identify the INPs because the silicon nitride window broke after the IN experiment. Figure 4.7(a) shows the chemical composition of the identified INPs obtained from EDX spectra. From the elemental composition, we classified the INPs following the particle classification scheme mentioned in Figure B.16. We observed four types of INPs: carbonaceous (C), sulfates (S), carbonaceous coated dust (CCD), and sulfate coated dust (SCD). Figure 4.7(b) shows the normalized INP fraction for each class. The INPs of SA2 were dominated by coated dust (56%) whereas the INPs of SA3 were dominated by sulfates (50%) and coated dust (43%). In the case of SA3, the particle population showed 35% carbonaceous, 10% sulfate, 8% coated dust, whereas the INP population indicated 5% carbonaceous, 50% sulfate and 43% coated dust. From Figure 4.7(a) we can conclude that all the identified INPs are internally mixed with either carbonaceous or sulfate coatings. Figure B.25 shows

representative identified INPs with respective EDX spectra. A previous OMP study observed coated dust, aged sea salt, sulfate and carbonaceous INPs [164]. However, more INPs should be identified in future studies to understand the composition of INPs for different temperatures and freezing modes.

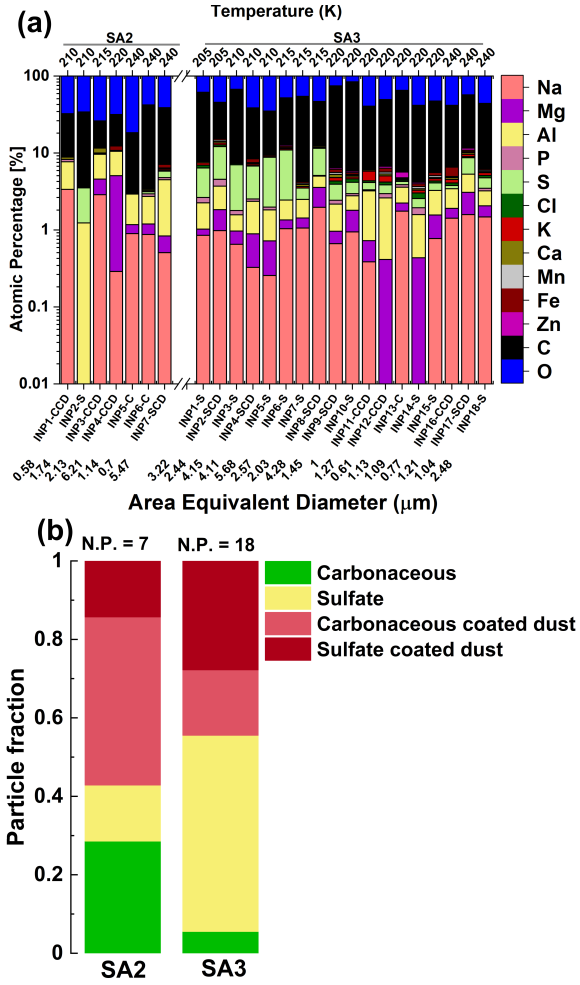

Figure 4.7: (a) Elemental composition of 7 identified individual INPs from SA2, and 18 from SA3. Four classes of INPs were observed, which were shown on the bottom axis, named as C (Carbonaceous), S (Sulfate), CCD (Carbonaceous coated dust) and, SCD (Sulfate coated dust). The top X-axis shows the temperature at which the ice nucleated. The bottom X-axis shows the measured area equivalent diameter of each of the identified INPs; (b) Classified normalized INP fraction from SA2 and SA3 samples.

The physicochemical properties of particles substantially affect DIN efficiencies [181, 199]. The relatively higher IN ability of the SA1 particles can be attributed to their size-resolved chemical composition, morphology, phase state, and mixing state. For example, we observed broader size distribution (Figure 4.2a), dominance of uncoated and coated dusts at particle size greater than 2.1 μm., and dominance of viscous particles (Figure 4.5a) and more internally mixed particles (Figure 4.2e) in sample SA1. A significant fraction of particles belong to the OC+INO class for sample SA1. Therefore, the inclusion of INO material may play a role in impacting the glass transition temperature. We observed higher TCA for the majority of OC+INO particles in SA1 than in SA2 or SA3. The majority of OC+INO particles lie between the high viscosity boundaries. Enhanced ice nucleation ability of mineral dust has often been associated with a small portion of organic matter rather than the mineral components [233]. The STXM/NEXAFS shows that SA1 particles with higher OC+INO fraction are more solid-like (tilted view of SEM images) and have a thin organic coating (from OVF measurement) compared to other samples. The solid organic coating might enhance the DIN activity by providing a solid surface for IN and impact multiphase reactions. The observed differences in DIN efficiencies of different samples indicate that the physicochemical properties of the aerosols can be essential factors in controlling DIN in the free troposphere.

During long-range transport, particles may experience several cloud cycling [234] that can transform the particles to a porous structure [182, 235], eventually promoting

ice formation. The mixing state of the aerosols also transformed during long-range transport. From the identified INPs, we observed different coated dust, carbonaceous, and sulfate particles which suggests the evolution of the mixing state of the INPs in the free troposphere. INP parameterizations are derived for different particle types, suggesting the importance of the mixing state of the overall particle population to predict the ice nucleation [236]. However, a limited number (25 particles) of INPs were identified in this study, which warrants further investigation to generate statistically significant INP characteristics.

4.4 CONCLUSIONS

The aerosol's cold cloud formation potential is driven by multiple factors, including aerosol size distribution, aerosol composition, mixing state, phase state, and morphology. A recent aerosol–ice formation closure study highlighted that size-resolved chemical composition of individual particles is crucial to achieving closure between measured and predicted INP number concentrations [237]. Though the previous OMP study also measured the IN propensity and characterized the INP population, it did not provide any detailed characterization of the ambient aerosol population to predict the IN activity [164]. Understanding the role of phase state of aerosol on ice formation also makes this study unique from the previous study [164]. This study employed a multimodal analytical methodology that allows for comprehensive micro-spectroscopic analysis of a large number ($\sim$23,700) of single particles to access size-resolved chemical composition, mixing state, the distribution of organic matter,

functional groups, and phase state. The results showed variability in the aforementioned physicochemical properties for different sampling days. Variation in transport patterns of airmass from the FLEXPART model on different days suggest variable sources, demonstrating the variation of physicochemical properties observed from the micro-spectroscopic analysis.

Direct observation of ice formation using the IN-ESEM also showed variations in IN potential at the deposition mode for different samples, which can manifest from the ambient aerosols' physicochemical properties. A previous study showed that the distribution of organic matter affects the phase state of aerosol, which is central to understand aerosol processes and predicting their IN activity under the deposition mode [189]. Our study highlighted that long-range transported particles exhibited different distributions of organic matter within individual particles, which can substantially influence their IN activity in the deposition mode [182]. Glassy aerosols affect the IN properties of tropical cirrus clouds [201, 238] and extratropical cirrus formation [239] where the freezing mechanism of complex organic mixtures can be affected by the relative time scales of viscosity transitions and ice formation [197]. The presence of sulfate can lower the viscosity of aqueous secondary organic aerosol via plasticizing effect, which enhances the IN efficiency [240]. The identified INPs from two samples indicate a significant fraction of sulfate and sulfate-coated aerosols to serve as INPs. The previous study shows that ammonium sulfate can serve as

INP in the cirrus regime [241]. However, a significant number of INPs characterization is needed to make a firm conclusion. We observed aerosol sample with broader size distribution and containing high viscosity particles nucleate ice more efficiently than other samples. The size resolved chemical composition of that particular sample showed a dominance of coated and uncoated dust at larger size bins (>2.1 μm). The organic coating material on dust may affect the viscosity of that particle. The STXM/NEXAFS reveals that the majority of OC+INO particles fall over the high viscosity boundary. These highly viscous particles will facilitate the formation of ice at cirrus cloud relevant temperature via the deposition mode.

An integrated study of the comprehensive size-resolved chemical composition, direct observation of phase state of individual particles and estimated phase state using molecular corridor approach along with FLEXPART and GFS meteorological analysis allows us to probe the phase state of the particles and their effect on ice formation of long-range transported particles. Our IN experiments complemented the microspectroscopic analysis; in fact, the RH-dependent T_g showed that solid-like particles are efficient INPs nucleating ice, which is vital to predicting the ice nucleation in the atmosphere. Overall, this study advances the understanding of the role of the phase state of long-range transported aerosols in ice cloud formation.

ACKNOWLEDGMENTS

The Pacific Northwest National Laboratory (PNNL) group acknowledges support

from the Laboratory Directed Research and Development program at PNNL. The CCSEM/EDX and IN analysis were performed at the Environmental Molecular Sciences Laboratory, a national scientific user facility at PNNL. PNNL is operated by the U.S. Department of Energy by Battelle Memorial Institute under contract DE-AC06-76RL0. STXM/NEXAFS analysis at beamline 5.3.2.2 of the Advanced Light Source at the Lawrence Berkeley National Laboratory is supported by the Director, Office of Science, Office of Basic Energy Sciences of the U.S. Department of Energy under contract no. DE-AC02-05CH11231. We acknowledge funding from the U.S. Department of Energy, Office of Science (BER), Atmospheric System Research (DE-SC0006941, DESC0008613, and DE-SC0016370), the National Science Foundation (AGS-1110059 and AGS-1028998), the NASA's Earth and Space Science Graduate Fellowships (NNX12AN97H and NNX13AN68H), and the Earth Planetary and Space Sciences Institute at the Michigan Technological University.

Chapter 5

Tethered Balloon reveals Vertical Profile of aerosol over Arctic

5.1 Introduction

Climate change has the most significant impact on the Arctic region of the Earth [242], where near-surface warming has been nearly twice as large as the global average [243, 244, 245] a phenomenon known as Arctic amplification [246]. Warming causes substantial sea ice loss, with thick multilayer sea ice being replaced by thinner first-year ice, affecting fracture development and open regions of ocean covered by ice [247]. A decrease in sea ice extent and total summer sea ice melting is anticipated by 2050 [248], with adverse impact on Arctic ecosystems and inhabitants [249] and global weather and climate patterns [248].

Arctic aerosol contributes to climate-environment feedbacks by scattering and absorbing solar energy and changing cloud characteristics [163, 250]. As a result of the lack of understanding of many of these impacts, their quantitative assessment remains restricted [8]. The Arctic has a yearly aerosol cycle that is very distinct from other parts of the world [251]. The aerosol particles found in the Arctic are formed by both human activities and natural processes. However, the limited human activities in the Arctic restrict the local anthropogenic sources [252]. Higher aerosol mass loading is observed during winter and spring, with long-range transported pollutants from mid-latitudes and low latitudes contributing to the Arctic Haze [252, 253, 254]. In contrast, summer is characterized by lower aerosol mass loading from local biogenic sources and intermittent transport from low-latitude wildfires, potentially affecting seasonal variability [46, 255]. The primary sink for accumulation-mode particles is wet removal by snow or rain, while the primary sources of these particles are condensation, cloud processing, and transportation [256].

The concentration, size, and composition of aerosols have been demonstrated to influence the overall radiative impact of Arctic clouds [257, 258]. The potential of aerosols to serve as CCN depends on the particle's size and chemical composition under favorable meteorological circumstances [216, 259, 260, 261]. Therefore, to understand aerosol-cloud interactions, simultaneous observations of aerosols and cloud residual compositions are fundamental.

Numerous ground-based observations demonstrate the significance of Arctic aerosol in seasonal variation [45, 46]. However, ground-based observations are often insufficient to explain processes such as cloud processing, photochemical oxidation, and chemical aging. Additionally, several studies have shown that the Arctic atmosphere is stratified [246, 262], resulting in aerosol layering that ground-based measurements cannot detect. Aircraft-based measurement also revealed the variation of chemical composition and sources over the Alaskan Arctic [263]. Although data from large-scale field campaigns collected by aircraft can be informative, the time span of these observations is limited [264, 265]. While aerosol distributions and chemical composition significantly affect the radiative forcing of the ambient aerosol, these variables are poorly represented in climate models [264, 266]. Understanding the relative locations of aerosol and cloud layers and the resultant radiative effects has been assisted by remote sensing techniques [267]. However, there is no presently accurate vertical profile of aerosols that can be obtained using satellites [267]. Large-scale field experiments offer valuable data, but only for a limited time [264]. Based on the above, the study of aerosol particles' composition, characteristics, vertical distribution, and origins in the lower troposphere's contributes significantly to our knowledge of the main processes operating in the Arctic climate system.

To access the vertical profile of Arctic aerosols, a Tethered Balloon System (TBS) was deployed at Oliktok Point, Alaska, in August 2019. Here we illustrated the observations obtained from both offline chemical characterizations and online measurements

along with the meteorological conditions to probe aerosol-cloud interactions.

5.2 Methods

5.2.1 Study location and dates

Tethered balloon system (TBS) flights were deployed at the Department of Energy Atmospheric Radiation Measurement (DOE ARM) Program's third Mobile Facility (AMF3) in Oliktok Point, Alaska (70.51°N, 149.86°W, 2m above mean sea level (a.m.s.l.)) to collect the atmospheric particles. The aerosol particles were collected on multiple substrates (TEM B-film grids, lacey grids, and silicon nitride substrates) using a four-stage cascade impactor (Sioutas Personal Cascade Impactor, SKC, Inc). One programmable low-pressure drop pump was used at a flow rate of 9 l/min. Particle cut-off sizes for four stages are: stage A - 2.5 μm, stage B - 1 μm, stage C - 0.50 μm, and stage D - 0.25 μm. During most of the flights, we deployed three TBS impactor (TBI) packages, two Printed Optical Particle Spectrometers (POPS), and one condensation particle counter (CPC, model 3007, TSI). One of two TBI is usually attached with the tether 500m away from the POPS. One POPS is operated just below the balloon to reach the maximum possible altitude, while the second POPS is generally operated lower on the tether, for example, near the cloud base. The POPS measures particle diameter from 135 nm to 3 μm. The CPC is usually attached one foot away from the POPS right below the balloon. The cut-off size of CPC is around 10 nm. Overall, this TBS aerosol payload provides the aerosol number concentration,

the size distribution above 135 nm, and the size-resolved chemical composition of particles. The dates, times and, flight hours for all TBS flights used are provided in Table B.8. We named the events on August 15th as case study 1 where aerosols were collected through the loitered flight where the TBS reached at certain altitude of interest and started aerosol sampling for a certain time. The events on August 20th as case study 2 where the aerosol sampling was done during the full profile of the TBS flight. Here we select the aerosol samples from stage D for all the sampling days and times based on the particle loading, grid condition and, back trajectory analysis.

5.2.2 Micro-spectroscopic and chemical imaging of particles

We characterized the vertically resolved atmospheric particles using multimodal micro spectroscopic techniques. We utilized a computer-controlled scanning electron microscope (CCSEM, FEI Quanta environmental SEM) with energy-dispersive X-ray spectroscopy (CCSEM-EDX) available in Environmental Molecular Sciences Laboratory at Pacific Northwest National Laboratory. The CCSEM/EDX provides particle size, morphology and, the elemental composition of thousands of individual particles. A total of $\sim$ 19600 particles were analyzed across all samples for this study. CCSEM/EDX experiments were performed at an acceleration voltage of 20 kV and a beam current of 480 pA. Particles were then classified into ten different classes such as “Na-rich”, “Na-rich/sulfate”, “sulfate”, “carbonaceous”, “dust”, “carbonaceous coated dust”, “sulfate coated dust”, “Si+S”, “K+S” and “other” based on the

atomic percentage data using the particle classification scheme shown in the SIB.3 Figure B.26. Chemical imaging of individual particles was performed using scanning transmission electron microscopy (STEM) with an EDX detector.

We characterized the carbon properties of the particles using scanning transmission X-ray microscopy coupled with near-edge x-ray absorption and fine structure (STXM/NEXAFS) (beamline 5.3.2.2) located in the Advanced Light Source (ALS) at Lawrence Berkley National Laboratory collected at one hundred eleven energies of the carbon K-edge. STXM/NEXAFS provides information about different types of internally mixed particles like organic carbon (OC) where the organic mass is homogeneously distributed throughout the entire particle, elemental carbon mixed with organic carbon (EC+OC) where particles possess soot-like properties (higher C=C, sp^2 hybridized bonds) along with organic functionalities, organic carbon infused with inorganics (IN+OC), and particles containing mixtures of organic carbon, elemental carbon, and inorganic inclusion (OC+EC+IN) [211]. The organic nature of particle-containing (OC+IN), (OC+IN+EC) components can be revealed from organic volume fraction (OVF) maps [3, 212, 213].

5.3 Result and discussion

Figure 5.1(a) and (d) shows the TBS distributed temperature sensing, cloud thickness, CPC and, POPS total concentration at different altitudes for case study 1 and 2. For case study 1, the aerosol sampling was done inside the cloud (at 500m) and above the

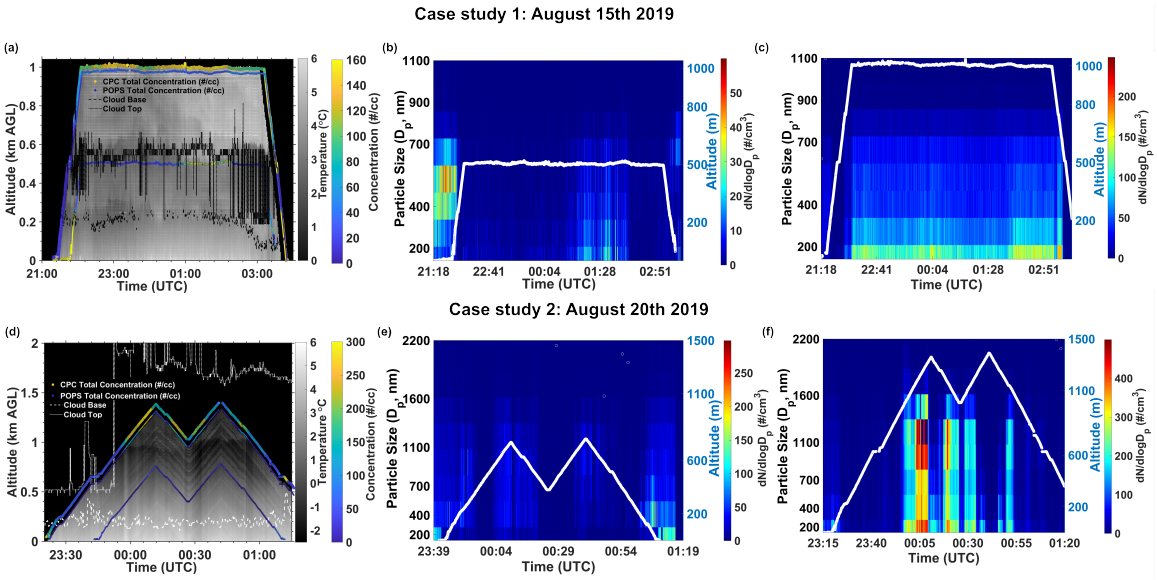

Figure 5.1: Panel (a) and (d) shows the TBS distributed temperature sensing, cloud thickness, CPC and, POPS total concentration at different altitudes for August 15th and August 20th. Panel (b-c) shows the size distribution of aerosols from POPS at 500m and 1000m altitude. Panel (e-f) shows the size distribution of aerosols from POPS at 200m and 1100m altitude.

cloud (at 1000m) and loitered for five hours before reaching ground (Figure 5.1(a)). The number concentration obtained from POPS at both altitudes indicate a low number concentration of particles, where CPC shows a higher number concentration of aerosols above the cloud (at 1000m). A low level temperature inversion is observed in this case which may trap the aerosols in the boundary layer and prevent the aerosols from mixing that in turn form haze [268]. As POPS number concentration at both altitudes does not show significant difference, we probed the size distribution from POPS (Figure 5.1(b-c)). The POPS size distribution shows a variance, and a broader size distribution is observed at high altitude (Figure 5.1(b-c)). For case study 2, the aerosol sampling was done for the full profile of the flight at the cloud base (at 200m)

and inside the cloud (at 1100m) (Figure 5.1(d)). Both CPC and POPS indicates higher number concentration of particles in the case of high altitude (1100m). For this case, temperature inversion is not observed. But the size distribution obtained from POPS shows a clear difference at both altitudes, e.g., broader size distribution of aerosols is observed at high altitude.

To understand the sources of airmass, 120 hr HYSPLIT(Hybrid Single Particle Lagrangian Integrated Trajectory) back trajectories were performed for the start and end of each sampling period. Figure B.27 shows the back trajectory of the airmasses. The Figure B.27 $(a - b)$ indicates a different trajectory of the airmass which suggest variation of aerosol sources, for example, the airmass of case study 1 is coming from the northwest part of Canada, on the other hand the airmass of case study 2 is coming from the northeast part of Siberia. Additionally, the trajectory of airmass on same day at different altitudes are not same (Figure B.27(c-d)). For case study 1, the airmass of high altitude traveled down to 500m on August 13th and transported to high altitude before reaching 1000m where the sampling was done. The airmass of 500m altitude lies almost the same level. Contrarily, the airmass of high altitude of case study 2 was coming from high altitude and merged with the airmass at 200m on August 19th. Then the airmass travelled towards high altitude before reaching 1100m. The airmass of low altitude (200m) was coming from the ground. Overall, these results indicate long range transportation of aerosols before reaching the sampling location.

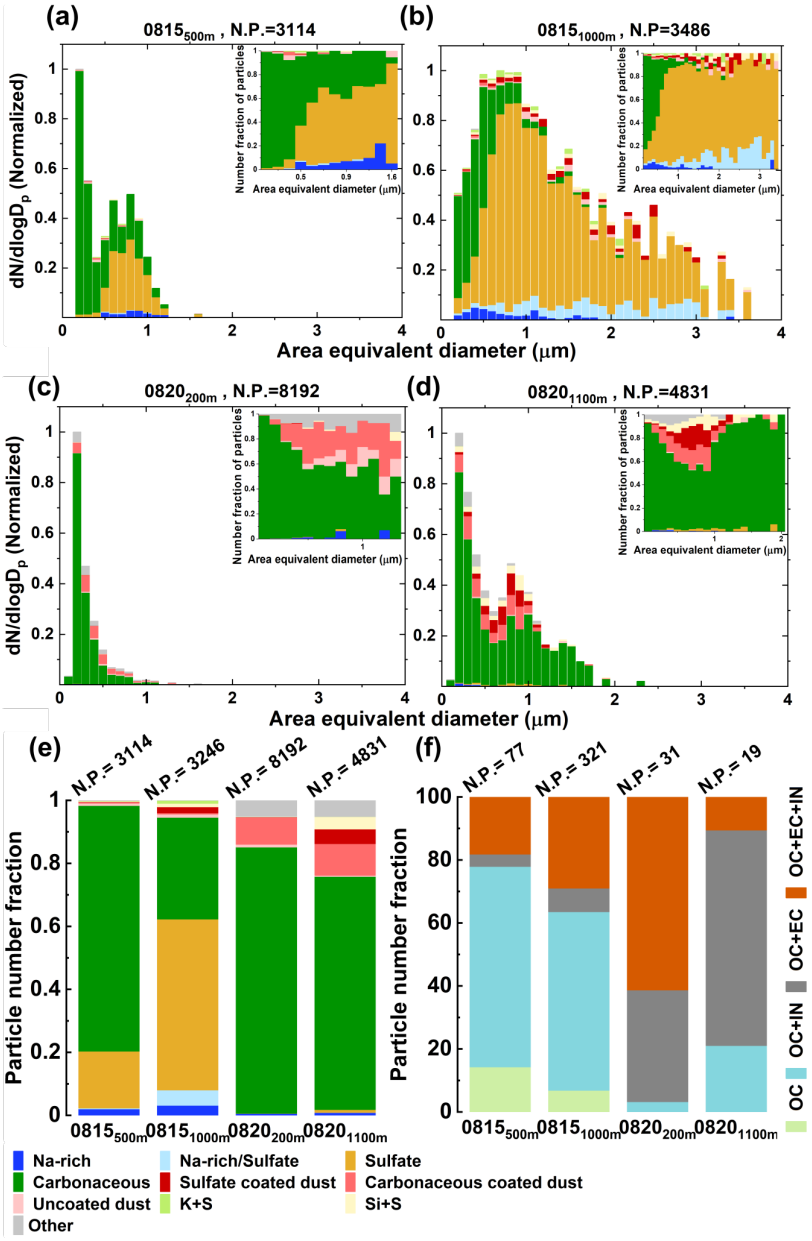

Figure 5.2: The top row- (a) and, (b) shows size-resolved particle classes obtained from CCSEM/EDX at 500m and 1000m altitudes for case study 1. The middle row- (c) and, (d) shows size-resolved particle classes obtained from CCSEM/EDX at 200m and 1100m altitudes for case study 2. The inset shows (a,b,c and, d) the normalized size distribution of the particles, The bottom row- (e) shows the number fraction of CCSEM/EDX derived particle classes, panel (f) shows the particle classes obtained from STXM/NEXAFS analysis where the particles are classified by different combinations of organic carbon (O.C.) and other internally mixed components such as inorganics (IN) and elemental carbon (E.C.). Here N.P. stands for the number of particles analyzed.

Figure 5.2 shows the offline chemical characterizations of the aerosols for the two case studies. Figure 5.2(a) and 5.1(b) shows the size-resolved chemical composition obtained from CCSEM/EDX measurements of the particles collected at 500m and 1000m altitude (case study 1). Dominance of carbonaceous aerosols is observed in the low altitude particle population (500m) in smaller size bins (0.2-0.5 μm), and dominance of sulfate particles is observed in the case of larger size bins (0.5-1.6 μm). In contrast, dominance of carbonaceous aerosols is observed at high altitude particle population (1000m) in smaller size bins (0.2-0.5 μm), and dominance of sulfate particles are observed in the case of larger size bins (0.5-3.6 μm). A broadening of size distribution of aerosols is observed in the case of high-altitude particles which supports the observation from POPS size distribution. The higher sulfate concentration and broadening of the size distribution at high altitude indicates possible cloud processing of the aerosols [216, 269]. Interestingly, the high-altitude aerosols were sampled above the cloud. Now the question arises, how did the cloud processed aerosols reached the higher altitude where there is no cloud? To answer this question, we checked the back trajectory analysis (Figure B.27). The back trajectory analysis shows that the airmass of high-altitude particles (1000m) are coming from very high altitude ($\sim$1450m). During the transport, the airmass reached 500m on August 13th and again move in an upward direction and transported to higher altitude (1100-1450m) during August 14th and 15th and reached 1000m altitude (Figure B.27(c)). We also looked at the cloud base height of the respective dates. We observed that three cloud

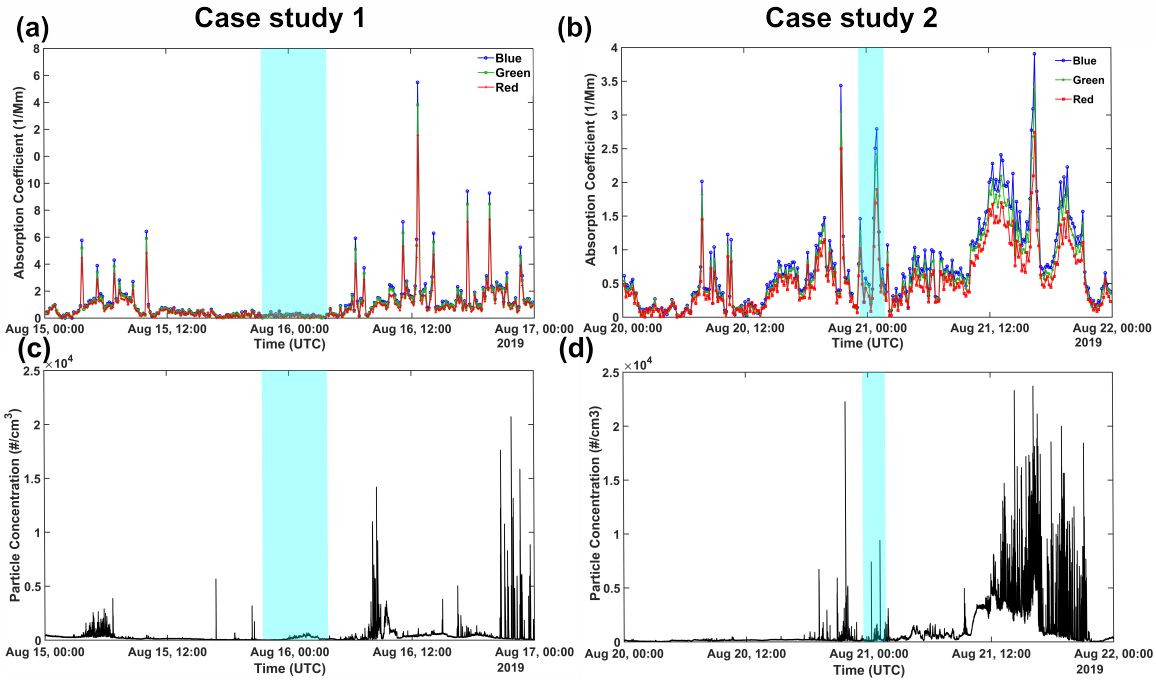

Figure 5.3: Ground based measurements at Oliktok point from PSAP (top row-(a) and (b)) and CPC (bottom row-(c) and (d)). The cyan shaded region showed the sampling duration.

bases present during August 14th and August 15th (Figure B.28). The cloud bases are more prominent during end of August 14th and beginning of August 15th and fluctuates between 300-3000m. Possibly during that time, the aerosols were processed by the clouds and travelled down to 1000m altitude.

A recent study showed core and shell morphology of aerosol is the signature of cloud processing of aerosol [270]. More oxidized organic matter in the cloud contributes to the existence of organic shells after cloud processing. In case study 1, we observed core-shell morphology of aerosols at high altitude (Figure B.29) which is also consistent with the previous observation [270].

Figure 5.2 (c) and (d) shows the size resolved chemical composition obtained from case study 2. The dominance of carbonaceous aerosols is observed at both altitudes and all the size bins, indicating biomass burning aerosols as a possible source. We also observed a broadening of size distribution of aerosols at high altitude (1100m). Interestingly, we did not observe any dominance of sulfate aerosols at high altitude; instead, we observe more coated dust e.g., sulfate-coated dust, carbonaceous coated dust etc. other than carbonaceous aerosols. Now the question arises, why carbonaceous aerosols dominate at both altitude in case study 2? Is it coming from any burning event? Because previous studies indicate that the local oil field affects the air quality at Oliktok Point [258, 271]. We looked at the ground-based measurement from CPC and PSAP (Particle Soot Absorption Photometer) (Figure 5.3). In the PSAP, light transmission through aerosol filter samples is measured at three different wavelengths: red (660 nm), green (522 nm), and blue (470 nm) [272]. Pronounced absorption peaks are observed from PSAP for case study 2 (Figure 5.3(b) shaded region) which is absent in the case of case study 1 (Figure 5.3(a) shaded region). The CPC also shows a similar trend; higher number concentration of particles in case study 2 (Figure 5.3(d) shaded region). The sharp peaks from PSAP and CPC indicate the influence of anthropogenic emission of aerosol which also supports the observations from size resolved chemical composition (Figure 5.2(c) and (d). Figure 5.2(e) indicates normalized particle fraction at each of the altitudes. The low altitude particles (500m) from case study 1 are dominated with carbonaceous aerosols ($\sim$78%), whereas

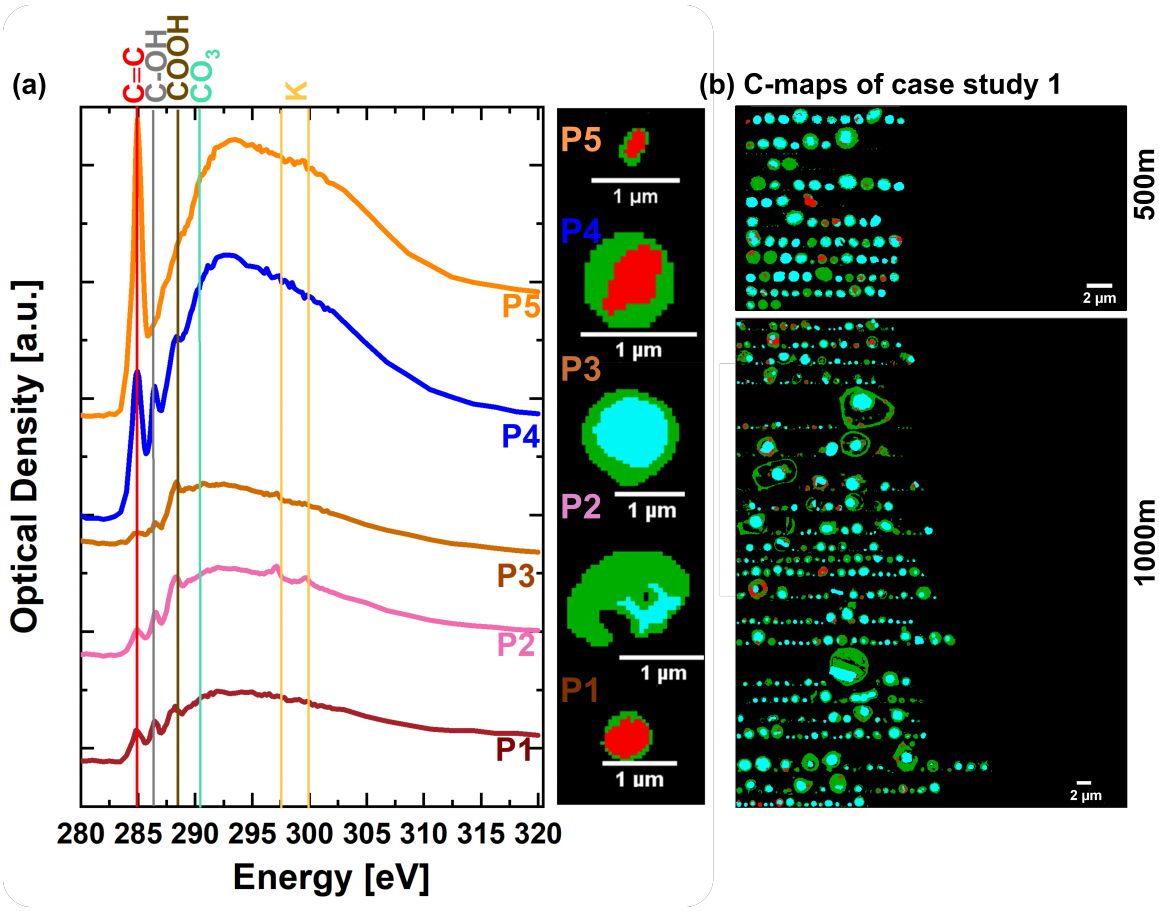

Figure 5.4: Panel (a) shows C-Kedge the STXM/NEXAFS spectra obtained from different types of particles observed in different samples from this study. The right of each spectrum shows the STXM/NEXAFS carbon speciation maps illustrating particle internal heterogeneity based on individual spectra. The areas dominated by organic carbon constituents are green, and inorganic regions are teal and the area dominated by C=C bond is shown with red. Each of the scale bars represents 1µm. Panel (b) shows the carbon speciation maps of all the particles from August 15th 2019 at 500m and 1000m altitudes.

the high altitude(1000m) particles are dominated with sulfate aerosols (∼54%). In contrast, particles from case study 2 are dominated with carbonaceous aerosols at both altitudes.

The carbonaceous features present in the aerosol population were probed

with STXM/NEXAFS. Figure 5.2(f) illustrates the mixing state obtained from STXM/NEXAFS. The particles from case study 1 (August 15th) are dominated with OC+IN class. Contrarily, higher OC+EC+IN and OC+EC is observed in case study 2. The presence of relatively higher OC+EC and OC+EC+IN -containing particles suggests that the airmass for this event is affected by biomass-burning aerosols. The observation from STXM/NEXAFS is also in agreement with the observation from CCSEM/EDX and ground based measurements.

Figure 5.4 (a) shows spatially resolved STXM/NEXAFS spectra of representative internally mixed particles observed in both studies. Carbon speciation maps (C-maps) are shown on the right of each spectrum; green, red, and cyan indicate organic-rich, elemental carbon-rich, and inorganic-rich areas, respectively. Figure 5.3 (b) shows the C-maps of all the particles from case study 1 at both altitudes. The C-maps showing the dominance of OC+IN particles in case study 1. At 1000m, the organic shell (green) and inorganic core (cyan) is more clearly visible, supporting the observation from CCSEM/EDX, SEM imaging, cloud base height measurements, and back trajectory analysis that suggest the possible cloud processing of aerosols.

5.4 Conclusion

Understanding atmospheric particle transport over short and long distances and the vertical profile of particle composition might be a significant benefit of this research. In the field of atmospheric science, studies done by tethered balloon system can

provide efficient, cost-effective, and long-term monitoring of aerosols to access the vertical profile. The combined use of multimodal micro-spectroscopic analysis, online measurement data, and HYSPLIT back trajectory show variations in the physico-chemical properties at different altitudes. These results further support the vertical stratification of the Arctic atmosphere.

This study enabled us to characterize the aerosols from two unique cases. The size-resolved chemical composition from CCSEM/EDX, C-features obtained from STXM/NEXAFS, and online measurements from POPS and CPC from case study 1 suggest possible cloud processing of aerosols at high altitude. The results include broadening of the aerosol size distribution, observation of higher sulfate concentration and core-shell morphology of the aerosol. Furthermore, the back trajectory analysis and cloud base height observation from the ceilometer also support chemical analysis and online measurements. However, there was no cloud during the sampling time at the high altitude. In contrast, at the low altitude case (500m) where the sampling was done inside the cloud were devoid of those cloud processing signatures. Contrarily, case study 2 indicates a higher carbonaceous concentration at both altitudes with broadening of size distribution at high altitude. The ground-based observation from CPC and PSAP indicate a higher concentration of particles suggesting a possible contribution of anthropogenic emission from the ground that has been transported to high altitude. Though aerosol sampling at both altitudes was done inside the cloud, we did not observe any predominance of sulfate aerosols. This probably resulted from

the nature (chemical composition) of the aerosol and cloud aqueous phase interaction.

The predominance of two types of aerosols from two case studies has a different effect on the Arctic climate. The sulfate aerosols scatter solar radiation, thus have cooling effect on Arctic climate. In contrast, some class of carbonaceous aerosol e.g., black carbon absorbs solar radiation thus warms up the climate.

Chapter 6

Conclusion and Future Direction

6.1 Conclusion

The studies reported in this thesis are primarily concerned with the effect of physicochemical properties on ice cloud formation. Both experiments on a known substrate and with complex atmospheric particles were performed. The four most important questions investigated are as follows:

1. Are there differences in water adsorption depending on surface properties, such as the existence of different surface cations?

2. Do the surface properties, e.g., the presence of different surface cations, affect ice nucleation?

3. How do the physicochemical properties of aerosol affect ice cloud formation over

the marine boundary layer?

4. Are the physicochemical properties of aerosols vertically stratified?

The first question is addressed in chapter 2 where controlled experiments performed on a known substrate e.g., muscovite mica, to probe the effect of surface cations on water adsorption using FTIR spectroscopy. We observed that there are differences in mica water interactions depending on the surface cation. However, the hydrogen bonding network appears to be similar across mica surfaces based on FTIR analysis results. It has been found that while RH affects the specifics of the water structure around ions on surfaces like H^+, K^+, and Ca^+-mica, the overall film thickness does not vary significantly.

The second question is addressed in chapter 3 where controlled experiments on a known substrates are conducted to examine the effect of surface cations on heterogeneous freezing of water. The experiments revealed that multivalent cation exposed mica surfaces are better ice nucleators, in the order of $Al^{3+} > Ca^{2+} \simeq Sr^{2+} > Mg^{2+} > K^+$. Based on these findings, we believe that the exposed cation size impacts nucleation rate. This study also examined the relationship between valency and the fraction of silica surface exposed to water. Based on the results of computer simulations, clusters of hydrogen-bonded water molecules anchored by the ions and a higher fraction of free water are associated with multivalent ions on the surface. A substantial fraction of free water can be found in the ion's hydration shells, leading

to ice-like structures, which are facilitated by regions of mica surface beneath them that are empty of ions.

The third question is addressed in chapter 4 where multimodal micro-spectroscopic techniques are employed to explain the effect of physicochemical properties of free tropospheric aerosols on ice cloud formation. Using an integrated study of the comprehensive size-resolved chemical composition, direct observation of phase state of individual particles, and estimated phase state using molecular corridor approach, as well as FLEXPART and GFS meteorological analysis, the phase state of the particles and its effect on ice formation of long-range transported particles can be accessed. This research demonstrates that solid-like particles are effective INPs, which is vital for predicting ice nucleation in the atmosphere. In general, this research contributes to a better understanding of the phase state of long-range transported aerosols in the development of ice clouds.

The fourth question is addressed in chapter 5 where tethered balloon sampling was done to access the vertical profile of aerosol over the Arctic. Micro-spectroscopic analysis, online measurements, and the HYSPLIT back trajectory show that the physicochemical properties vary with altitude These findings provide additional evidence for the Arctic atmosphere's vertical stratification. One of the case studies indicates cloud processing aerosols. Another case study indicates the influence of anthropogenic emission from ground in the vertical aerosol population.

6.2 Future Direction

In this section, results from some exploratory experiments and future directions are discussed. These are not conclusive but may serve as a guide for future generations.

6.2.1 Heterogeneous Freezing of Dilute Solutions on Different Ion Exposed Micas

From Chapter 3, we observed that presence of different cations on muscovite mica affect the freezing temperature in a different way. Ice-nucleating particles are frequently found in mixtures with soluble materials in the real atmosphere. The effect of this soluble substance on ice nucleation, on the other hand, poorly understood. A recent study investigated the immersion mode ice nucleation of dilute salt solution adding different ice nucleators [229]. The study observed that 0.015M salt solution with different ice nucleators has a different effect on freezing. Ice nucleation activity is enhanced for some ice nucleators; for some, it is suppressed, and others remain unchanged. This study motivated us to probe the effect of dilute solution on freezing behavior of different cation exposed mica surfaces. We observed the freezing events of very dilute salt solutions (eg. 0.015M NaCl, 0.015M $(NH_4)_2SO_4$) on K^+ and Mg^{2+}-mica surface. Comparing this data with water freezing data of water and dilute solution, we observed that dilute solution of $(NH_4)_2SO_4$) enhances freezing of water on K^+-mica and hinders freezing on Mg^{2+}-mica. On the other hand, addition of dilute NaCl has no significant effect on freezing on K^+-mica. To make a conclusion

as to why we are observing this effect, more freezing is data needed.

6.2.2 Elucidate the role of surface chemistry of organic-mineral surfaces in ice cloud formation

From chapter 3, we observed that, simply altering the surface cations (without changing surface roughness), we can probe the effect of surface chemistry e.g. surface cations on mica. Mica is one of the common soil dust components [273]. The ability of better ice nucleation on dust surface is often dictated by the presence of a small portion of organic matter rather than mineral components [233]. Because the presence of a low concentration of organic matter increases the glass transition temperature of the mineral. Additionally, fertile soil is found to associate with organic matter such plant litter, animal or microbial residues, lipids, carbohydrates, peptides, cellulose, lignin, and humic like substances [274, 275] and can act as a potential source of INP [276]. So, it will be interesting to observe ice nucleation on different organic matter coated mica surface to elucidate the role of organic-mineral surface on ice cloud formation which is still now poorly understood.

References

[1] Albrecht, B. A. *Science* **1989**, *245*(4923), 1227–1230.

[2] Ramanathan, V.; Cess, R.; Harrison, E.; Minnis, P.; Barkstrom, B.; Ahmad, E.; Hartmann, D. *Science* **1989**, *243*(4887), 57–63.

[3] Lata, N. N.; Zhang, B.; Schum, S.; Mazzoleni, L.; Brimberry, R.; Marcus, M. A.; Cantrell, W. H.; Fialho, P.; Mazzoleni, C.; China, S. *ACS Earth and Space Chemistry* **2021**.

[4] Hartmann, D. L.; Ockert-Bell, M. E.; Michelsen, M. L. *Journal of Climate* **1992**, *5*(11), 1281–1304.

[5] Seinfeld, J. H.; Pandis, S. N. **2006**.

[6] Rosenfeld, D. *Solar Variability and Planetary Climates* **2006**, pages 149–157.

[7] Ramanathan, V.; Crutzen, P. J.; Kiehl, J.; Rosenfeld, D. *science* **2001**, *294*(5549), 2119–2124.

[8] Solomon, S.; Manning, M.; Marquis, M.; Qin, D.; others. *Climate change 2007-the physical science basis: Working group I contribution to the fourth assessment report of the IPCC*, Vol. 4; Cambridge university press, 2007.

[9] Forster, P.; Ramaswamy, V.; Artaxo, P.; Berntsen, T.; Betts, R.; Fahey, D.; Haywood, J.; Lean, J.; Lowe, D.; Myhre, G.; others. *chap. Changes in Atmospheric Constituents and in Radiative Forcing, Cambridge University Press, Cambridge, UK and New York, NY, USA* **2007**.

[10] Cantrell, W.; Heymsfield, A. *Bulletin of the American Meteorological Society* **2005**, *86*(6), 795–808.

[11] Tomasi, C.; Fuzzi, S.; Kokhanovsky, A. *Atmospheric aerosols: Life cycles and effects on air quality and climate;* John Wiley & Sons, 2017.

[12] Kärcher, B. *Geophysical research letters* **2004**, *31*(12).

[13] Rissler, J.; Vestin, A.; Swietlicki, E.; Fisch, G.; Zhou, J.; Artaxo, P.; Andreae, M. *Atmospheric Chemistry and Physics* **2006**, *6*(2), 471–491.

[14] Hoose, C.; Möhler, O. *Atmos. Chem. Phys* **2012**, *12*(20), 9817–9854.

[15] Rogers, D. C.; DeMott, P. J.; Kreidenweis, S. M.; Chen, Y. *Geophysical research letters* **1998**, *25*(9), 1383–1386.

[16] DeMott, P. J.; Prenni, A. J.; Liu, X.; Kreidenweis, S. M.; Petters, M. D.; Twohy, C. H.; Richardson, M.; Eidhammer, T.; Rogers, D. *Proceedings of the National Academy of Sciences* **2010**, *107*(25), 11217–11222.

[17] Boose, Y.; Sierau, B.; García, M. I.; Rodríguez, S.; Alastuey, A.; Linke, C.; Schnaiter, M.; Kupiszewski, P.; Kanji, Z. A.; Lohmann, U. *Atmospheric Chemistry and Physics* **2016**, *16*(14), 9067–9087.

[18] Pruppacher, H. R.; Klett, J. D. In *Microphysics of clouds and precipitation;* Springer, 2010; pages 10–73.

[19] Cziczo, D. J.; Froyd, K. D.; Hoose, C.; Jensen, E. J.; Diao, M.; Zondlo, M. A.; Smith, J. B.; Twohy, C. H.; Murphy, D. M. *Science* **2013**, *340*(6138), 1320–1324.

[20] Ansmann, A.; Tesche, M.; Althausen, D.; Müller, D.; Seifert, P.; Freudenthaler, V.; Heese, B.; Wiegner, M.; Pisani, G.; Knippertz, P.; others. *Journal of Geophysical Research: Atmospheres* **2008**, *113*(D4).

[21] Marcolli, C. *Atmospheric Chemistry and Physics* **2014**, *14*(4), 2071–2104.

[22] Westbrook, C.; Illingworth, A. *Quarterly Journal of the Royal Meteorological Society* **2013**, *139*(677), 2209–2221.

[23] Durant, A. J.; Shaw, R. A. *Geophysical Research Letters* **2005**, *32*(20).

[24] Ladino Moreno, L. A.; Stetzer, O.; Lohmann, U. *Atmospheric Chemistry and Physics* **2013**, *13*(19), 9745–9769.

[25] Niehaus, J.; Cantrell, W. *The journal of physical chemistry letters* **2015**, *6*(17), 3490–3495.

[26] Microphysics of clouds and precipitation, 361–446. Pruppacher, H. R.; Klett, J. **1997**.

[27] Zuberi, B.; Bertram, A. K.; Koop, T.; Molina, L. T.; Molina, M. J. *The Journal of Physical Chemistry A* **2001**, *105*(26), 6458–6464.

[28] Murray, B.; O'sullivan, D.; Atkinson, J.; Webb, M. *Chemical Society Reviews* **2012**, *41*(19), 6519–6554.

[29] Murray, B. J.; Wilson, T. W.; Dobbie, S.; Cui, Z.; Al-Jumur, S. M.; Möhler, O.; Schnaiter, M.; Wagner, R.; Benz, S.; Niemand, M.; others. *Nature Geoscience* **2010**, *3*(4), 233–237.

[30] Atkinson, J. D.; Murray, B. J.; Woodhouse, M. T.; Whale, T. F.; Baustian, K. J.; Carslaw, K. S.; Dobbie, S.; O'Sullivan, D.; Malkin, T. L. *Nature* **2013**, *498*(7454), 355.

[31] Knopf, D. A.; Wang, B.; Laskin, A.; Moffet, R. C.; Gilles, M. K. *Geophysical research letters* **2010**, *37*(11).

[32] DeMott, P. J. *Journal of Applied Meteorology and Climatology* **1990**, *29*(10), 1072–1079.

[33] Tang, M.; Cziczo, D. J.; Grassian, V. H. *Chemical reviews* **2016**, *116*(7), 4205–4259.

[34] Cziczo, D. J.; Froyd, K. D.; Gallavardin, S. J.; Moehler, O.; Benz, S.; Saathoff, H.; Murphy, D. M. *Environmental Research Letters* **2009**, *4*(4), 044013.

[35] Eastwood, M. L.; Cremel, S.; Wheeler, M.; Murray, B. J.; Girard, E.; Bertram, A. K. *Geophysical Research Letters* **2009**, *36*(2).

[36] Fitzgerald, E.; Ault, A. P.; Zauscher, M. D.; Mayol-Bracero, O. L.; Prather, K. A. *Atmospheric Environment* **2015**, *115*, 19–25.

[37] Sullivan, R. C.; Miñambres, L.; DeMott, P. J.; Prenni, A. J.; Carrico, C. M.; Levin, E. J. T.; Kreidenweis, S. M. *Geophysical Research Letters* **2010**, *37*(24).

[38] Tobo, Y.; DeMott, P. J.; Raddatz, M.; Niedermeier, D.; Hartmann, S.; Kreidenweis, S. M.; Stratmann, F.; Wex, H. *Geophysical Research Letters* **2012**, *39*(19).

[39] Hegg, D.; Baker, M. *Reports on progress in Physics* **2009**, *72*(5), 056801.

[40] Cziczo, D. J.; Ladino, L.; Boose, Y.; Kanji, Z. A.; Kupiszewski, P.; Lance, S.; Mertes, S.; Wex, H. *Meteorological Monographs* **2017**, *58*, 8–1.

[41] Adapa, S.; Swamy, D. R.; Kancharla, S.; Pradhan, S.; Malani, A. *Langmuir: the ACS journal of surfaces and colloids* **2018**, *34*(48), 14472–14488.

[42] Balmer, T. E.; Christenson, H. K.; Spencer, N. D.; Heuberger, M. *Langmuir* **2008**, *24*(4), 1566–1569.

[43] Lata, N. N.; Zhou, J.; Hamilton, P.; Larsen, M.; Sarupria, S.; Cantrell, W. *The Journal of Physical Chemistry Letters* **2020**, *11*(20), 8682–8689.

[44] Schmale, J.; Zieger, P.; Ekman, A. M. *Nature Climate Change* **2021**, *11*(2), 95–105.

[45] Kirpes, R. M.; Bonanno, D.; May, N. W.; Fraund, M.; Barget, A. J.; Moffet, R. C.; Ault, A. P.; Pratt, K. A. *ACS central science* **2019**, *5*(11), 1760–1767.

[46] Quinn, P.; Shaw, G.; Andrews, E.; Dutton, E.; Ruoho-Airola, T.; Gong, S. *Tellus B: Chemical and Physical Meteorology* **2007**, *59*(1), 99–114.

[47] Langmuir, I. *J. Am. Chem. Soc.* **1918**, *66*, 1361–1403.

[48] de Poel, W.; Pintea, S.; Drnec, J.; Carla, F.; Felici, R.; Mulder, P.; Elemans, J. A.; van Enckevort, W. J.; Rowan, A. E.; Vlieg, E. *Surf. Sci.* **2014**, *619*, 19–24.

[49] Mazurkiewicz, J.; Mearns, F. J.; Losic, D.; Weeks, L.; Waclawik, E. R.; Rogers, C. T.; Shapter, J. G.; Gooding, J. J. *J. Vac. Sci. Technol. B* **2002**, *20*(6), 2265–2270.

[50] Zhang, F.; Zhang, P.; Hou, J.; Yun, X.; Li, W.; Du, Q.; Chen, Y. *ACS Appl. Mater. Interfaces* **2015**, *7*(16), 8699–8705.

[51] Beaglehole, D.; Radlinska, E.; Ninham, B.; Christenson, H. *Phys. Rev. Lett.* **1991**, *66*(16), 2084.

[52] Beaglehole, D.; Christenson, H. *J. Phys. Chem.* **1992**, *96*(8), 3395–3403.

[53] Cantrell, W.; Ewing, G. E. *J. Phys. Chem. B* **2001**, *105*(23), 5434–5439.

[54] Miranda, P. B.; Xu, L.; Shen, Y. R.; Salmeron, M. *Phys. Rev. Lett.* **1998**, *81*, 5876–5879.

[55] Hu, J.; Xiao, X.-d.; Ogletree, D.; Salmeron, M. *Surf. Sci.* **1995**, *344*(3), 221–236.

[56] Arai, T.; Sato, K.; Iida, A.; Tomitori, M. *Sci. Rep.* **2017**, *7*(1), 4054.

[57] Sakuma, H.; Kawamura, K. *Geochim. Cosmochim. Acta* **2009**, *73*(14), 4100–4110.

[58] Fukuma, T.; Ueda, Y.; Yoshioka, S.; Asakawa, H. *Phys. Rev. Lett.* **2010**, *104*(1), 016101.

[59] Odelius, M.; Bernasconi, M.; Parrinello, M. *Physical Review Letters* **1997**, *78*(14), 2855.

[60] Xu, L.; Salmeron, M. *Langmuir* **1998**, *14*(20), 5841–5844.

[61] Cheng, L.; Fenter, P.; Nagy, K.; Schlegel, M.; Sturchio, N. *Physical review letters* **2001**, *87*(15), 156103.

[62] Kirkpatrick, R. J.; Wang, J.; Kalinichev, A. G.; Cygan, R. T. **2004**.

[63] Schlegel, M. L.; Nagy, K. L.; Fenter, P.; Cheng, L.; Sturchio, N. C.; Jacobsen, S. D. *Geochim. Cosmochim. Acta* **2006**, *70*(14), 3549 – 3565.

[64] Balmer, T.; Christenson, H.; Spencer, N.; Heuberger, M. *Langmuir* **2008**, *24*(4), 1566–1569.

[65] Malani, A.; Ayappa, K. *The Journal of Physical Chemistry B* **2009**, *113*(4), 1058–1067.

[66] Wang, J.; Kalinichev, A. G.; Kirkpatrick, R. J. *J. Phys. Chem. C* **2009**, *113*(25), 11077–11085.

[67] Meleshyn, A. *The Journal of Physical Chemistry C* **2009**, *113*(41), 17604–17607.

[68] Xu, K.; Cao, P.; Heath, J. R. *Science* **2010**, *329*(5996), 1188–1191.

[69] Zhao, G.; Tan, Q.; Xiang, L.; Cai, D.; Zeng, H.; Yi, H.; Ni, Z.; Chen, Y. *J. Chem. Phys.* **2015**, *143*(10), 104705.

[70] Debbarma, R.; Malani, A. *Langmuir* **2016**, *32*(4), 1034–1046.

[71] Kobayashi, K.; Liang, Y.; Amano, K.; Murata, S.; Matsuoka, T.; Takahashi, S.; Nishi, N.; Sakka, T. *Langmuir* **2016**, *32*(15), 3608–3616.

[72] Martin-Jimenez, D.; Garcia, R. *J. Phys. Chem. Lett.* **2017**, *8*(23), 5707–5711.

[73] Loganathan, N.; Kalinichev, A. G. *J. Phys. Chem. C* **2017**, *121*(14), 7829–7836.

[74] Quezada, G. R.; Rozas, R. E.; Toledo, P. G. *The Journal of Physical Chemistry C* **2017**, *121*(45), 25271–25282.

[75] Bourg, I. C.; Lee, S. S.; Fenter, P.; Tournassat, C. *J. Phys. Chem. C* **2017**, *121*(17), 9402–9412.

[76] Cafolla, C.; Voïtchovsky, K. *Nanoscale* **2018**, *10*, 11831–11840.

[77] Hu, J.; Xiao, X. D.; Ogletree, D. F.; Salmeron, M. *Science* **1995**, *268*(5208), 267–269.

[78] Xu, L.; Lio, A.; Hu, J.; Ogletree, D. F.; Salmeron, M. *J. Phys. Chem. B* **1998**, *102*(3), 540–548.

[79] Ou, X.; Wang, X.; Lin, Z.; Li, J. *J. Phys. Chem. C* **2017**, *121*(12), 6813–6819.

[80] Bluhm, H.; Inoue, T.; Salmeron, M. *Surf. Sci.* **2000**, *462*(1-3), L599–L602.

[81] de Poel, W.; Vaessen, S. L.; Drnec, J.; Engwerda, A. H.; Townsend, E. R.; Pintea, S.; de Jong, A. E.; Jankowski, M.; Carlà, F.; Felici, R.; Elemans, J. A.; van Enckevort, W. J.; Rowan, A. E.; Vlieg, E. *Surf. Sci.* **2017**, *665*, 56–61.

[82] Prakash, A.; Pfaendtner, J.; Chun, J.; Mundy, C. J. *J. Phys. Chem. C* **2017**, *121*(34), 18496–18504.

[83] Adapa, S.; Malani, A. *Sci. Rep.* **2018**, *8*(1), 12198.

[84] Kobayashi, K.; Liang, Y.; Murata, S.; Matsuoka, T.; Takahashi, S.; Nishi, N.; Sakka, T. *Langmuir* **2017**, *33*(15), 3892–3899.

[85] Loh, S. H.; Jarvis, S. P. *Langmuir* **2010**, *26*(12), 9176–9178.

[86] Park, S.-H.; Sposito, G. *Physical Review Letters* **2002**, *89*(8), 085501.

[87] Park, C.; Fenter, P. A.; Nagy, K. L.; Sturchio, N. C. *Physical review letters* **2006**, *97*(1), 016101.

[88] Pimentel, G. C.; McClellan, A. L. *The hydrogen bond;* Freeman, 1960.

[89] Eisenberg, D.; Kauzmann, W. *The structure and properties of water;* Oxford University Press, 1969.

[90] Du, Q.; Freysz, E.; Shen, Y. R. *Science* **1994**, *264*(5160), 826–828.

[91] Debbarma, R.; Malani, A. *Langmuir* **2016**, *32*(4), 1034–1046.

[92] Kashchieve, D. *Nucleation: Basic theory with applications;* Butterworth Heinemann, 2000.

[93] Li, J.; Lee, T.-C. *Trends Food Sci. Technol.* **1995**, *6*(8), 259–265.

[94] Matus, A. V.; L'Ecuyer, T. S. *J. Geophys. Res.* **2017**, *122*(5), 2559–2578.

[95] Mülmenstädt, J.; Sourdeval, O.; Delanoë, J.; Quaas, J. *Geophys. Res. Lett.* **2015**, *42*(15), 6502–6509.

[96] Hegg, D.; Baker, M. *Rep. Prog. Phys.* **2009**, *72*(5), 056801.

[97] Cziczo, D. J.; Froyd, K. D.; Hoose, C.; Jensen, E. J.; Diao, M.; Zondlo, M. A.; Smith, J. B.; Twohy, C. H.; Murphy, D. M. *Science* **2013**, *340*(6138), 1320–1324.

[98] Cantrell, W.; Heymsfield, A. *Bull. Amer. Meteor. Soc.* **2005**, *86*(6), 795–808.

[99] Murray, B.; O'sullivan, D.; Atkinson, J.; Webb, M. *Chem. Soc. Rev.* **2012**, *41*(19), 6519–6554.

[100] Coluzza, I.; Creamean, J.; Rossi, M. J.; Wex, H.; Alpert, P. A.; Bianco, V.; Boose, Y.; Dellago, C.; Felgitsch, L.; Fröhlich-Nowoisky, J.; Herrmann, H.; Jungblut, S.; Kanji, Z.; Menzl, G.; Moffett, B.; Moritz, C.; Mutzel, A.; Pöschl, U.; Schauperl, M.; Scheel, J.; Stopelli, E.; Stratmann, F.; Grothe, H.; Schmale III, D. G. *Atmosphere* **2017**, *8*(8), 138.

[101] Liu, Z.; He, Z.; Lv, J.; Jin, Y.; Wu, S.; Liu, G.; Zhou, F.; Wang, J. *RSC Adv.* **2017**, *7*, 840–844.

[102] He, Z.; Xie, W. J.; Liu, Z.; Liu, G.; Wang, Z.; Gao, Y. Q.; Wang, J. *Sci. Adv.* **2016**, *2*(6), e1600345.

[103] Zolles, T.; Burkart, J.; Hausler, T.; Pummer, B.; Hitzenberger, R.; Grothe, H. *J. Phys. Chem. A* **2015**, *119*(11), 2692–2700.

[104] Emelyanenko, A. M.; Emelyanenko, K. A.; Boinovich, L. B. *J. Phys. Chem. Lett.* **2020**, *11*(8), 3058–3062.

[105] Pach, E.; Verdaguer, A. *J. Phys. Chem. C* **2019**, *123*(34), 20998–21004.

[106] Koop, T.; Luo, B.; Tsias, A.; Peter, T. *Nature* **2000**, *406*(6796), 611.

[107] Christenson, H. K.; Thomson, N. H. *Surf. Sci. Rep.* **2016**, *71*(2), 367–390.

[108] de Poel, W.; Pintea, S.; Drnec, J.; Carla, F.; Felici, R.; Mulder, P.; Elemans, J. A.; van Enckevort, W. J.; Rowan, A. E.; Vlieg, E. *Surf. Sci.* **2014**, *619*, 19–24.

[109] Schlegel, M. L.; Nagy, K. L.; Fenter, P.; Cheng, L.; Sturchio, N. C.; Jacobsen, S. D. *Geochim. Cosmochim. Acta* **2006**, *70*(14), 3549–3565.

[110] Kumar, A.; Marcolli, C.; Peter, T. *Atmos. Chem. Phys.* **2018**, *2018*, 1–36.

[111] Campbell, J. M.; Meldrum, F. C.; Christenson, H. K. *J. Phys. Chem. C* **2015**, *119*(2), 1164–1169.

[112] Campbell, J. M.; Christenson, H. K. *Phys. Rev. Lett.* **2018**, *120*(16), 165701.

[113] Steinke, I. *Ice nucleation properties of mineral dusts* PhD thesis, **2013**.

[114] Shen, J.; Klier, K.; Zettlemoyer, A. *J. Atmos. Sci.* **1977**, *34*(6), 957–960.

[115] Anim-Danso, E.; Zhang, Y.; Dhinojwala, A. *J. Phys. Chem. C* **2016**, *120*(7), 3741–3748.

[116] Abdelmonem, A. *Atmos. Chem. Phys.* **2017**, *17*(17), 10733–10741.

[117] Teschke, O.; Valente Filho, J. F.; de Souza, E. F. *Chem. Phys. Lett.* **2010**, *485*(1-3), 133–136.

[118] Miranda, P.; Xu, L.; Shen, Y.; Salmeron, M. *Phys. Rev. Lett.* **1998**, *81*(26), 5876.

[119] Li, H.; Zeng, X. C. *J. Chem. Theory Comp.* **2012**, *8*(9), 3034–3043.

[120] Odelius, M.; Bernasconi, M.; Parrinello, M. *Physical Review Letters* **1997**, *78*(14), 2855.

[121] Cantrell, W.; Ewing, G. E. *J. Phys. Chem. B* **2001**, *105*(23), 5434–5439.

[122] Balmer, T.; Christenson, H.; Spencer, N.; Heuberger, M. *Langmuir* **2008**, *24*(4), 1566–1569.

[123] Adapa, S.; Swamy, D. R.; Kancharla, S.; Pradhan, S.; Malani, A. *Langmuir* **2018**, *34*(48), 14472–14488.

[124] Tarasevich, Y. I.; Polyakova, I.; Polyakov, V. *Adsorption Science & Technology* **2002**, *20*(9), 927–935.

[125] Bera, B.; Kumar, N.; Duits, M.; Cohen Stuart, M.; Mugele, F. *Langmuir* **2018**, *34*(45), 13574–13583.

[126] Shannon, R. D. *Acta crystallogr. A* **1976**, *32*(5), 751–767.

[127] Bi, Y.; Cao, B.; Li, T. *Nature Comm.* **2017**, *8*(1), 1–7.

[128] Sear, R. P. *Int. Mater. Rev.* **2012**, *57*(6), 328–356.

[129] Xu, L.; Lio, A.; Hu, J.; Ogletree, D. F.; Salmeron, M. *J. Phys. Chem. B* **1998**, *102*(3), 540–548.

[130] Fitzner, M.; Sosso, G. C.; Cox, S. J.; Michaelides, A. *J. Am. Chem. Soc.* **2015**, *137*(42), 13658–13669.

[131] Fitzner, M.; Sosso, G. C.; Pietrucci, F.; Pipolo, S.; Michaelides, A. *Nature Comm.* **2017**, *8*(1), 1–7.

[132] Lupi, L.; Hudait, A.; Molinero, V. *J. Am. Chem. Soc.* **2014**, *136*(8), 3156–3164.

[133] Reinhardt, A.; Doye, J. P. K. *J. Chem. Phys.* **2014**, *141*(8), 084501.

[134] Hudait, A.; Moberg, D. R.; Qiu, Y.; Odendahl, N.; Paesani, F.; Molinero, V. *Proceedings of the National Academy of Sciences* **2018**, *115*(33), 8266–8271.

[135] Naullage, P. M.; Molinero, V. *J. Am. Chem. Soc.* **2020**, *142*(9), 4356–4366.

[136] Zielke, S. A.; Bertram, A. K.; Patey, G. N. *J. Phys. Chem. B* **2016**, *120*(8), 1726–1734.

[137] Soni, A.; Patey, G. N. *J. Chem. Phys.* **2019**, *150*(21), 214501.

[138] Glatz, B.; Sarupria, S. *J. Chem. Phys.* **2016**, *145*(21), 211924.

[139] Glatz, B.; Sarupria, S. *Langmuir* **2018**, *34*(3), 1190–1198.

[140] Bi, Y.; Cabriolu, R.; Li, T. *J. Phys. Chem. C* **2016**, *120*(3), 1507–1514.

[141] Knopf, D. A.; Alpert, P. A.; Zipori, A.; Reicher, N.; Rudich, Y. *npj Climate and Atmospheric Science* **2020**, *3*(1), 1–9.

[142] Murray, B. J.; Broadley, S. L.; Wilson, T. W.; Atkinson, J. D.; Wills, R. H. *Atmos. Chem. Phys* **2011**, *11*(9), 4191–4207.

[143] Sosso, G. C.; Li, T.; Donadio, D.; Tribello, G. A.; Michaelides, A. *J. Phys. Chem. Lett* **2016**, *7*(13), 2350–2355.

[144] Starr, F. W.; Nielsen, J. K.; Stanley, H. E. *Physical Review E* **2000**, *62*(1), 579.

[145] Steiner, T. *Angew. Chem. Int.* **2002**, *41*(1), 48–76.

[146] Shannon, P.; Markiel, A.; Ozier, O.; Baliga, N. S.; Wang, J. T.; Ramage, D.; Amin, N.; Schwikowski, B.; Ideker, T. *Genome Res.* **2003**, *13*(11), 2498–2504.

[147] Tielrooij, K. J.; Garcia-Araez, N.; Bonn, M.; Bakker, H. J. *Science* **2010**, *328*(5981), 1006–1009.

[148] Yu, H.; Whitfield, T. W.; Harder, E.; Lamoureux, G.; Vorobyov, I.; Anisimov, V. M.; MacKerell, A. D.; Roux, B. *J. Chem. Theory. Comput.* **2010**, *6*(3), 774–786.

[149] Sarupria, S.; Debenedetti, P. G. *J. Phys. Chem. Lett* **2012**, *3*(20), 2942–2947.

[150] Myshakin, E. M.; Jiang, H.; Warzinski, R. P.; Jordan, K. D. *J. Phys. Chem. A* **2009**, *113*(10), 1913–1921.

[151] DeFever, R. S.; Targonski, C.; Hall, S. W.; Smith, M. C.; Sarupria, S. *Chem. Sci.* **2019**, *10*, 7503–7515.

[152] Moroni, D.; Wolde, P.; Bolhuis, P. *Phys. Rev. Lett.* **2005**, *94*(23), 235703.

[153] Beckham, G.; Peters, B. *J. Phys. Chem. Lett.* **2011**, *2*(10), 1133–1138.

[154] Lechner, W.; Dellago, C.; Bolhuis, P. *Phys. Rev. Lett.* **2011**, *106*(8), 085701.

[155] Liang, Y.; Díaz Leines, G.; Drautz, R.; Rogal, J. *J. Chem. Phys.* **2020**, *152*(22), 224504.

[156] Allen, R. J.; Valeriani, C.; Ten Wolde, P. R. *Journal of physics: Condensed matter* **2009**, *21*(46), 463102.

[157] Allen, R. J.; Frenkel, D.; ten Wolde, P. R. *J. Chem. Phys.* **2006**, *124*(2), 024102.

[158] Cabriolu, R.; Li, T. *Physical Review E* **2015**, *91*(5), 052402.

[159] DeFever, R. S.; Sarupria, S. *J. Chem. Phys.* **2017**, *147*(20), 204503.

[160] Bolhuis, P. G. *J. Chem. Phys.* **2008**, *129*(11), 114108.

[161] Cabriolu, R.; Skjelbred Refsnes, K. M.; Bolhuis, P. G.; van Erp, T. S. *J. Chem. Phys.* **2017**, *147*(15), 152722.

[162] Haag, W.; Kärcher, B. *Journal of Geophysical Research: Atmospheres* **2004**, *109*(D12).

[163] Lohmann, U.; Feichter, J. *Atmospheric Chemistry and Physics* **2005**, *5*(3), 715–737.

[164] China, S.; Alpert, P. A.; Zhang, B.; Schum, S.; Dzepina, K.; Wright, K.; Owen, R. C.; Fialho, P.; Mazzoleni, L. R.; Mazzoleni, C.; others. *Journal of Geophysical Research: Atmospheres* **2017**, *122*(5), 3065–3079.

[165] Cozic, J.; Mertes, S.; Verheggen, B.; Cziczo, D. J.; Gallavardin, S.; Walter, S.; Baltensperger, U.; Weingartner, E. *Journal of Geophysical Research: Atmospheres* **2008**, *113*(D15).

[166] Rinaldi, M.; Santachiara, G.; Nicosia, A.; Piazza, M.; Decesari, S.; Gilardoni, S.; Paglione, M.; Cristofanelli, P.; Marinoni, A.; Bonasoni, P.; others. *Atmospheric environment* **2017**, *171*, 173–180.

[167] Cziczo, D. J.; Froyd, K. D.; Hoose, C.; Jensen, E. J.; Diao, M.; Zondlo, M. A.; Smith, J. B.; Twohy, C. H.; Murphy, D. M. *Science* **2013**, *340*(6138), 1320–1324.

[168] Cziczo, D. J.; Froyd, K. D. *Atmospheric research* **2014**, *142*, 15–31.

[169] DeMott, P. J.; Sassen, K.; Poellot, M. R.; Baumgardner, D.; Rogers, D. C.; Brooks, S. D.; Prenni, A. J.; Kreidenweis, S. M. *Geophysical Research Letters* **2003**, *30*(14).

[170] Lloyd, G.; Choularton, T.; Bower, K.; Crosier, J.; Gallagher, M.; Flynn, M.; Dorsey, J.; Liu, D.; Taylor, J. W.; Schlenczek, O.; others. *Atmospheric Chemistry and Physics* **2020**, *20*(6), 3895–3904.

[171] Twohy, C.; Poellot, M. *Atmospheric Chemistry and Physics* **2005**, *5*(8), 2289–2297.

[172] Moffet, R. C.; O'Brien, R. E.; Alpert, P. A.; Kelly, S. T.; Pham, D. Q.; Gilles, M. K.; Knopf, D. A.; Laskin, A. *Atmospheric Chemistry and Physics* **2016**, *16*(22), 14515–14525.

[173] Laskin, A.; Gilles, M. K.; Knopf, D. A.; Wang, B.; China, S. *Annual Review of Analytical Chemistry* **2016**, *9*, 117–143.

[174] Dzepina, K.; Mazzoleni, C.; Fialho, P.; China, S.; Zhang, B.; Owen, R. C.; Helmig, D.; Hueber, J.; Kumar, S.; Perlinger, J. A.; others. *Atmospheric Chemistry and Physics Discussions* **2014**, *14*, 24753–24810.

[175] H. Kroll, J.; D. Smith, J.; L. Che, D.; H. Kessler, S.; R. Worsnop, D.; R. Wilson, K. *Physical Chemistry Chemical Physics* **2009**, *11*(36), 8005–8014.

[176] George, I.; Abbatt, J. *Nature Chemistry* **2010**, *2*(9), 713–722.

[177] A. Knopf, D.; M. Forrester, S.; H. Slade, J. *Physical Chemistry Chemical Physics* **2011**, *13*(47), 21050–21062.

[178] C. Chapleski, R.; Zhang, Y.; Troya, D.; R. Morris, J. *Chemical Society Reviews* **2016**, *45*(13), 3731–3746.

[179] Maring, H.; Savoie, D. L.; Izaguirre, M. A.; Custals, L.; Reid, J. S. *Journal of Geophysical Research: Atmospheres* **2003**, *108*(D19).

[180] Trochkine, D.; Iwasaka, Y.; Matsuki, A.; Yamada, M.; Kim, Y.-S.; Nagatani, T.; Zhang, D.; Shi, G.-Y.; Shen, Z. *Journal of Geophysical Research: Atmospheres* **2003**, *108*(D23).

[181] Wang, B.; Knopf, D. A. *Journal of Geophysical Research: Atmospheres* **2011**, *116*(D3).

[182] Bertozzi, B.; Wagner, R.; Song, J.; Höhler, K.; Pfeifer, J.; Saathoff, H.; Leisner, T.; Möhler, O. *Atmospheric Chemistry and Physics* **2021**, *21*(13), 10779–10798.

[183] Baustian, K. J.; Cziczo, D. J.; Wise, M. E.; Pratt, K. A.; Kulkarni, G.; Hallar, A. G.; Tolbert, M. A. *Journal of Geophysical Research: Atmospheres* **2012**, *117*(D6).

[184] Augustin-Bauditz, S.; Wex, H.; Denjean, C.; Hartmann, S.; Schneider, J.; Schmidt, S.; Ebert, M.; Stratmann, F. **2016**.

[185] Zheng, G.; Wang, Y.; Wood, R.; Jensen, M. P.; Kuang, C.; McCoy, I. L.; Matthews, A.; Mei, F.; Tomlinson, J. M.; Shilling, J. E.; others. *Nature communications* **2021**, *12*(1), 1–10.

[186] Kanakidou, M.; Seinfeld, J.; Pandis, S.; Barnes, I.; Dentener, F. J.; Facchini, M. C.; Dingenen, R. V.; Ervens, B.; Nenes, A.; Nielsen, C.; others. *Atmospheric Chemistry and Physics* **2005**, *5*(4), 1053–1123.

[187] Hallquist, M.; Wenger, J. C.; Baltensperger, U.; Rudich, Y.; Simpson, D.; Claeys, M.; Dommen, J.; Donahue, N.; George, C.; Goldstein, A.; others. *Atmospheric chemistry and physics* **2009**, *9*(14), 5155–5236.

[188] Zhang, Q.; Jimenez, J. L.; Canagaratna, M.; Allan, J. D.; Coe, H.; Ulbrich, I.; Alfarra, M.; Takami, A.; Middlebrook, A.; Sun, Y.; others. *Geophysical research letters* **2007**, *34*(13).

[189] Knopf, D. A.; Alpert, P. A.; Wang, B. *ACS Earth and Space Chemistry* **2018**, *2*(3), 168–202.

[190] Möhler, O.; Benz, S.; Saathoff, H.; Schnaiter, M.; Wagner, R.; Schneider, J.; Walter, S.; Ebert, V.; Wagner, S. *Environmental Research Letters* **2008**, *3*(2), 025007.

[191] Marcolli, C.; Mahrt, F.; Kärcher, B. *Atmospheric Chemistry and Physics* **2021**, *21*(10), 7791–7843.

[192] Kanji, Z. A.; Florea, O.; Abbatt, J. P. *Environmental Research Letters* **2008**, *3*(2), 025004.

[193] Salam, A.; Lesins, G.; Lohmann, U. *Air quality, atmosphere & health* **2008**, *1*(3), 135–142.

[194] Wang, B.; Lambe, A. T.; Massoli, P.; Onasch, T. B.; Davidovits, P.; Worsnop, D. R.; Knopf, D. A. *Journal of Geophysical Research: Atmospheres* **2012**, *117*(D16).

[195] Baustian, K.; Wise, M.; Jensen, E.; Schill, G.; Freedman, M.; Tolbert, M. *Atmospheric Chemistry and Physics* **2013**, *13*(11), 5615–5628.

[196] Knopf, D. A.; Alpert, P. A.; Wang, B.; O'Brien, R. E.; Kelly, S. T.; Laskin, A.; Gilles, M. K.; Moffet, R. C. *Journal of Geophysical Research: Atmospheres* **2014**, *119*(17), 10–365.

[197] Lienhard, D. M.; Huisman, A. J.; Krieger, U. K.; Rudich, Y.; Marcolli, C.; Luo, B.; Bones, D. L.; Reid, J. P.; Lambe, A. T.; Canagaratna, M. R.; others. *Atmospheric Chemistry and Physics* **2015**, *15*(23), 13599–13613.

[198] Ignatius, K.; Kristensen, T. B.; Järvinen, E.; Nichman, L.; Fuchs, C.; Gordon, H.; Herenz, P.; Hoyle, C. R.; Duplissy, J.; Garimella, S.; others. *Atmospheric Chemistry and Physics* **2016**, *16*(10), 6495–6509.

[199] Pruppacher, H. R.; James, D. *Aerosol Science and Technology* **1998**, *28*(4), 381–382.

[200] Bones, D. L.; Reid, J. P.; Lienhard, D. M.; Krieger, U. K. *Proceedings of the National Academy of Sciences* **2012**, *109*(29), 11613–11618.

[201] Murray, B. *Atmospheric Chemistry and Physics* **2008**, *8*(17), 5423–5433.

[202] Zobrist, B.; Marcolli, C.; Pedernera, D.; Koop, T. *Atmospheric Chemistry and Physics* **2008**, *8*(17), 5221–5244.

[203] Wilson, T.; Murray, B.; Wagner, R.; Möhler, O.; Saathoff, H.; Schnaiter, M.; Skrotzki, J.; Price, H.; Malkin, T.; Dobbie, S.; others. *Atmospheric Chemistry and Physics* **2012**, *12*(18), 8611–8632.

[204] Berkemeier, T.; Shiraiwa, M.; Pöschl, U.; Koop, T. *Atmospheric Chemistry and Physics* **2014**, *14*(22), 12513–12531.

[205] Seibert, P.; Frank, A. *Atmospheric Chemistry and Physics* **2004**, *4*(1), 51–63.

[206] Stohl, A.; Forster, C.; Frank, A.; Seibert, P.; Wotawa, G. *Atmospheric Chemistry and Physics* **2005**, *5*(9), 2461–2474.

[207] Owen, R.; Honrath, R. *Atmospheric Chemistry and Physics* **2009**, *9*(7), 2577–2595.

[208] Zhang, B.; Owen, R.; Perlinger, J.; Kumar, A.; Wu, S.; Val Martin, M.; Kramer, L.; Helmig, D.; Honrath, R. *Atmospheric Chemistry and Physics* **2014**, *14*(5), 2267–2287.

[209] Zhang, B.; Owen, R.; Perlinger, J.; Helmig, D.; Val Martín, M.; Kramer, L.; Mazzoleni, L.; Mazzoleni, C.; Chang, M. E.; Palmer, P. *Elementa: Science of the Anthropocene* **2017**, *5*.

[210] Moffet, R. C.; Rödel, T.; Kelly, S. T.; Yu, X.-Y.; Carroll, G.; Fast, J.; Zaveri, R. A.; Laskin, A.; Gilles, M. K. *Atmospheric Chemistry and Physics* **2013**, *13*(20), 10445–10459.

[211] Moffet, R. C.; Tivanski, A. V.; Gilles, M. K. *Signorell, R., Reid, JP, Eds* **2010**, pages 243–272.

[212] O'Brien, R. E.; Neu, A.; Epstein, S. A.; MacMillan, A. C.; Wang, B.; Kelly, S. T.; Nizkorodov, S. A.; Laskin, A.; Moffet, R. C.; Gilles, M. K. *Geophysical Research Letters* **2014**, *41*(12), 4347–4353.

[213] Fraund, M.; Park, T.; Yao, L.; Bonanno, D.; Pham, D. Q.; Moffet, R. C. *Atmospheric Measurement Techniques* **2019**, *12*(3), 1619–1633.

[214] Wang, B.; A. Knopf, D.; China, S.; W. Arey, B.; H. Harder, T.; K. Gilles, M.; Laskin, A. *Physical Chemistry Chemical Physics* **2016**, *18*(43), 29721–29731.

[215] Kärcher, B.; Ström, J. *Atmospheric Chemistry and Physics* **2003**, *3*(3), 823–838.

[216] Ervens, B. *Chemical reviews* **2015**, *115*(10), 4157–4198.

[217] Fraund, M.; Pham, D. Q.; Bonanno, D.; Harder, T. H.; Wang, B.; Brito, J.; De Sá, S. S.; Carbone, S.; China, S.; Artaxo, P.; others. *Atmosphere* **2017**, *8*(9), 173.

[218] Riemer, N.; West, M. *Atmospheric Chemistry and Physics* **2013**, *13*(22), 11423–11439.

[219] Gasparik, J.; Ye, Q.; Curtis, J.; Presto, A.; Donahue, N.; Sullivan, R.; West, M.; Riemer, N. *Aerosol Science and Technology* **2020**, *54*(12), 1527–1541.

[220] Pham, D. Q.; O'Brien, R.; Fraund, M.; Bonanno, D.; Laskina, O.; Beall, C.; Moore, K. A.; Forestieri, S.; Wang, X.; Lee, C.; others. *ACS Earth and Space Chemistry* **2017**, *1*(9), 551–561.

[221] Rothfuss, N. E.; Petters, M. D. *Environmental science & technology* **2017**, *51*(1), 271–279.

[222] Tomlin, J. M.; Jankowski, K. A.; Rivera-Adorno, F. A.; Fraund, M.; China, S.; Stirm, B. H.; Kaeser, R.; Eakins, G. S.; Moffet, R. C.; Shepson, P. B.; others. *ACS Earth and Space Chemistry* **2020**, *4*(11), 2171–2184.

[223] Wang, B.; Harder, T. H.; Kelly, S. T.; Piens, D. S.; China, S.; Kovarik, L.; Keiluweit, M.; Arey, B. W.; Gilles, M. K.; Laskin, A. *Nature géoscience* **2016**, *9*(6), 433–437.

[224] Cheng, Z.; Sharma, N.; Tseng, K.-P.; Kovarik, L.; China, S. *RSC Advances* **2021**, *11*(25), 15264–15272.

[225] Fraund, M.; Bonanno, D. J.; China, S.; Pham, D. Q.; Veghte, D.; Weis, J.; Kulkarni, G.; Teske, K.; Gilles, M. K.; Laskin, A.; others. *Atmospheric Chemistry and Physics* **2020**, *20*(19), 11593–11606.

[226] Reid, J. P.; Bertram, A. K.; Topping, D. O.; Laskin, A.; Martin, S. T.; Petters, M. D.; Pope, F. D.; Rovelli, G. *Nature communications* **2018**, *9*(1), 1–14.

[227] Schum, S. K.; Zhang, B.; Džepina, K.; Fialho, P.; Mazzoleni, C.; Mazzoleni, L. R. *Atmospheric Chemistry and Physics* **2018**, *18*(19), 14017–14036.

[228] Shiraiwa, M.; Li, Y.; Tsimpidi, A. P.; Karydis, V. A.; Berkemeier, T.; Pandis, S. N.; Lelieveld, J.; Koop, T.; Pöschl, U. *Nature communications* **2017**, *8*(1), 1–7.

[229] Whale, T. F.; Holden, M. A.; Wilson, T. W.; O'Sullivan, D.; Murray, B. J. *Chemical science* **2018**, *9*(17), 4142–4151.

[230] Knopf, D. A.; Alpert, P. A. *Faraday discussions* **2013**, *165*, 513–534.

[231] Niemand, M.; Möhler, O.; Vogel, B.; Vogel, H.; Hoose, C.; Connolly, P.; Klein, H.; Bingemer, H.; DeMott, P.; Skrotzki, J.; others. *Journal of the Atmospheric Sciences* **2012**, *69*(10), 3077–3092.

[232] Alpert, P. A.; Knopf, D. A. *Atmospheric Chemistry and Physics* **2016**, *16*(4), 2083–2107.

[233] Tobo, Y.; Adachi, K.; DeMott, P. J.; Hill, T. C.; Hamilton, D. S.; Mahowald, N. M.; Nagatsuka, N.; Ohata, S.; Uetake, J.; Kondo, Y.; others. *Nature Geoscience* **2019**, *12*(4), 253–258.

[234] Hoose, C.; Lohmann, U.; Bennartz, R.; Croft, B.; Lesins, G. *Atmospheric Chemistry and Physics* **2008**, *8*(23), 6939–6963.

[235] Adler, G.; Koop, T.; Haspel, C.; Taraniuk, I.; Moise, T.; Koren, I.; Heiblum, R. H.; Rudich, Y. *Proceedings of the National Academy of Sciences* **2013**, *110*(51), 20414–20419.

[236] Riemer, N.; Ault, A.; West, M.; Craig, R.; Curtis, J. *Reviews of Geophysics* **2019**, *57*(2), 187–249.

[237] Knopf, D.; Barry, K.; Brubaker, T.; Jahl, L.; Jankowski, KA, L.; Li, J.; Lu, Y.; Monroe, L.; Moore, K.; Rivera-Adorno, F.; others. *Bulletin of the American Meteorological Society* **2021**, pages 1–50.

[238] Froyd, K.; Murphy, D.; Lawson, P.; Baumgardner, D.; Herman, R. *Atmospheric Chemistry and Physics* **2010**, *10*(1), 209–218.

[239] Wolf, M. J.; Zhang, Y.; Zawadowicz, M. A.; Goodell, M.; Froyd, K.; Freney, E.;

Sellegri, K.; Rösch, M.; Cui, T.; Winter, M.; others. *Nature communications* **2020**, *11*(1), 1–9.

[240] Schill, G. P.; De Haan, D. O.; Tolbert, M. A. *Environmental science & technology* **2014**, *48*(3), 1675–1682.

[241] Abbatt, J.; Benz, S.; Cziczo, D.; Kanji, Z.; Lohmann, U.; Möhler, O. *Science* **2006**, *313*(5794), 1770–1773.

[242] Hinzman, L. D.; Deal, C. J.; McGuire, A. D.; Mernild, S. H.; Polyakov, I. V.; Walsh, J. E. *Ecological Applications* **2013**, *23*(8), 1837–1868.

[243] Johannessen, O. M.; Bengtsson, L.; Miles, M. W.; Kuzmina, S. I.; Semenov, V. A.; Alekseev, G. V.; Nagurnyi, A. P.; Zakharov, V. F.; Bobylev, L. P.; Pettersson, L. H.; others. *Tellus A: Dynamic Meteorology and Oceanography* **2004**, *56*(4), 328–341.

[244] Rigor, I. G.; Colony, R. L.; Martin, S. *Journal of Climate* **2000**, *13*(5), 896–914.

[245] Serreze, M. C.; Francis, J. A. *Climatic change* **2006**, *76*(3), 241–264.

[246] Graversen, R. G.; Mauritsen, T.; Tjernström, M.; Källén, E.; Svensson, G. *Nature* **2008**, *451*(7174), 53–56.

[247] Richter-Menge, J. A.; Farrell, S. L. *Geophysical Research Letters* **2013**, *40*(22), 5888–5893.

[248] Overland, J. E.; Wang, M. *Geophysical Research Letters* **2013**, *40*(10), 2097–2101.

[249] Arrigo, K. R.; van Dijken, G. L. *Progress in Oceanography* **2015**, *136*, 60–70.

[250] Tomasi, C.; Yamanouchi, T.; O'NEILL, N. T. *Atmospheric environment (1994)* **2012**, *52*.

[251] Tunved, P.; Ström, J.; Krejci, R. *Atmospheric Chemistry and Physics* **2013**, *13*(7), 3643–3660.

[252] Law, K. S.; Stohl, A. *science* **2007**, *315*(5818), 1537–1540.

[253] Law, K. S.; Stohl, A.; Quinn, P. K.; Brock, C. A.; Burkhart, J. F.; Paris, J.-D.; Ancellet, G.; Singh, H. B.; Roiger, A.; Schlager, H.; others. *Bulletin of the American Meteorological Society* **2014**, *95*(12), 1873–1895.

[254] Stone, R. S.; Sharma, S.; Herber, A.; Eleftheriadis, K.; Nelson, D. W.; Helmig, D.; Bottenheim, J. W. *Elementa: Science of the Anthropocene* **2014**, *2*.

[255] Quinn, P.; Miller, T.; Bates, T.; Ogren, J.; Andrews, E.; Shaw, G. *Journal of Geophysical Research: Atmospheres* **2002**, *107*(D11), AAC–8.

[256] Croft, B.; Martin, R. V.; Leaitch, W. R.; Tunved, P.; Breider, T. J.; D'Andrea, S. D.; Pierce, J. R. *Atmospheric Chemistry and Physics* **2016**, *16*(6), 3665–3682.

[257] Garrett, T. J.; Zhao, C. *Nature* **2006**, *440*(7085), 787–789.

[258] Maahn, M.; de Boer, G.; Creamean, J. M.; Feingold, G.; McFarquhar, G. M.; Wu, W.; Mei, F. *Atmospheric Chemistry and Physics* **2017**, *17*(23), 14709–14726.

[259] Köhler, H. *Transactions of the Faraday Society* **1936**, *32*, 1152–1161.

[260] Lowe, S. J.; Partridge, D.; Davies, J.; Wilson, K.; Topping, D.; Riipinen, I. *Nature communications* **2019**, *10*(1), 1–12.

[261] Seinfeld, J. H.; Pandis, S. N. *Atmospheric Chemistry and Physics: From Air Pollution to Climate Change;* John Wiley & Sons, 2016.

[262] Persson, P. O. G.; Fairall, C. W.; Andreas, E. L.; Guest, P. S.; Perovich, D. K. *Journal of Geophysical Research: Oceans* **2002**, *107*(C10), SHE–21.

[263] Willis, M. D.; Bozem, H.; Kunkel, D.; Lee, A. K.; Schulz, H.; Burkart, J.; Aliabadi, A. A.; Herber, A. B.; Leaitch, W. R.; Abbatt, J. P. *Atmospheric Chemistry and Physics* **2019**, *19*(1), 57–76.

[264] Kipling, Z.; Stier, P.; Schwarz, J.; Perring, A.; Spackman, J.; Mann, G.; Johnson, C.; Telford, P. *Atmospheric Chemistry and Physics* **2013**, *13*(12), 5969–5986.

[265] Wang, Q.; Jacob, D. J.; Spackman, J. R.; Perring, A. E.; Schwarz, J. P.; Moteki, N.; Marais, E. A.; Ge, C.; Wang, J.; Barrett, S. R. *Journal of Geophysical Research: Atmospheres* **2014**, *119*(1), 195–206.

[266] Kipling, Z.; Stier, P.; Johnson, C. E.; Mann, G. W.; Bellouin, N.; Bauer, S. E.; Bergman, T.; Chin, M.; Diehl, T.; Ghan, S. J.; others. *Atmospheric Chemistry and Physics* **2016**, *16*(4), 2221–2241.

[267] Wilcox, E. *Atmospheric Chemistry and Physics* **2012**, *12*(1), 139–149.

[268] Hirdman, D.; Burkhart, J. F.; Sodemann, H.; Eckhardt, S.; Jefferson, A.; Quinn, P. K.; Sharma, S.; Ström, J.; Stohl, A. *Atmospheric Chemistry and Physics* **2010**, *10*(19), 9351–9368.

[269] Ervens, B.; Sorooshian, A.; Aldhaif, A. M.; Shingler, T.; Crosbie, E.; Ziemba, L.; Campuzano-Jost, P.; Jimenez, J. L.; Wisthaler, A. *Atmospheric Chemistry and Physics* **2018**, *18*(21), 16099–16119.

[270] Fu, Y.; Lin, Q.; Zhang, G.; Yang, Y.; Yang, Y.; Lian, X.; Peng, L.; Jiang, F.; Bi, X.; Li, L.; others. *Atmospheric Chemistry and Physics* **2020**, *20*(22), 14063–14075.

[271] Gunsch, M. J.; Kirpes, R. M.; Kolesar, K. R.; Barrett, T. E.; China, S.; Sheesley, R. J.; Laskin, A.; Wiedensohler, A.; Tuch, T.; Pratt, K. A. *Atmospheric Chemistry and Physics* **2017**, *17*(17), 10879–10892.

[272] Springston, S. *DOE ARM Climate Research Facility: Washington, DC, USA* **2018**.

[273] Prospero, J.; Glaccum, R.; Nees, R. *Nature* **1981**, *289*(5798), 570–572.

[274] Oades, J. M. In *Soil structure/soil biota interrelationships;* Elsevier, 1993; pages 377–400.

[275] Simoneit, B. R.; Elias, V. O.; Kobayashi, M.; Kawamura, K.; Rushdi, A. I.; Medeiros, P. M.; Rogge, W. F.; Didyk, B. M. *Environmental Science & Technology* **2004**, *38*(22), 5939–5949.

[276] O'Sullivan, D.; Murray, B.; Malkin, T.; Whale, T. F.; Umo, N. S.; Atkinson, J.; Price, H.; Baustian, K. J.; Webb, M. E.; others. *Atmospheric Chemistry and Physics* **2014**, *14*(4), 1853–1867.

[277] Xu, L.; Lio, A.; Hu, J.; Ogletree, D. F.; Salmeron, M. *J. Phys. Chem. B* **1998**, *102*(3), 540–548.

[278] Gaines Jr, G. L. *J. Phys. Chem.* **1957**, *61*(10), 1408–1413.

[279] Woodward, X.; Kostinski, A.; China, S.; Mazzoleni, C.; Cantrell, W. *Aerosol Sci. Technol.* **2015**, *49*(4), 229–238.

[280] Niehaus, J.; Bunker, K. W.; China, S.; Kostinski, A.; Mazzoleni, C.; Cantrell, W. *J. Atmos. Ocean. Technol.* **2014**, *31*(4), 913–922.

[281] Zobrist, B.; Koop, T.; Luo, B.; Marcolli, C.; Peter, T. *J. Phys. Chem. C* **2007**, *111*(5), 2149–2155.

[282] Richardson, S.; Richardson, J. J. *Am. Mineral.; (United States)* **1982**, *67:1-2*, 69–75.

[283] Cygan, R. T.; Liang, J.-J.; Kalinichev, A. G. *The Journal of Physical Chemistry B* **2004**, *108*(4), 1255–1266.

[284] Abascal, J. L. F.; Sanz, E.; García Fernández, R.; Vega, C. *J. Chem. Phys.* **2005**, *122*(23), 234511.

[285] Lorentz, H. A. *Annalen der Physik* **1881**, *248*(1), 127–136.

[286] Bussi, G.; Donadio, D.; Parrinello, M. *The Journal of chemical physics* **2007**, *126*(1), 014101.

[287] Berk, H.; Henk, B.; Herman, B. J. C.; Johannes, F. G. E. M. *J. Comput. Chem.* **1997**, *18*(12), 1463–1472.

[288] Essmann, U.; Perera, L.; Berkowitz, M. L.; Darden, T.; Lee, H.; Pedersen, L. G. *J. Chem. Phys.* **1995**, *103*(19), 8577–8593.

[289] Pronk, S.; Páll, S.; Schulz, R.; Larsson, P.; Bjelkmar, P.; Apostolov, R.; Shirts, M. R.; Smith, J. C.; Kasson, P. M.; van der Spoel, D.; Hess, B.; Lindahl, E. *Bioinformatics* **2013**, *29*(7), 845–854.

[290] Abraham, M. J.; Murtola, T.; Schulz, R.; Páll, S.; Smith, J. C.; Hess, B.; Lindahl, E. *SoftwareX* **2015**, *1-2*, 19 – 25.

[291] Páll, S.; Abraham, M. J.; Kutzner, C.; Hess, B.; Lindahl, E. In Markidis, S., Laure, E., Eds., *Solving Software Challenges for Exascale*, pages 3–27, Cham, 2015. Springer International Publishing.

[292] Berendsen, H. J. C.; Postma, J. P. M.; van Gunsteren, W. F.; DiNola, A.; Haak, J. R. *J. Chem. Phys.* **1984**, *81*(8), 3684–3690.

[293] Parrinello, M.; Rahman, A. *J. Appl. Phys* **1981**, *52*(12), 7182–7190.

[294] Kaiser, J.; Heil, A.; Andreae, M.; Benedetti, A.; Chubarova, N.; Jones, L.; Morcrette, J.-J.; Razinger, M.; Schultz, M.; Suttie, M.; others. *Biogeosciences* **2012**, *9*(1), 527–554.

[295] Kilcoyne, A.; Tyliszczak, T.; Steele, W.; Fakra, S.; Hitchcock, P.; Franck, K.; Anderson, E.; Harteneck, B.; Rightor, E.; Mitchell, G.; others. *Journal of synchrotron radiation* **2003**, *10*(2), 125–136.

[296] Hopkins, R. J.; Tivanski, A. V.; Marten, B. D.; Gilles, M. K. *Journal of Aerosol Science* **2007**, *38*(6), 573–591.

[297] Tivanski, A. V.; Hopkins, R. J.; Tyliszczak, T.; Gilles, M. K. *The Journal of Physical Chemistry A* **2007**, *111*(25), 5448–5458.

[298] O'Brien, R. E.; Wang, B.; Laskin, A.; Riemer, N.; West, M.; Zhang, Q.; Sun, Y.; Yu, X.-Y.; Alpert, P.; Knopf, D. A.; others. *Journal of Geophysical Research: Atmospheres* **2015**, *120*(18), 9591–9605.

[299] Henke, B. L.; Gullikson, E. M.; Davis, J. C. *Atomic data and nuclear data tables* **1993**, *54*(2), 181–342.

[300] Laskin, A.; Cowin, J. P.; Iedema, M. J. *Journal of Electron Spectroscopy and Related Phenomena* **2006**, *150*(2-3), 260–274.

[301] Riemer, N.; West, M.; Zaveri, R. A.; Easter, R. C. *Journal of Geophysical Research: Atmospheres* **2009**, *114*(D9).

[302] DeRieux, W.-S. W.; Li, Y.; Lin, P.; Laskin, J.; Laskin, A.; Bertram, A. K.; Nizkorodov, S. A.; Shiraiwa, M. *Atmospheric Chemistry and Physics* **2018**, *18*(9), 6331–6351.

[303] Shakya, K. M.; Liu, S.; Takahama, S.; Russell, L. M.; Keutsch, F. N.; Galloway, M. M.; Shilling, J. E.; Hiranuma, N.; Song, C.; Kim, H.; others. *Aerosol Science and Technology* **2013**, *47*(5), 543–555.

[304] Moffet, R. C.; Henn, T.; Laskin, A.; Gilles, M. K. *Analytical chemistry* **2010**, *82*(19), 7906–7914.

Appendix A

Permission

A.1 License Information for Chapter 2

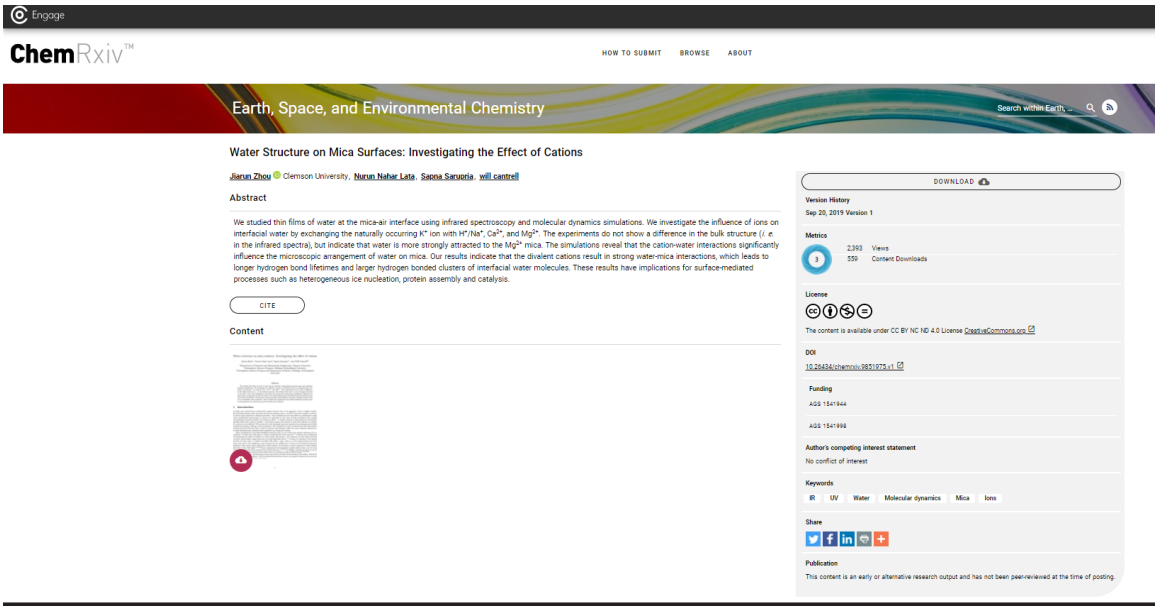

A.2 Permission for Chapter 3

Permission to use copyrighted material from the Journal of Physical Chemistry Let-

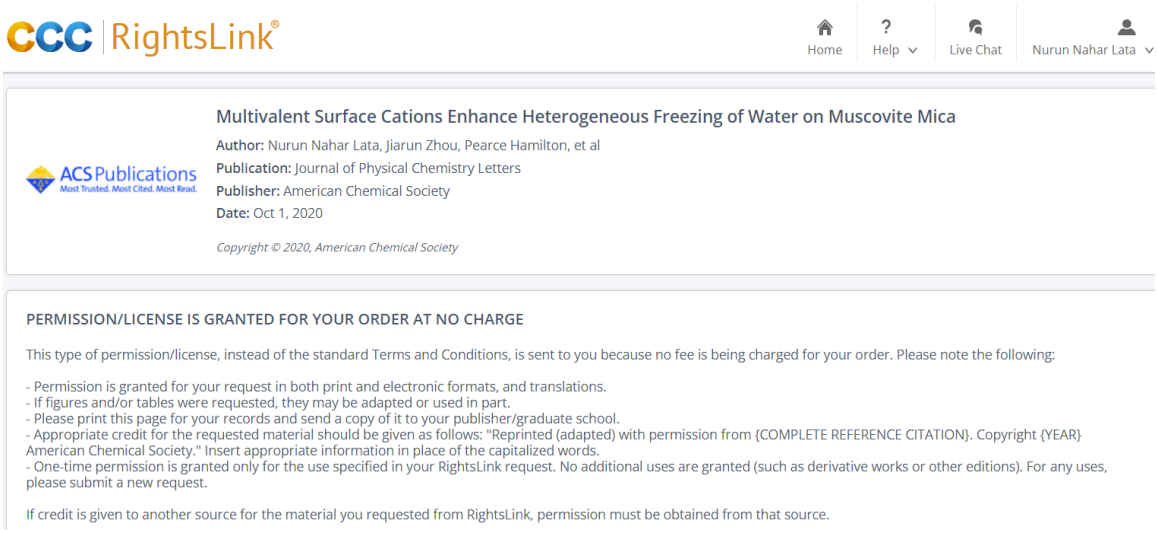

A.3 Permission for Chapter 4

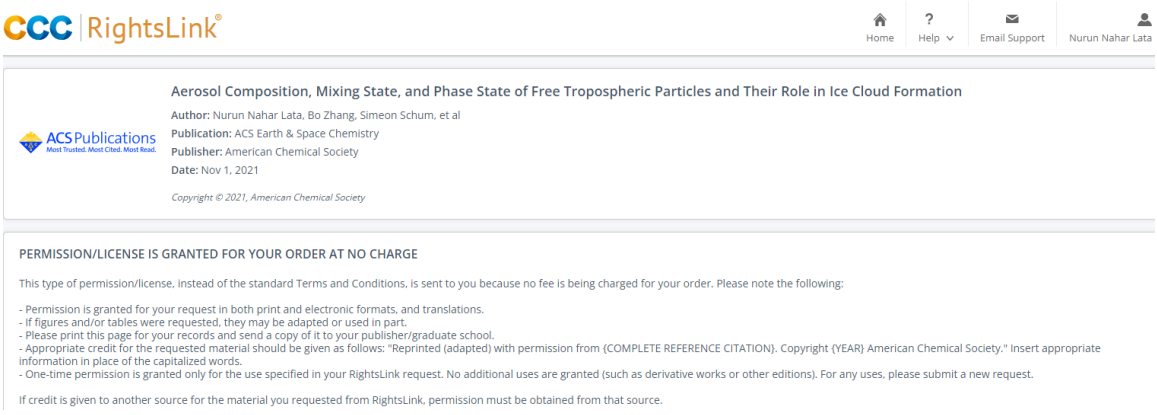

Appendix B

Supplementary

B.1 Supplementary Information of Chapter 3

B.1.1 Variability of micas from different sources

Because mica is a natural substance, with some variability in composition from source to source, we tested samples from three different suppliers to verify that our results are representative. Surface roughness measurements for K^+-mica and Mg^{2+}-mica from all three suppliers show no significant change in surface roughness. (See below for further discussion of surface roughness.) Table B.1 shows the surface areas of 1 μL droplets on freshly cleaved mica (K^+) from Tarheel Mica Co., Axim Mica Co., and Asheville Mica Co. (See main text and below for a more detailed discussion of surface area.) The surface areas of water droplets on K^+-mica from different resources are the same within the uncertainty of the measurements. All show that water spreads

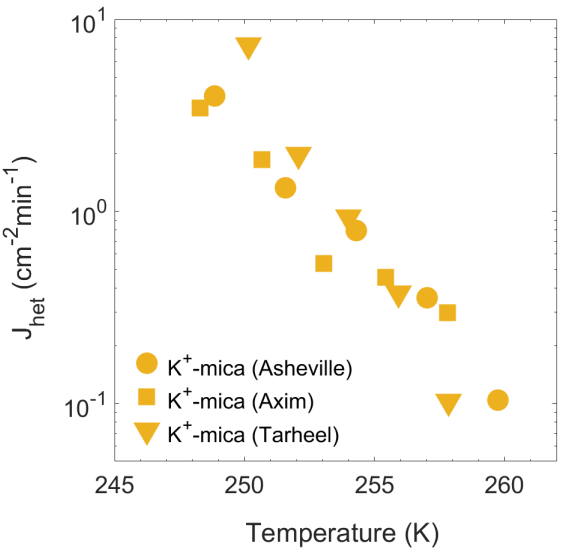

Figure B.1: Heterogeneous nucleation rate coefficient on different supplier's K^+-mica. Note we have used a time base of minutes, not seconds, for J_{het}.

into a thin pancake, consistent with previous measurements of a contact angle less than 3° [107, 124, 277]. Note that mica is a high energy surface, and the contact angle of water increases with age as contaminants from the ambient atmosphere adsorb to the surface.

Table B.1
Surface area of 1 μL water droplet on different sources of K^+-mica

Source of K^+-mica	Surface area of droplet (cm^2)
Asheville	0.31± 0.01
Axim	0.303± 0.008
Tarheel	0.297±0.002

Figure B.1 is a plot of the heterogeneous nucleation rate coefficient, J_{het}, for K^+-mica from Asheville, Axim, and Tarheel Mica Cos. (A more detailed discussion of J_{het} is below.) The figure indicates that liquid water nucleates to ice over a wide range of temperatures, but that the freezing rates on mica from the different suppliers are

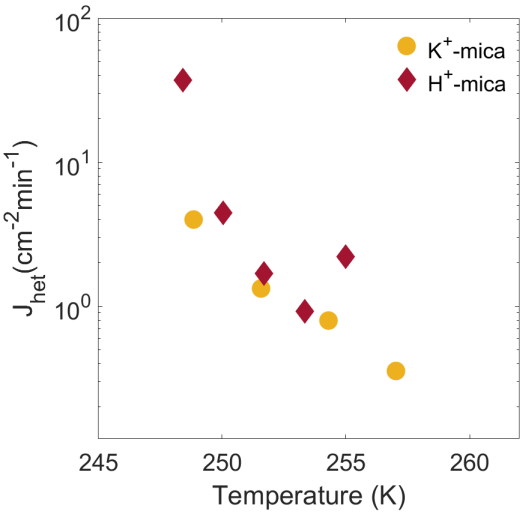

Figure B.2: Heterogeneous nucleation rate coefficient on K^+ and H^+-mica.

similar. Our measurements are also consistent with the finding that mica is not a good freezing catalyst. At 253 K, we see approximately one freezing event every three minutes.

We have also measured J_{het} on mica that has simply been rinsed with pure water, thus replacing the K^+ ions with H^+ [60]. Figure B.2 shows no significant difference in the heterogeneous nucleation rate coefficients for the two surfaces.

B.1.2 Ion Exchange

The mica samples were cleaved along the basal plane and treated with salt solutions to exchange the surface ions. The treated surfaces were then rinsed with water to remove the counter ions from the salt solution, leaving a surface with K^+ ions exchanged for divalent or trivalent ions (preserving charge neutrality). We used 0.1 M $MgSO_4$ (Sigma Aldrich), saturated $CaSO_4$ (Sigma Aldrich), 0.1 M $SrCl_2$ (Acros Chemical)

and 0.1 M anhydrous $AlCl_3$ (Acros Chemical) solutions to get Mg^{2+}, Ca^{2+}, Sr^{2+} and Al^{3+}-mica, respectively. The treatment time was 20 to 25 minutes. Previous studies showed soaking the mica sheets in salt solution only for few minutes can completely exchange the surface cations [60, 81, 278] whereas inter layer cation exchange takes a few days soaking time [278]. After rinsing, the treated mica sheets were dried at room temperature, covered in a Petri dish; the dried samples were then ready for experiments.

As a further check on our procedure, we analyzed some samples using a PHI 5800 X-ray photoelectron spectrophotometer (XPS). The X-ray source used during analysis was either a non-monochromatic Mg source (1254 eV) or a non-monochromatic Al source (1487 eV). A neutralizer was used for charge correction to supply low energy (6 eV) electrons to the surface. The analysis area has a nominal 800 μm diameter. Data was collected with the sample at an angle of 45 degrees to the detector. For survey scans a pass energy of 187.85 eV was used with a resolution of 0.8 eV/step and a dwell time of 20 ms/step. For high resolution spectra a pass energy of 23.50 eV was used with a resolution of 0.1 eV/step and a dwell time of 100 ms/step.

Figure B.3 shows a comparison spectrum of a K^+-mica surface (*i.e.* untreated) with an Mg^{2+}-mica surface. It is clear from the figure that the intensity of peak at 294 eV (K) is reduced while at the same time a new peak at 1305 eV (Mg) appears. This indicates a successful surface ion exchange reaction which is consistent with the

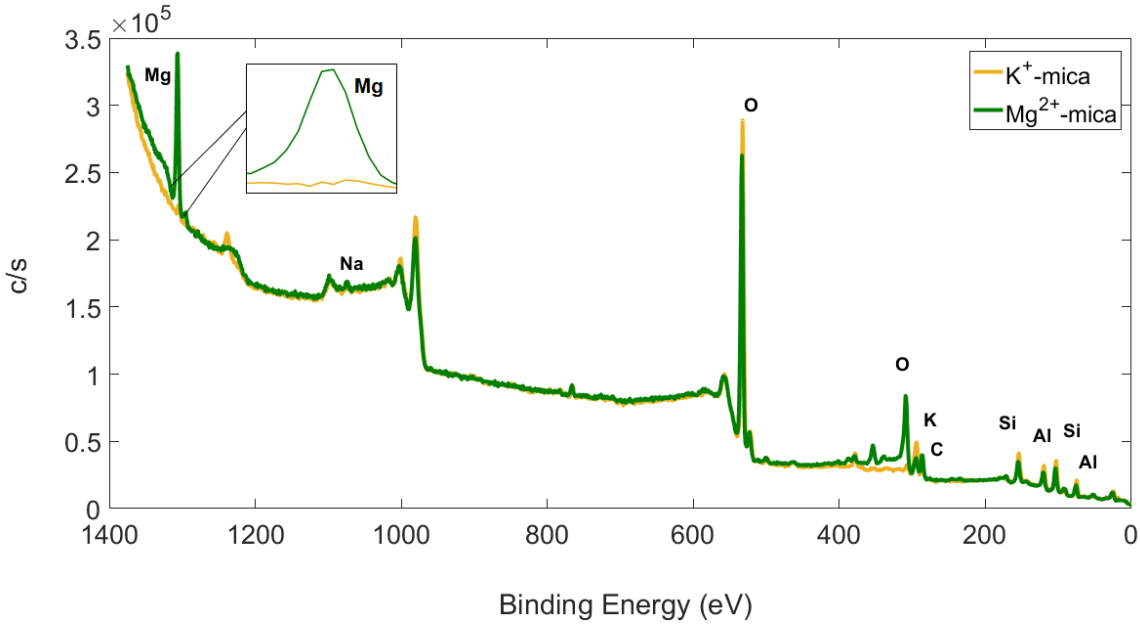

Figure B.3: XPS spectra of K^+-mica and Mg^{2+}-mica. The inset shows the zoomed Mg peak (green). The appearance of a new peak at 1305 eV (green) indicates the presence of Mg which is absent in case of the K^+-mica (yellow), indicating successful ion exchange.

result obtained by Xu and Salmeron [60]. They observed complete exchange of ions by immersing natural mica in a salt solution. Note that though the exchange process is completed, the K peak has not completely disappeared. This is because XPS is a surface sensitive technique, but the detection depth can be more than 2 nm, which is approximately two layers of mica [60]. The depleted K peak we are observing is coming from subsurface layers, where the ions are not exchanged [278].

B.1.3 Surface Area of Droplets

To measure the surface area of droplets on the mica, we deposit a 1 μl droplet on the surface, either freshly cleaved in the case of the K^+-mica or ion exchanged and dried for the others. The droplet on the surface is a hemisphere. We make repeated

measurements of the diameter of the hemisphere, D_h, with a caliper, then compute the surface area of the droplet in contact with the substrate as $\pi \left(\frac{D_h}{2}\right)^2$. We measured 2-3 diameters for each of the drop and measured 6-10 droplets on different cation exposed mica surfaces. That quantity is reported in Table 1 in the main text.

B.1.4 Characterization of (lack of) Surface Roughness

To characterize any changes in surface roughness due to the ion replacement process, some of the prepared samples were imaged with a Nanosurf Easyscan 2 Atomic Force Microscope using a silicon SHOCON probe. The AFM scanned 2048 lines over a 10 μm $\times$ 10 μm area of the surface, resulting in an image that records the measured sample height for each 10 μm/2048 $\sim$5 nm$\times$5 nm pixel.

Our first measure of surface smoothness is a calculation of the RMS roughness for the samples. (See Woodward et al. [279] for a detailed discussion of RMS roughness and features on a substrate.) The median height is subtracted from each image and the residual recorded height above or below the median is squared and then summed over all 2048^2 pixels. The resulting sum's square root is recorded as the RMS roughness on a 5 nm scale. The comparison in surface roughness between a K^+-mica surface and an Mg^{2+}-mica surface reveals a very small change. To determine if this small change is statistically significant, the same procedure was done for 64 disjoint 1.25 μm $\times$ 1.25 μm sub-domains of the 10 μm $\times$ 10 μm image (each sub-domain having its own median measured sample height), so that a statistical uncertainty could be

estimated for the measurement based on the standard deviation among the 64-member ensemble. Finally, each of the 1.25 μm sub-domains was box-filtered (box-blurred) with a uniform 3×3 filter to smooth any features on scales between 5 nm and 15 nm; the sub-domain images were then subtracted from the box-filtered images and summed over the 256^2 pixels in the sub-domain. The resulting sum's square root was recorded as the box-filtered RMS roughness on a 5 nm scale, essentially giving a high-pass-filtered estimate of the local roughness in each 1.25 μm domain for scales between 5 nm and 15 nm. These 64 local roughness measurements were combined to form a separate ensemble with its own statistical uncertainty and compared between the K^+-mica and the Mg^{2+}-mica. The three separate methods of measuring surface roughness are all commensurate with no meaningful statistical difference in the surface roughness between the two samples. Note that the procedure just described is also a measure of local roughness and shows that the surface is locally as well as globally smooth.

To reconfirm that point, we analyze the ensemble of linear scans with the AFM. In this procedure, each line scan is compared to a 5-point moving average filtered version of itself; the resulting smoothed line-scan is subtracted from the raw data. This procedure acts as a high-pass filter. The 2048 line differences are then combined to form a frequency histogram. If small-scale features are present, the histogram of differences will show a significant width because of local (5 point) variations in the surface topography.

Figure B.4 is a plot of the histograms for the K^+ data (left) and the Mg^{2+} data (right). It is clear that the local height variability as detected by the AFM is minimal on scales relevant to nucleation. It is also clear that the two surfaces have essentially the same level of smoothness. The similarity between the two histograms is remarkable.

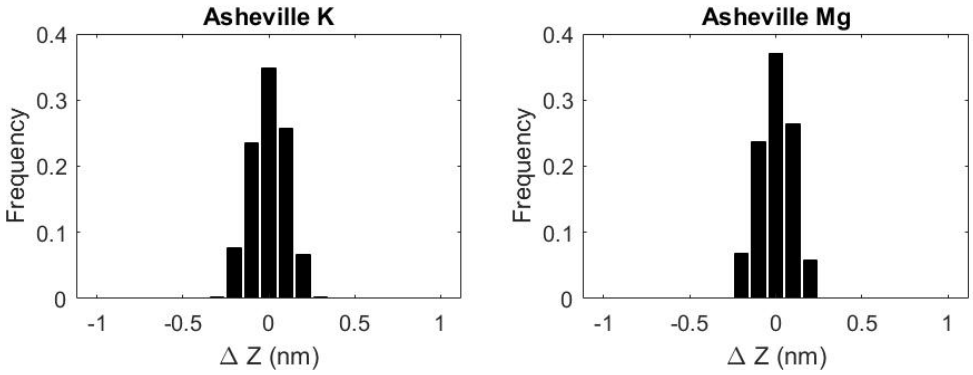

Figure B.4: Histograms of the residuals of local deviations from surface topography for the K^+-mica and the Mg^{2+}-mica. The remarkable similarity in the histograms shows that the two surfaces are similarly smooth.

As a final check on the similarity of surface smoothness between the two surfaces, we computed the average magnitude of the slope observed in the two processed images as a function of spatial scale. To obtain these plots, the value of $\frac{|(\Delta z)|}{\Delta x}$ was computed for different values of Δx. (x is the axis parallel to the line-scan direction, and z is the height of the sample.) Surface roughness localized at a given scale would manifest as a larger value of the slope. The initial values of ≈ 0.025 shows that the mean difference in height between two adjacent AFM measurement points is less than a tenth of a nanometer.

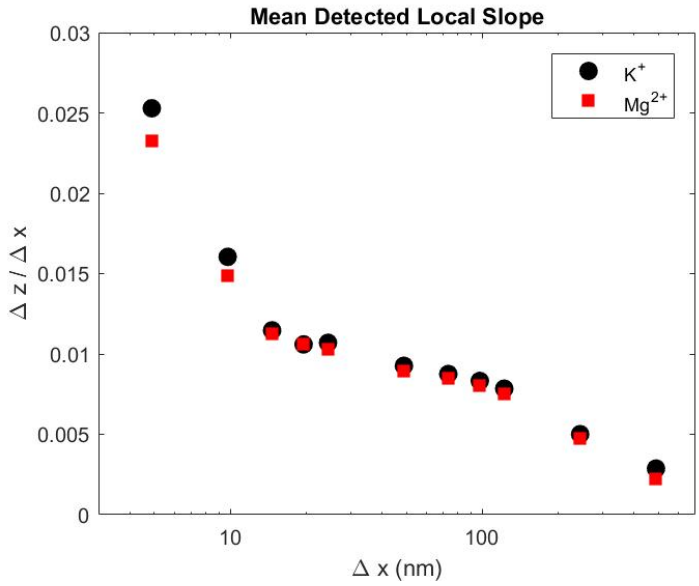

Figure B.5: Mean slope as a function of spatial scale in the line-scan direction of the AFM for the two samples. Surface roughness would manifest a difference in this quantity. Both samples have essentially the same mean roughness at all scales, though the mean slope decreases as the spatial scale increases, as expected.

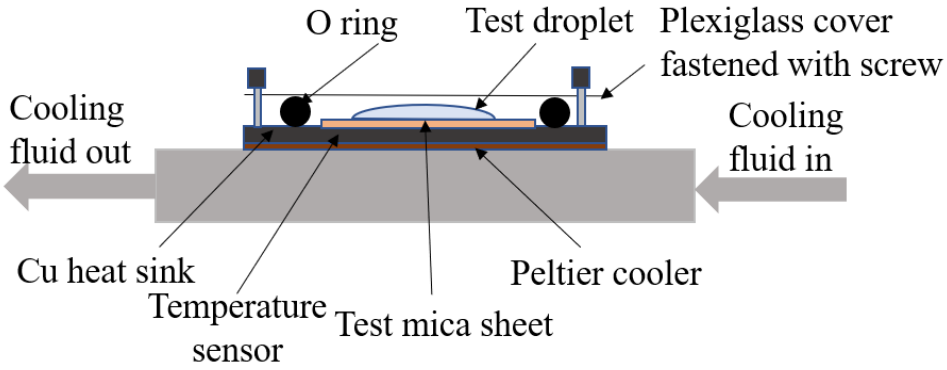

Figure B.6: Schematic of the cold stage used for drop freezing experiments.

B.1.5 Ice Nucleation Experiments

A custom built cold stage, shown schematically in Figure B.6 is used to observe ice nucleation. It is a simplified version of the stage described in Niehaus et al., 2014

[280]. A 0.3 mm thick copper plate is assembled on the top of a Peltier cooler. A platinum resistance thermometer (Minco) embedded within the copper plate enables temperature control of a test droplet via an Accuthermo FTC100D TEC temperature controller. The top of the cold stage is covered with grooved plexiglass fitted with an O-ring seal to isolate the test droplet from the atmosphere. A thin layer of vacuum grease is spread on the top of the cold stage before putting mica sheets on it so that there is no air gap between the mica and the cold stage. All data reported here are from tests using a 1 μL volume droplet, placed on the basal plane of the mica. The test droplet was cooled at 1.43 K min^{-1}. Droplet freezing was observed with the help of a microscope camera; the magnified image of the droplet was projected onto a monitor and the phase transition is detected by eye as a marked change in the droplet's transparency. To ensure that drop freezing was correctly identified in this manner, in some cases where drop freezing was observed, the top of the chamber was removed and the droplet was prodded with a metal pick. In all cases, the droplet was solid (*i.e.* it had indeed frozen). We observed only one droplet freezing at a time because a 1 μL water droplet covers $\sim$ 0.3 cm^2 on K^+-mica. We observed repeated freezing events ($\sim$ 10) of a single drop of water, then repeated the experiment with a different sheet of the mica. Each series in the plot of J_{het} vs. T represents at least 50 trials.

B.1.6 Heterogeneous Freezing Rate Coefficient

From the freezing temperature data and the measured contact area of the droplets with the mica surface, we calculate the heterogeneous freezing rate coefficient. (Note that comparison of the frozen fraction of droplets is misleading because droplets spread to cover more or less of the surface, depending on the exposed ion.) The nucleation rate is given by

$$\omega_{het} = \frac{N_f}{t_{tot}} \tag{B.1}$$

where N_f is the number of freezing events within the observation time, t_{tot}. For experiments in which the temperature is continuously changing, Eqn B.1 can still be used to determine the nucleation rate within the ith temperature interval using, [281]

$$t^i_{tot} = \frac{\Delta T}{c}\left(N^i_{unfrz} - N^i_f\right) + \sum_{j=1}^{N^i_f} \Delta t_{f,j} \tag{B.2}$$

where ΔT is the width of the temperature interval, c is the cooling rate, N^i_{unfrz} is the number of unfrozen droplets at the beginning of the interval, N^i_f is the number of droplets that froze within the interval, and $\Delta t_{f,j}$ is the time that it took the jth droplet to freeze in the interval. The heterogeneous freezing rate coefficient is then

$$J_{het}(T^i) = \frac{\omega_{het}(T^i)}{A_{drop}}. \tag{B.3}$$

A_{drop} is the area of contact between the liquid water droplet and the substrate.

B.1.7 Molecular dynamics (MD) simulations

MD simulations of water film on the mica surfaces were performed at 243.5 K in the NVT ensemble. Mica crystal structure was imported from American Mineralogist Crystal Structure Database [282]. The chemistry formula for the unit cell is $KAl_2(Si_3Al)O_{10}(OH)_2$. Si was substituted with Al with a Si:Al ratio of 3:1. This was achieved through randomly substituting the Si atoms to Al atoms in the crystal structure. It was ensured that no two Al atoms were connected through a bridging oxygen atom. The substitution creates a net negative charge that attracts cations. Initially, cations, regardless of types, were placed in the voids created by Si/Al and the bridging oxygen atoms. The ions were placed randomly on the mica surface and were free to diffuse during the simulations.

The MD simulation systems comprised of a mica sheet with a water layer placed on top of the surface. There was vacuum above the water layer and a repulsive wall placed at the edge of the simulation box to prevent the water molecules from diffusing across the box to the other side of the mica surface. The water layer on mica was about 4 nm thick with 5000 water molecules. The box dimensions were 6.2 $\times$ 7.2 $\times$ 20 nm^3, with the z-direction normal to the mica surface. The repulsive wall was placed at least 8 nm away from the surface. The mica surface comprised 96 mica unit cells. CLAYFF force field [283] was used to describe the surface. TIP4P/Ice water model [284], which predicts the correct freezing point for water, was used to describe

the water molecules. Lorentz-Berthelot mixing rules [285] were used for water-surface (including water-ion) cross interactions. The repulsive wall comprised of atoms with no partial charge and Lennard Jones parameters $\sigma = 0.356$ nm and $\epsilon = 0.293$ kJ/mol.

All the MD simulations were performed in the NVT ensemble at 243.5 K for 220 ns. The temperature was annealed from 300 K to 243.5 K in the first 10 ns. During the simulation, atoms in mica surface except the cations were held fixed, i.e the mica surface except the cations was effectively at 0 K. The cations were free to diffuse. Temperature was controlled using the V-rescale [286] thermostat with a time constant of 2 ps. The water molecules and mica surface were coupled to different thermostats at reference temperature of 243.5 K. The LINCS [287] algorithm was used to maintain the water geometry and Particle Mesh Ewald (PME) [288] method was applied to calculate the electrostatic interactions. We used a time step of 2 fs. Configurations were stored every 10 ps and we used the last 120 ns of 220 ns for all the analysis. For each system, three simulations were performed by randomizing the molecular velocities of the atoms in the system. All simulations were performed using Gromacs 2018.3 [289, 290, 291].

B.1.8 Calculation of hydrogen bonded clusters of water molecules

We performed calculations to identify clusters of hydrogen bonded water molecules. To this end, we first identified the hydrogen bonded water molecules. After the

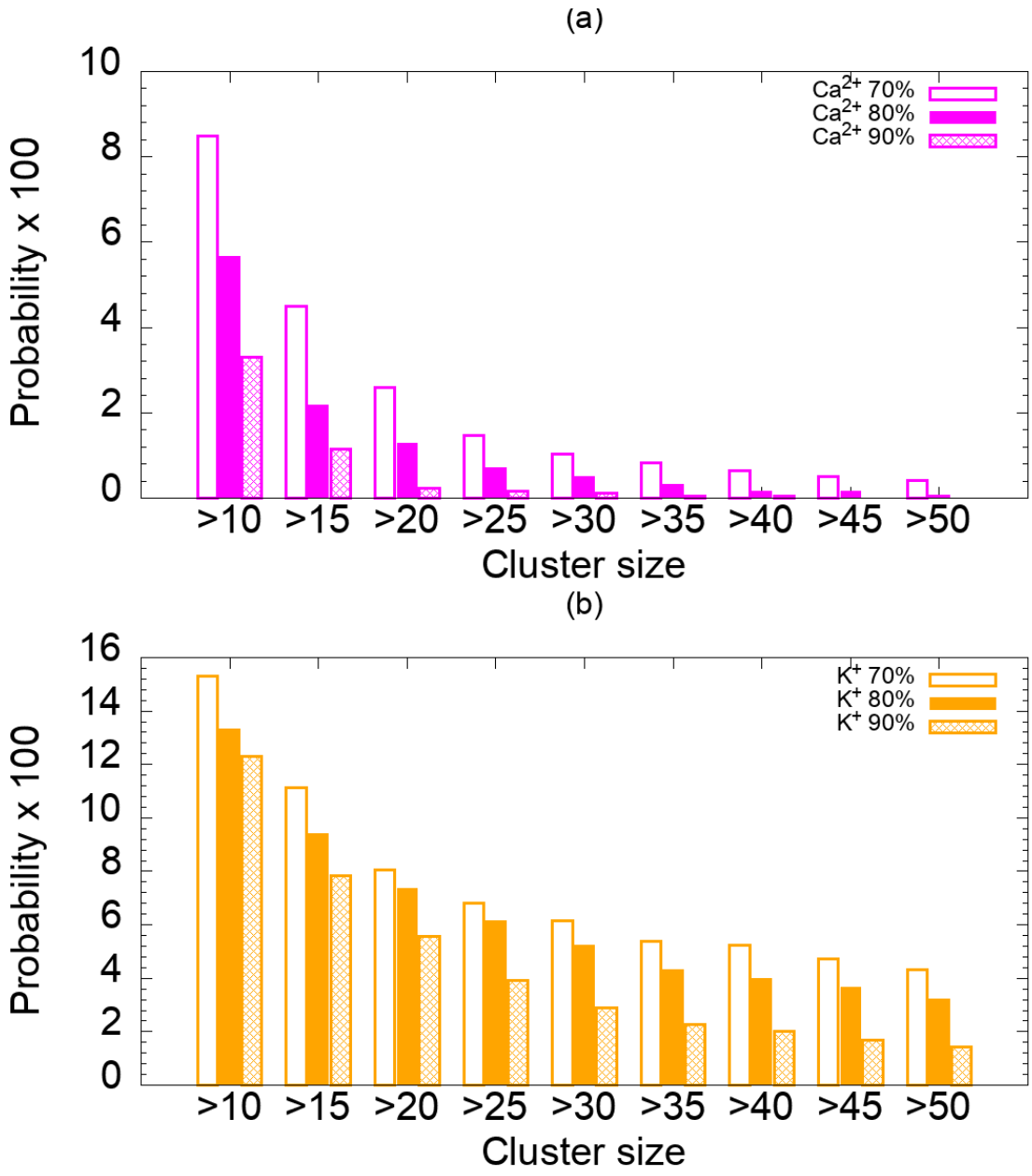

Figure B.7: Probability of observing clusters greater than a given size on Ca^{2+}-mica (a) and K^{+}-mica (b) with $\overline{h_{ij}} > 0.7$, $\overline{h_{ij}} > 0.8$, and $\overline{h_{ij}} > 0.9$ criteria.

hydrogen bonded water molecules were identified, clusters formed by those were found using Cytoscope (a network analysis software) [146]. Geometric criteria were used for identifying the hydrogen bonds between water molecules. To reduce the effect

of thermal fluctuations we adapted the definition of history independent hydrogen bonds as proposed by Stanley and coworkers [144]. We divided our 100 ns production simulation into 10 observation windows of 2 ns each. We identified those hydrogen bonds that existed for 80% of the frames in this 2 ns window. In this definition, the bonds do not need to exist continuously. This criteria can be described as

$$\overline{h_{ij}} = \frac{1}{Nc} \sum_{t=1}^{Nc} h_{ij}(t) \tag{B.4}$$

where

$$h_{ij} = \begin{cases} 1 & \text{if there is a hydrogen bond between molecules } i \text{ and } j \\ 0 & \text{otherwise} \end{cases}$$

and N_C is the number of configurations in the observation window. If $\overline{h_{ij}} > 0.8$, then it is considered that atoms i and j are hydrogen bonded in the observation window and used for further cluster analysis. We also evaluated the effect of changing this criteria to $\overline{h_{ij}} > 0.7$ and $\overline{h_{ij}} > 0.9$. As expected, with the less strict criterion (i.e. $\overline{h_{ij}} > 0.7$) more clusters are identified. However, the trends observed in the distribution of cluster size with charge on the ions remains consistent, as seen in Fig. B.7. Thus, this criteria does not affect the discussion and conclusion in the manuscript.

To evaluate the effect of the length of the observation window, we performed the analysis for observation windows of 0.5, 1, 2 and 5 ns. Given the criteria above (i.e.

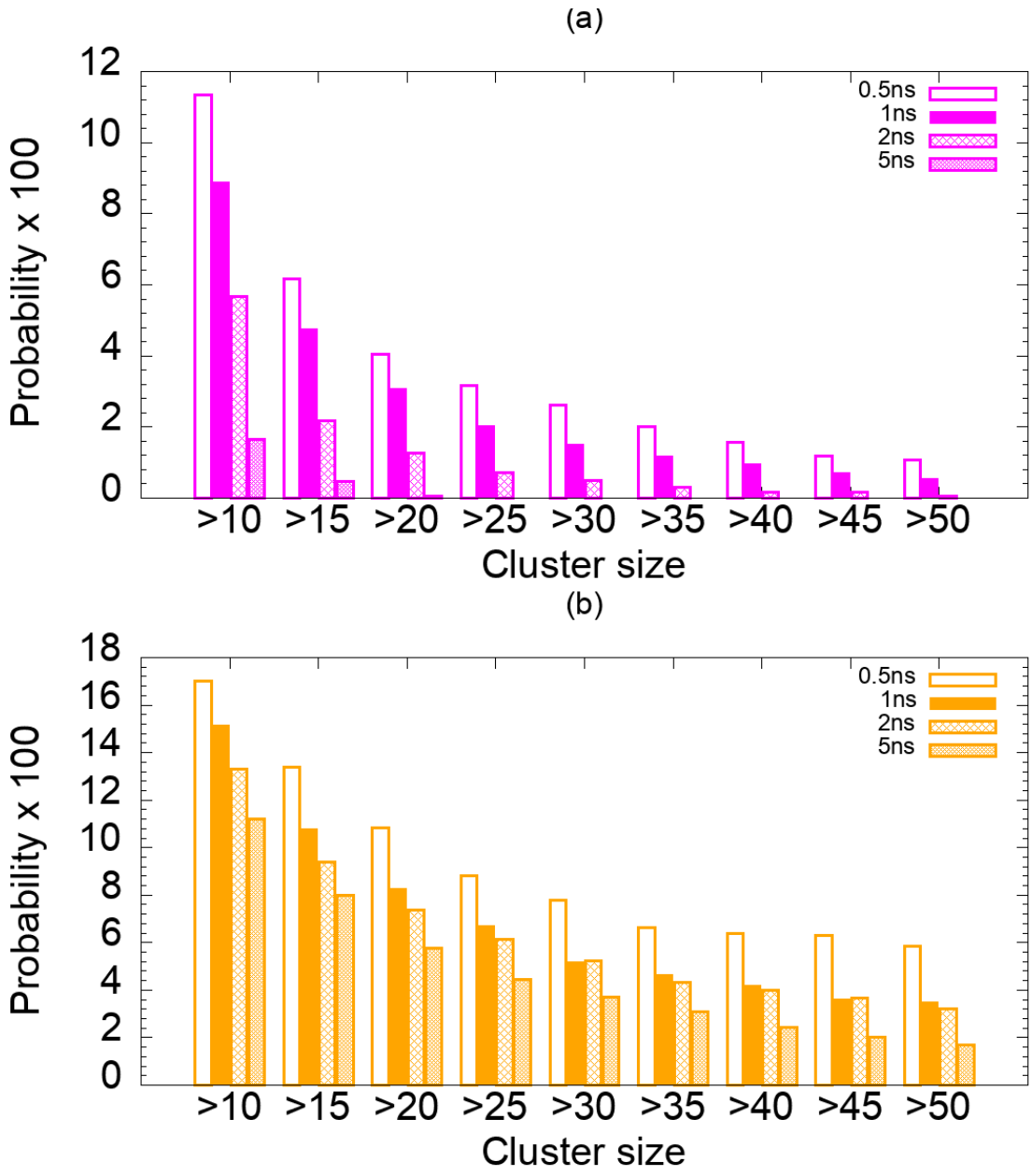

Figure B.8: Probability of observing clusters greater than a given size on (a) Ca^{2+}-mica and (b) K^{+}-mica using different lengths of observation windows. $\overline{h_{ij}} > 0.8$ criteria was used for all these calculations.

of $\overline{h_{ij}} > 0.8$) it could be considered that the condition for being hydrogen bonded gets stricter with increasing length of observation window. As expected, larger number of clusters are observed with less strict criterion. Again, the trends across the cations

however, remain consistent for all observation window lengths. See Figs. B.8(a) and (b). We thus focus on the results from the 2 ns observation window. This gives us a balance between identifying relatively longer lived clusters and sufficient sampling. The results presented in the main text are for 2 ns observation window and are averaged over ten windows – 110-112, 120-122, 130-132, 140-142, 150-152, 160-162, 170-172, 180-182, 190-192, and 200-202 ns.

B.1.9 Single ion in water simulations

MD simulations of single ion in water were performed in the NPT ensemble at 243.5K and 1 bar. Six ions were studied: Ca^{+}, Ca^{2+}, Ca^{3+}, K^{+}, K^{2+}, K^{3+}. In each case, the system consisted of one cation and 2000 TIP4P/Ice [284] water molecules. We used the same Lennard Jones parameters [283] for the cations as the ones used for the mica-water simulations.

The systems were equilibrated for 20 ns followed by a 100 ns production simulation. Berendsen thermostat and barostat [292] with a time constant of 2 ps were used to control the temperature and pressure during the equilibration simulation. In the production run, the V-rescale [286] thermostat and Parrinello-Rahman barostat [293] were used with a time constant of 2 ps for both. LINCS[287] algorithm was used to keep the water molecules rigid. Particle Mesh Ewald (PME) [288] was used to handle the long-range electrostatic interactions. A timestep of 2 fs was used. The configurations were stored every 2 ps. Simulations were performed using Gromacs

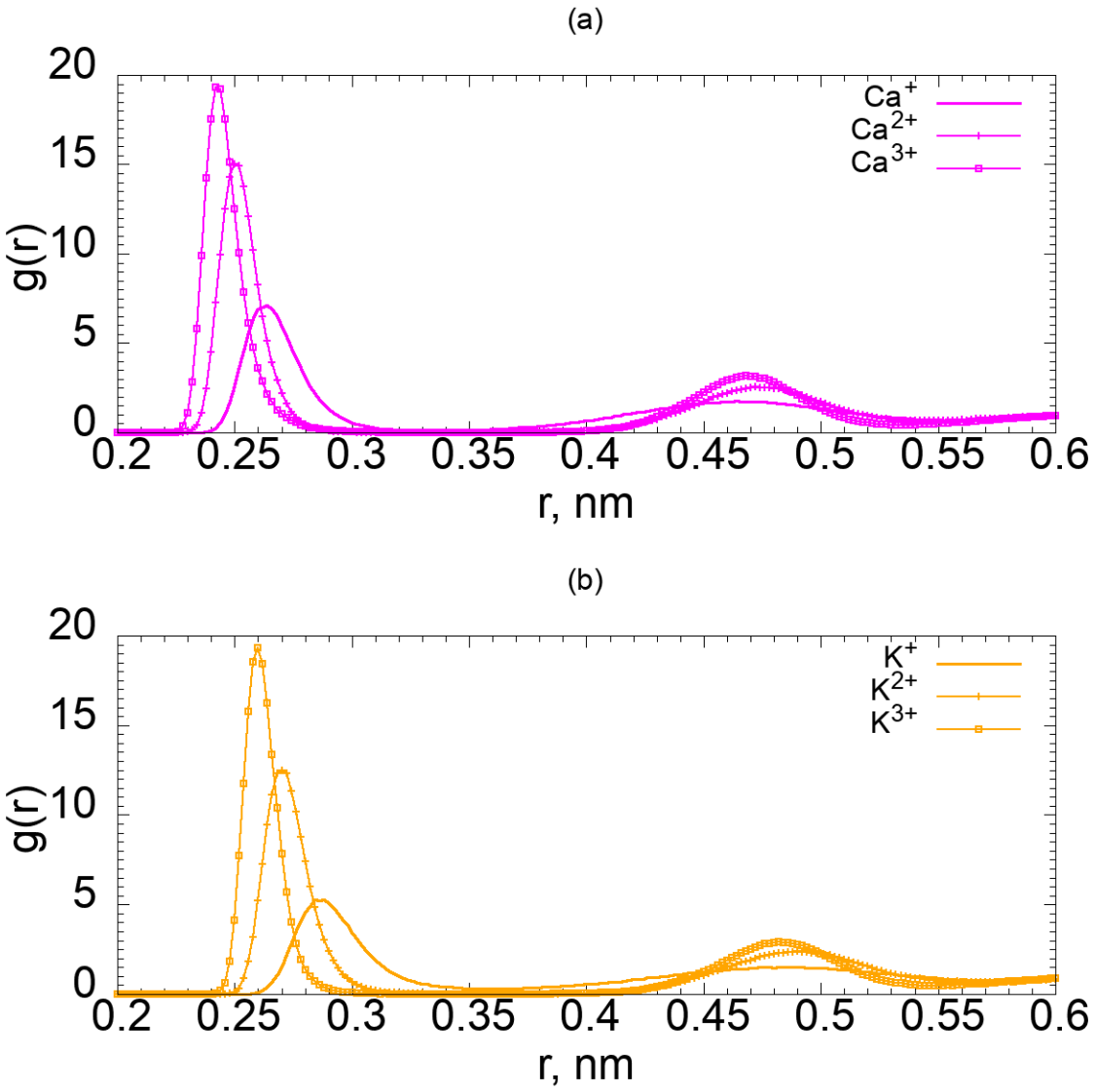

Figure B.9: Radial distribution function of cation and water oxygen calculated from simulations of single ion in water at 243.5 K. Panel (a): Ca ions with 1+, 2+ and 3+ charge. Panel (b): K ions with 1+, 2+ and 3+ charge.

2018.3 [289, 290, 291]. The radial distribution function (RDF) between the cation and water oxygen atoms are shown in Fig. B.9. The first and second minimum in these RDFs were used to determine the water molecules within the first and second hydration layer of the ions.

B.1.10 Microsecond long simulations on smaller Ca-mica surfaces

MD simulations of Ca-mica surfaces substituted with Ca^{2+} and Ca^{3+} ions were performed at 243.5K. The surface generation methodology was the same as described above. Since, these were longer simulations we reduced the surface dimensions to 3.1×3.6 nm^2. This corresponding simulation box dimensions were $3.1 \times 3.6 \times 20$ nm^3. A layer of 1500 water molecules was placed on the surface. All other simulation details are the same as described above. For each system, three simulations were performed by randomizing the molecular velocities of the atoms.

B.1.11 Clusters on $\mathbf{K}^{i+}, i = 1, 2, 3$ mica surfaces

The clusters of hydrogen bonded water molecules were calculated for the $K^{i+}, i = 1, 2, 3$ mica surfaces. The fraction of free water in the interfacial region as well as in the hydrogen bonded clusters was determined. The results are shown in Fig. B.10.

B.1.12 Ice-like water cluster identification

Water molecules were classified as ice-like using the tetrahedral order parameter (q) [149, 150]. The tetrahedral order parameter for a water molecule i is calculated using Eq. B.5, where n_i is the total number of water molecules in the first hydration shell of water molecule i and θ_{jik} is the angle between the oxygen atoms of water molecules j, i, and k (i.e., $\angle O_j O_i O_k$).

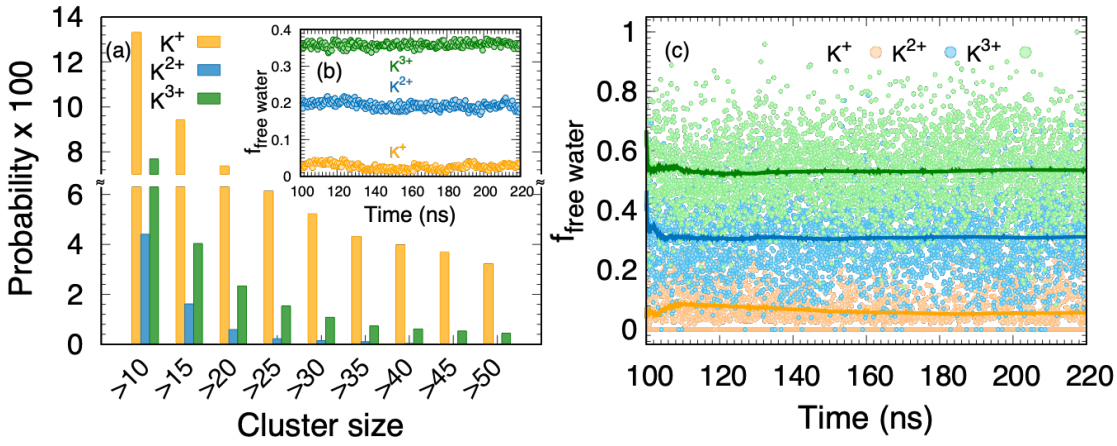

Figure B.10: Panel (a): Probability of observing clusters greater than a given size on the surface of K-mica with various charges. The data presented here uses the cutoff of 80% and observation window of 2 ns for determining hydrogen bonded water molecules. Panel (b): Fraction of free water within 0.8 nm of the mica surface.Panel (c): Fraction of free water in the largest cluster of hydrogen bonded water molecules. The solid lines indicate the running average.

$$q_i = \sum_{j=1}^{n_i-1} \sum_{k=j+1}^{n_i} (|cos\theta_{jik}|cos\theta_{jik} + \frac{1}{9})^2 \tag{B.5}$$

For a perfect tetrahedral, $q = 0$. We used a cutoff value of 0.4; if the tetrahedral order parameter is less than 0.4, the water molecule is tagged as ice-like. The cluster analysis was performed on the ice-like water molecules to obtain their clusters. Water molecules identified as ice-like and within 0.35 nm of each other were considered connected. Clusters between the connected water molecules were identified. No water molecule could belong to more than one cluster. Water molecules within 0.8 nm were considered for these calculations. We show the distribution of clusters of ice-like water molecules obtained from the microsecond long simulations of the Ca^{2+} and Ca^{3+}-mica (smaller) surfaces.

We also used PointNet based method [151] to identify the ice-like molecules. This is a stricter criteria than tetrahedral order parameter. We find that several water molecules in the largest clusters of hydrogen bonded water molecules were identified as ice-like. Fig. B.12 is a representative snapshot.

B.1.13 Simulations of mica surfaces with shifted ions

To investigate the role of the regions of mica surface devoid of ions in promoting ice nucleation, we created mica surfaces with ions shifted to limited region (approximately 1.5 nm in width) of the surface. This resulted in a large region on the mica surface devoid of ions. We performed these calculations on K^{3+}- and Ca^{3+}-mica. Fig.B.13 shows the representative snapshots of the mica surface with shifted ions. Simulations of water layer on these surfaces were performed at 243.5 K. The same simulation protocol described above was used here. The positions of the ions however, were restricted using position restraints. The analysis performed is the same as that described above. The analysis included identification of the largest cluster of hydrogen bonded water molecules, largest cluster of ice-like particles, and identification of free water in the hydrogen bonded clusters. Representative snapshots of the largest cluster of hydrogen bonded water molecules and largest clusters of ice-like particles are shown in Figs. B.14 and B.15.

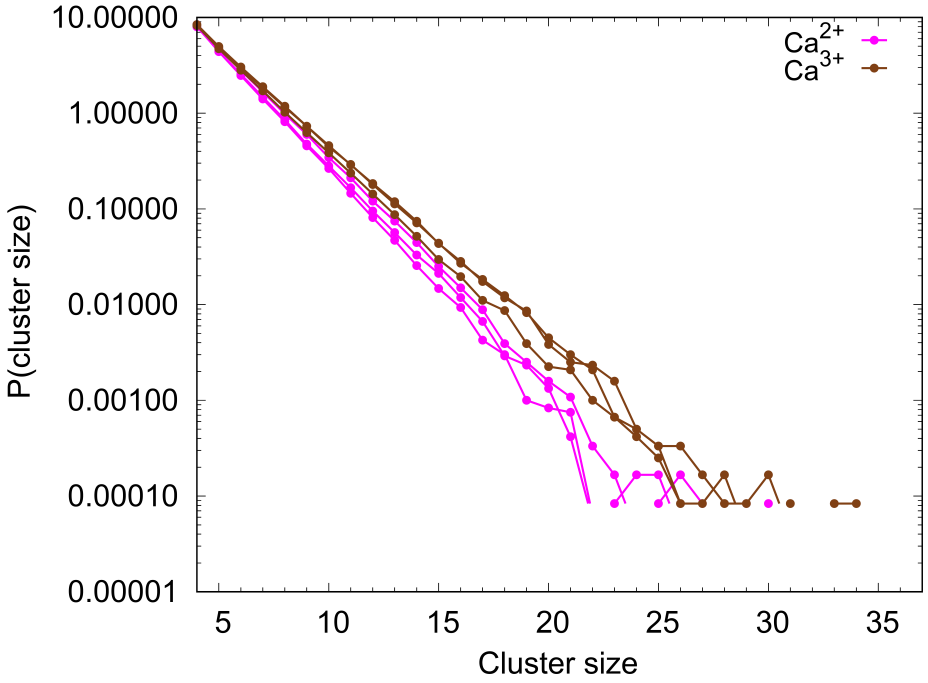

Figure B.11: Distribution of cluster size of ice-like water molecules for 3.1×3.6 nm^2 mica surfaces. Ice-like water molecules were identified using tetrahedral order parameter.

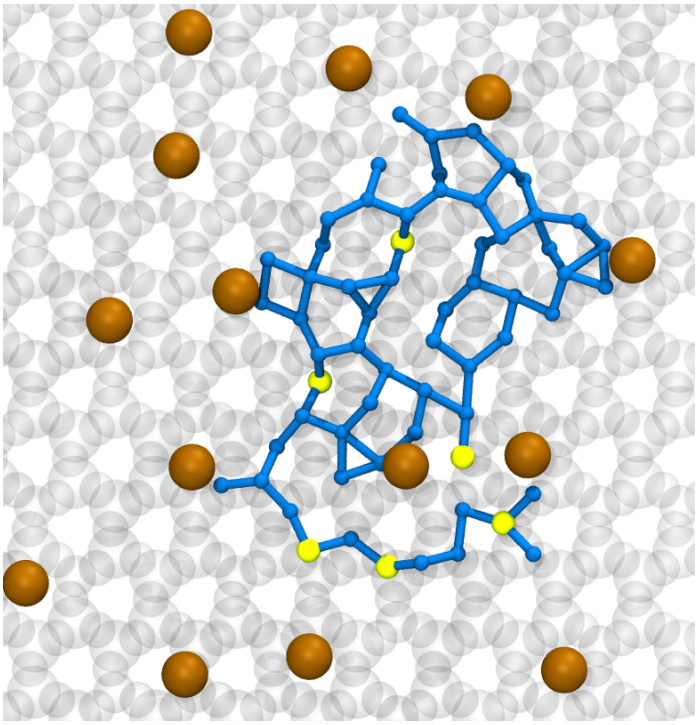

Figure B.12: Snapshot of a cluster of hydrogen bonded water molecules on Ca^{3+}-mica surface with ice-like water molecules identified from PointNet highlighted in yellow. Color code: gray:mica surfaces, sienna: Ca^{3+} ions, blue: hydrogen bonded water molecules and yellow: water molecules classified as ice-like by PointNet.

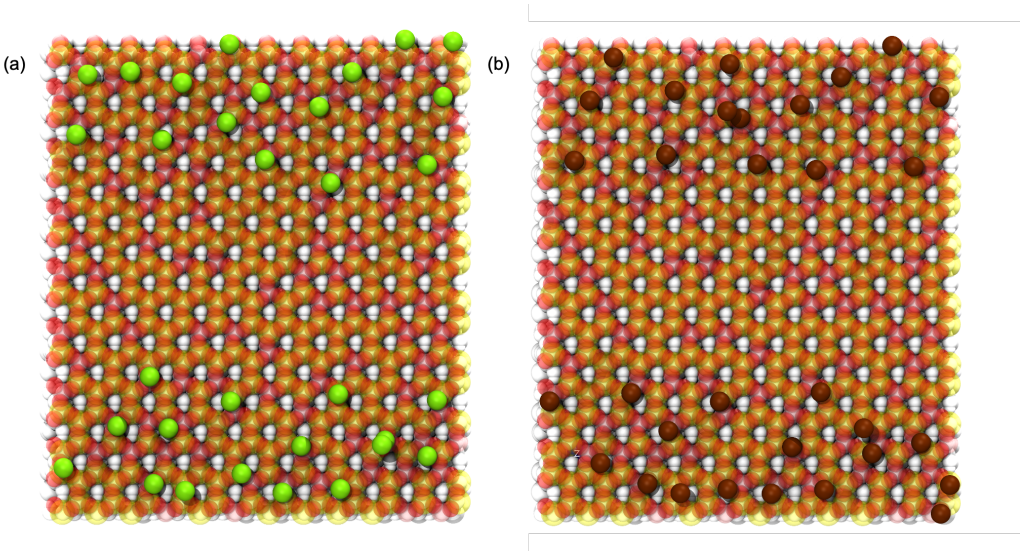

Figure B.13: Snapshots of (a) K^{3+}-shift and (b) Ca^{3+}-shift mica. The ions have been shifted to create a large region of mica surface devoid of any ions. Color code: yellow: Si, pink: Al, red: oxygen, green: K^{3+} ion and brown: Ca^{3+} ion.

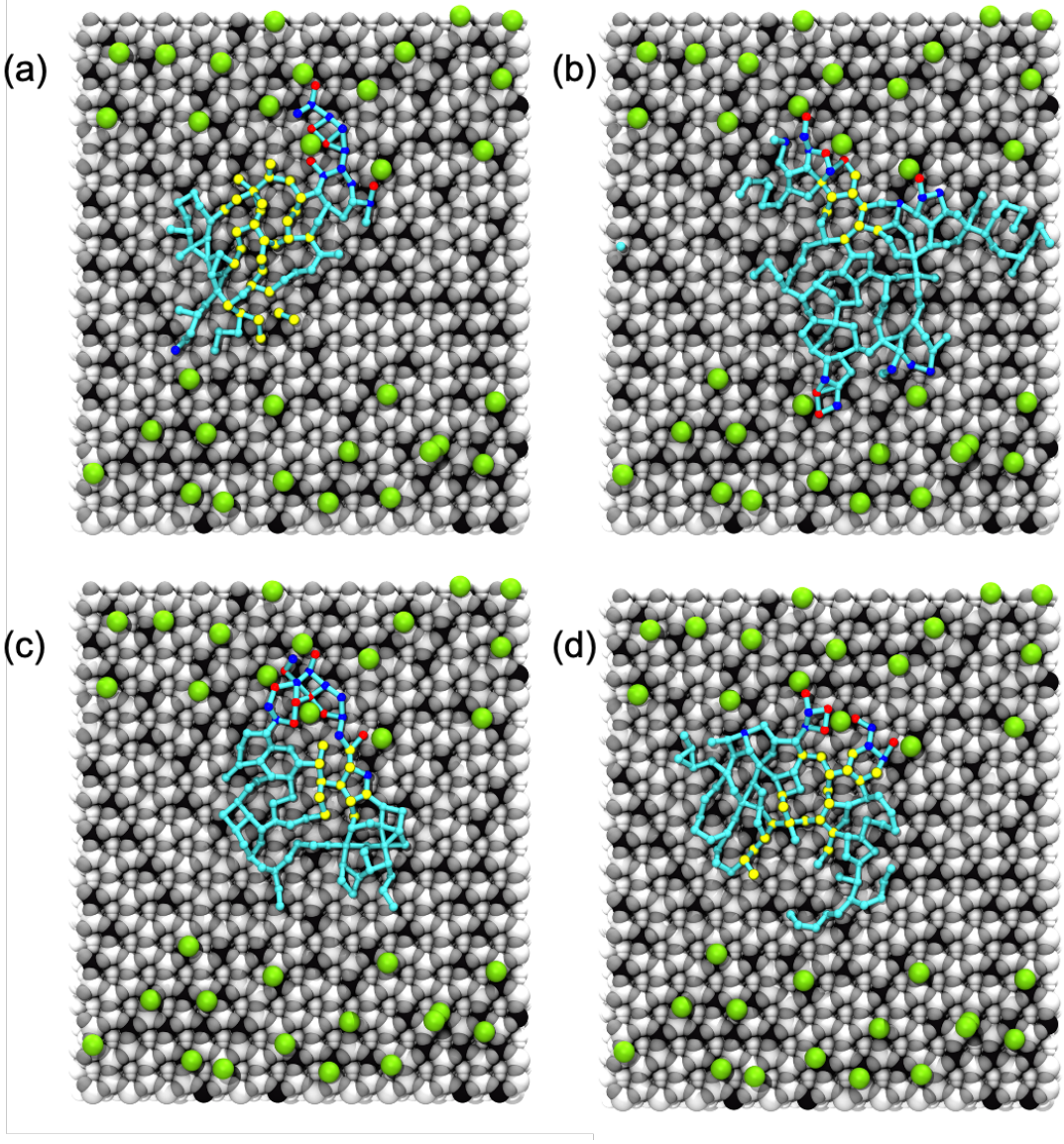

Figure B.14: Representative snapshots of hydrogen bonded clusters on K^{3+}-shift mica. Color code: white: Si, silver: Oxygen, grey: Al, red: water in 1st hydration shell of ions, blue: water in 2nd hydration shell of ions, cyan: free water, yellow: largest cluster of ice-like water molecules, and green: K^{3+} ion.

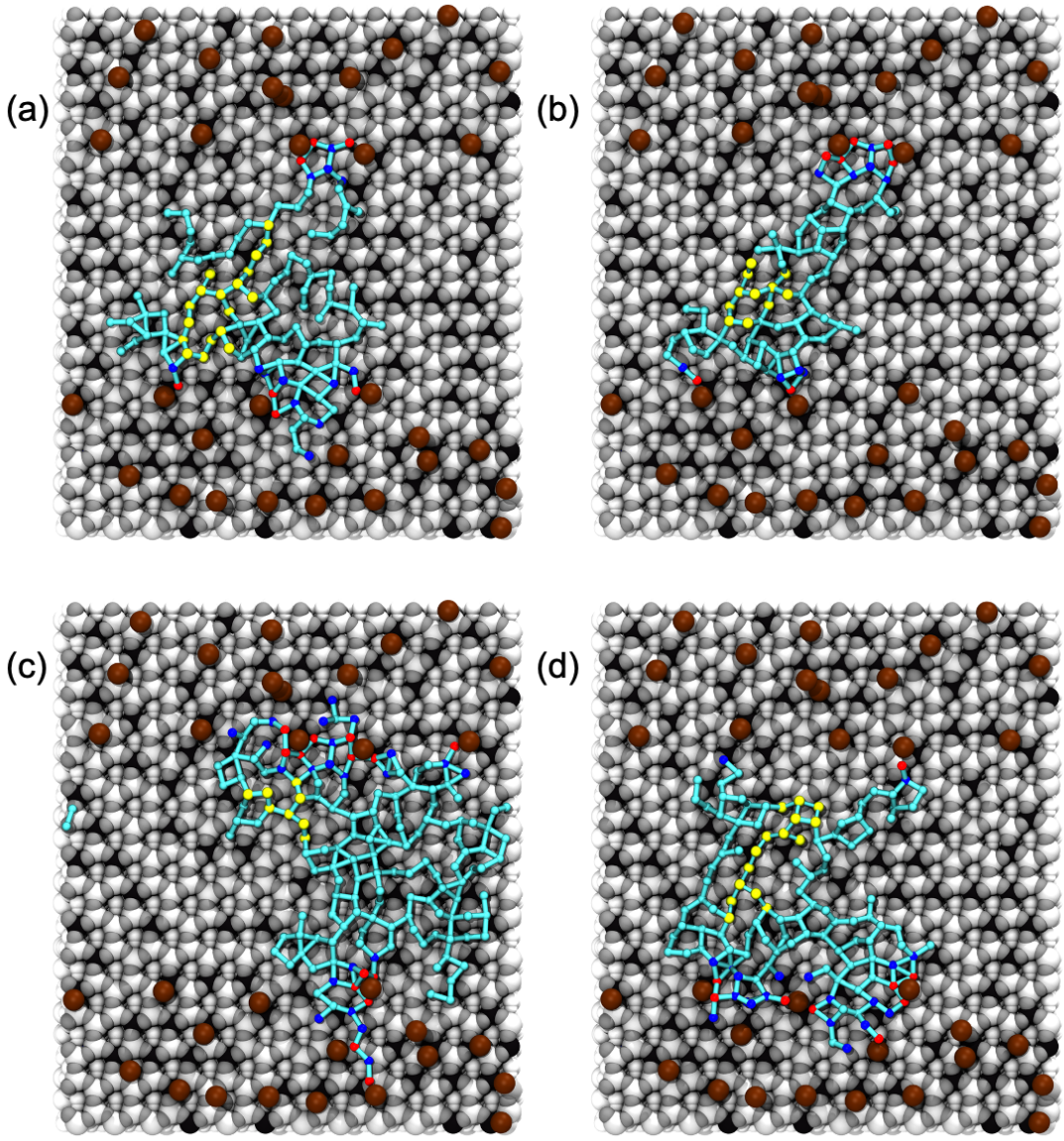

Figure B.15: Representative snapshots of hydrogen bonded clusters on Ca^{3+}-shift mica. Color code: white: Si, silver: Oxygen, grey: Al, red: water in 1st hydration shell of ions, blue: water in 2nd hydration shell of ions, cyan: free water, yellow: largest cluster of ice-like water molecules, and brown: Ca^{3+} ion.

B.2 Supplementary Information of Chapter 4

B.2.1 Introduction

The supporting information provides ten additional figures, six supplementary text sections and four supplementary tables.

B.2.2 Particle Dispersion Model

We performed backward mode simulations of the Lagrangian Flexible Particle (FLEXPART) dispersion model [205, 206, 207]. For each of the simulations corresponding to our aerosol samples, 80,000 passive air parcels were released from OMP and transported backward in time and space for up to 20 days [205]. The backward simulations calculated three-dimensional matrices of residence times of the air parcels every 3 hours in an output grid with a horizontal resolution of 1° latitude by 1° longitude and 11 vertical levels up to 15 km. The backward simulations can also calculate sensitivity factors of tracer mixing ratios at the receptor to emission fluxes in surface cells during the transport period. We multiplied the sensitivity factors with CO emission inventories, Emissions Database for Global Atmospheric Research version 4.2 (EC-JRC/PBL. , 2011) and the Global Fire Assimilation System [294] to estimate the CO contributions from anthropogenic and wildfire sources and air mass origins and ages [208].

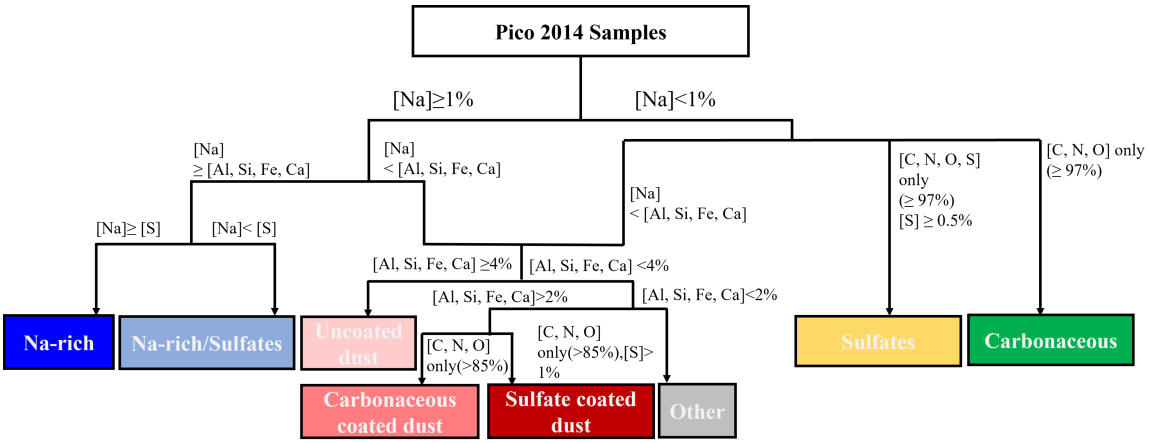

Figure B.16: Classification scheme used to identify the types of particles analyzed by CCSEM/ EDX.

B.2.3 Single-particle analysis

We used a computer-controlled environmental scanning electron microscope (FEI, Quanta 3D) to probe individual particles. The CCSEM is equipped with an energy dispersive X-ray (EDX) spectrometer with a Si (Li) detector possessing an active surface area of 10 mm^2. The X-ray spectra were taken at a beam current of 0.43 nA and an accelerating voltage of 20 kV. We utilized CCSEM/EDX data to classify thousands of individual particles. We classified the particles into eight categories based on their elemental compositions (atomic %): 1) Na-rich, 2) Na-rich/sulfate, 3) sulfate, 4) carbonaceous, 5) dust, 6) carbonaceous coated dust 7) sulfate coated dust, and 8) others. Figure B.16 illustrates the particle classification scheme. In the first step, all the particles were segregated into two classes based on particles containing more/less than 1 atomic percent of Na. Because the aerosol particles were collected near marine environment, so they will be either Na-rich or Na-lean. The Na-rich

particles were then subdivided into two groups based on the sum of the abundance of mineral elements: aluminum, silicon, iron, and calcium because these elements are common in dust particles. If the particles contained more sodium than mineral elements (Al, Si, Fe and, Ca), they were classified in either "Na-rich" ([Na] $\geq$ [S]) or "Na-rich/Sulfates" ([Na] $<$ [S]) categories, depending on the concentration of sulfur element with respect to sodium. Sodium-deficient ([Na] $<$ 1 atomic %) particle were classified into four groups. Particles dominated by carbon, nitrogen, and oxygen elements ($>$ 99 atomic %) were identified as "Carbonaceous particles". With sulfur concentration above a threshold level of 0.5 atomic %, the particles were classified as "sulfate" when C, N, O, S were found to be the major constituent elements ($>$ 99 atomic %). Particles containing [Al, Si, Fe, Ca] above 4% were considered dust. Particles containing [Al, Si, Fe, Ca] less than 4% were classified into two categories. If the atomic percent of the abundance of the element was less than 2%, the particle was considered as "other". Particles containing a percent of Al, Si, Fe, Ca greater than 2% were subdivided into two classes- with [C, N, O] percent greater than 85%, they were considered as carbonaceous coated dust, and with [C, N, O] percent greater than 85% with [S]$>$1% were considered as sulfate coated dust. For INP classification, we followed the same classification scheme, except we adjusted the [C, N, O] percent because we excluded Si and N from the classification and normalized the atomic percentage. Si and N constitute the Si_3N_4 substrates on which the IN experiments were conducted and including Si and N would result in an overestimation of these

elements.

The carbon features present in the aerosol population were analyzed using STXM/NEXAFS. The detail of the beamline at Advanced Light Source at Lawrence Berkeley National Laboratory is described elsewhere [295]. STXM utilizes the transmission of soft X-ray beams generated from a synchrotron light source across a raster-scanned sample at given photon energy to probe the chemical bonding of elements of interest. Particles were scanned for energy levels between 278 and 320 eV to obtain X-ray absorption spectra of the carbon K-edge. The X-ray transmitted through the particles acquired at each energy and position is then converted to an optical density (OD_E) using the Beer-Lambert Law:

$$OD_E = -\ln\left(\frac{I(E)}{I_o(E)}\right) = \mu(E)\rho t \tag{B.6}$$

Where I is the intensity at a given energy, I_o is the background intensity, $\mu(E)$ is the mass absorption coefficient at X-ray energy E, ρ is the mass density and t is the particle thickness [211]. The datasets acquired for this study included 'maps' that were collected at eleven different energies of the carbon K-edge and spectral 'stacks' that were collected at 111 energies of the carbon K-edge. The spatially resolved spectra yielded carbon composition and mixing states of individual particles. A 25 nm zone plate was used for the STXM imaging [296, 297]. The carbon K-edge images can be used to calculate the organic volume fraction (OVF) [213]. The thickness of

both organic and inorganic components was calculated from the optical density at energy either pre-edge (278 eV) or post-edge (320eV). The OD at each a given energy can be estimated as a linear combination of the ODs of the inorganic and organic components [213, 298] -

$$OD_{278} = \mu_{278}^{INO}\rho^{INO}t^{INO} + \mu_{278}^{ORG}\rho^{ORG}t^{ORG} \tag{B.7}$$

$$OD_{320} = \mu_{320}^{INO}\rho^{INO}t^{INO} + \mu_{320}^{ORG}\rho^{ORG}t^{ORG} \tag{B.8}$$

where INO and ORG representing inorganic and organic components. By taking $OD_{320} - OD_{278}$, the thickness of the inorganic (t^{INO}) and organic (t^{ORG}) components can be calculated as-

$$t^{INO} = \frac{OD_{278} - \mu_{278}^{ORG}\rho^{ORG}t^{ORG}}{\mu_{278}^{INO}\rho^{INO}} \tag{B.9}$$

$$t^{ORG} = \frac{OD_{320} - A^{INO}OD_{278}}{(\mu_{320}^{ORG} - A^{INO}\mu_{278}^{ORG}) \times \rho^{ORG}} \tag{B.10}$$

where, A^{INO} is $(\mu_{320}^{I}NO)/(\mu_{320}^{O}RG)$. Then the OVF was calculated by taking the ratio of the organic component thickness to the total thickness. The mass absorption coefficients were calculated using previous methods [299]. The densities of NaCl (2.16 gcm^3) and Adipic acid (1.36 gcm^3) are used for this work. The $OD_{320} - OD_{278}$ was used to calculate the TCA [212].

B.2.4 Mixing State Calculation

In this study, C, N, O, Na, Mg, Al, Si, P, S, Cl, K, Ca, Mn, Fe, and Zn elements were selected for mixing state calculation. A previous study showed CCSEM/EDX is more quantitative for elements with Z>11 and only semi-quantitative for C, N, and O [300] which added a caveat to the quantification mass calculation. This might result in an overestimation of C, N, and O mass. The mixing state parameterization begins with converting atomic percent data from the CCSEM-EDX to mass fractions [217, 218]. The individual mass m_i is calculated based on density due to elemental composition. In this study we used 1.77 gm/cm^3 for carbonaceous, 1.83 gm/cm^3 for sulfate, 2.2 gm/cm^3 for Na-rich particle, 2.6 gm/cm^3 for dust for mass calculation of carbonaceous, sulfate, Na-rich, and dust particles, respectively [301]. For calculating the masses of Na-rich sulfate, carbonaceous coated dust, and sulfate coated dust particles, we took the arithmetic mean of the densities of known aerosol classes; for example, to get the density of Na-rich sulfate particles, we took the average of the density of Na-rich class and Sulfate class. The masses of each of the elements were calculated by multiplying the atomic percent data by the particle mass. The volumes of the particles were calculated from the area equivalent diameter. The masses of the particles were then calculated by multiplying the volume with the densities of each of the aerosol classes. Then the mass fraction of a particle within a sample, the mass fraction of components within a sample and mass fraction of component a within particle was calculated. The Shannon entropy for each particle (H_i), each

component H_α and for the bulk H_γ is then calculated using the mass fractions. From the Shannon entropy the diversity values for the number of species within a specific particle D_i, the average number of species within any given particle D_α, the number of species within the entire sample are defined with the following equations-

$$D_i = e^{H_i}, D_\alpha = e^{H_\alpha}, D_\gamma = e^{H_\gamma} \tag{B.11}$$

The mixing state index χ is calculated from the diversity values using the following equation-

$$\chi = \frac{D_\alpha - 1}{D_\gamma - 1} \tag{B.12}$$

B.2.5 Spectral Deconvolution

We performed spectral deconvolution analysis to determine the relative contribution from each of the observed functional groups [210, 220]. The spectral deconvolution creates a fit of a spectrum using a nonlinear least square fit algorithm. The deconvolved peaks were fitted with a pre-edge subtracted normalized spectrum. The fitting was done by adjusting the peak positions and width value to obtain the height of each of the peaks. From the peak height and width, the area under the curve is calculated. The fit parameters are listed in Table S2. Figure B.22 shows the representative spectral deconvolution obtained for carbon K-edge spectrum for this study.

B.2.6 Estimation of glass transition temperature (T_g) and relative humidity-dependent glass transition temperature T_g(RH)

Gordon-Taylor equation from a previous study was used to calculate the glass transition temperature [302].

$$T_g(w_{org}) = \frac{w_w T_{g,w} k_{GT} + w_{org} T_{g,dry}}{w_w k_{GT} + w_{org}} \tag{B.13}$$

$$RH = 100 \times \left(1 + \kappa_{org} \times \frac{\rho_w}{\rho_{org}} \frac{w_{org}}{w_w}\right)^{-1} \tag{B.14}$$

Here w_{org} is the mass fraction of organics, w_w is the mass fraction of water, $T_{g,w}$ is the glass transition temperature of water (136K), k_{GT} is the Gordon-Taylor constant (taken as 2.5 from a previous study) [302], $T_{g,org}$ is the dry glass transition temperature, ρ_w is the density of water (1 g/cm^{-3}), ρ_{org} is the density of organic (1.4 g/cm^3), κ_{org} is the CCN derived hygroscopicity parameter of the organic fraction (0.17) [194]. For this study, we adopted the mean $T_{g,dry}$ from a previous study [227]. Equation S8 is converted to $T_g(RH)$ by converting w_{org} to relative humidity dependent term [227, 228, 302].

$$T_g(RH) = \frac{\left(1 - \frac{1.4 - \frac{1.4 \times RH}{100}}{1.4 - \frac{1.28 \times RH}{100}}\right) \times 136 + 0.4 \times \left(\frac{1.4 - \frac{1.4 \times RH}{100}}{1.4 - \frac{1.28 \times RH}{100}}\right) \times T_{g,dry}}{\left(1 - \frac{1.4 - \frac{1.4 \times RH}{100}}{1.4 - \frac{1.28 \times RH}{100}}\right) + 0.4 \times \left(\frac{1.4 - \frac{1.4 \times RH}{100}}{1.4 - \frac{1.28 \times RH}{100}}\right)} \tag{B.15}$$

B.2.7 Ice Nucleation Experiments

The ice nucleation experiments were performed using a custom-made temperature and humidity-controlled cryo-stage that was described in detail in a previous study [214]. The ice nucleation setup was interfaced with a temperature control unit (Model 22C, Cryogenic Control Systems, Inc.) and a water vapor supply to control relative humidity inside the chamber. The temperature of the cryo-stage was monitored by a temperature sensor ($\pm$0.15 K, Pt-100, Omega Engineering Inc.) that was located at the bottom of the sample holder. The desired dew point temperature (T_d) was achieved by passing ultra-high purity dry $N_2(g)$ through a temperature-controlled water reservoir and then pumped into the ESEM chamber. Ice nucleation experiments were performed at isobaric (constant T_d) as well as isothermal conditions, meaning constant particle/substrate temperature (T_p). The first ice nucleation event over the entire exposed area was detected by looking at SEM images during isobaric experiments while decreasing the T_p at a rate were of 0.1-0.2 K/min. A chilled mirror hygrometer (GE Sensing, Model 1311XR) was used to measure the T_d. T_p and T_d were used to calculate the relative humidity with respect to ice (R_{Hice}), from the ratio of $P(T_d)$ and $P_{ice}(T_p)$ where $P(T_d)$ and $P_{ice}(T_p)$ denoted the water vapor partial pressure in the ESEM chamber and saturation vapor pressure over ice at T_p, respectively. The

error of RH_{ice} was calculated using the below equation-

$$Error = RH_{ice} - 100 \times \frac{e^{(9.550426-5723.265/(T_d-0.15)+3.53068\times LN((T_d-0.15))|0.00728332\times(T_d-0.15))}}{e^{(9.550426-5723.265/(T_p+0.3)+3.53068\times LN((T_p+0.3))|0.00728332\times(T_p+0.3))}} \tag{B.16}$$

Here, T_d= dew point temperature T_p= Particle temperature

B.2.8 Estimation of N_{INP}

We estimated the activated INP (N_{INP}) per liter of air via deposition mode (205-220K) for each of the samples which are provided in Table S1. To compute the N_{INP} values, the observations of INP activated fractions and measurements of total particle number concentration in air (ambient condition) obtained with an optical particle counter (> 0.3 micron) throughout each sample collection period were used. The observed active fractions were computed using the ratio of the number of ice crystals generated simultaneously to the total number of particles on the substrate. This calculation results in the N_{INP} 0.017, 0.017 and 0.01 L^{-1} for sample SA1, SA2, SA3 respectively. The calculated INP concentrations are within the range of the previous OMP study [164].

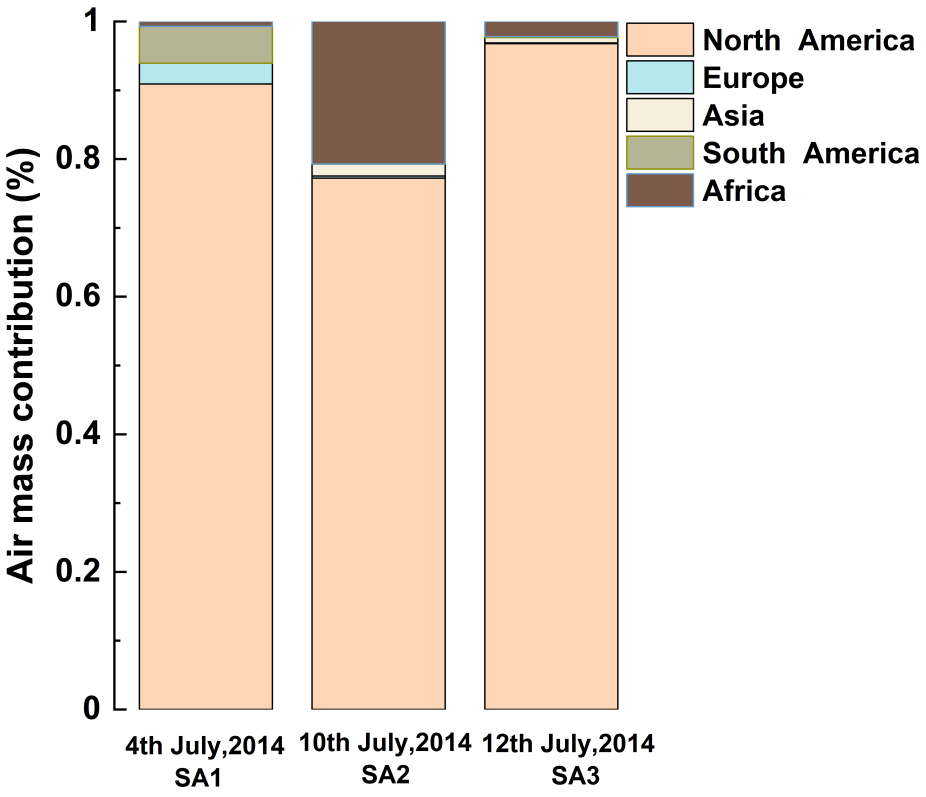

Figure B.17: The bar graph of folded (multipled) contribution (%) of air mass concentration at each site at the respective times.

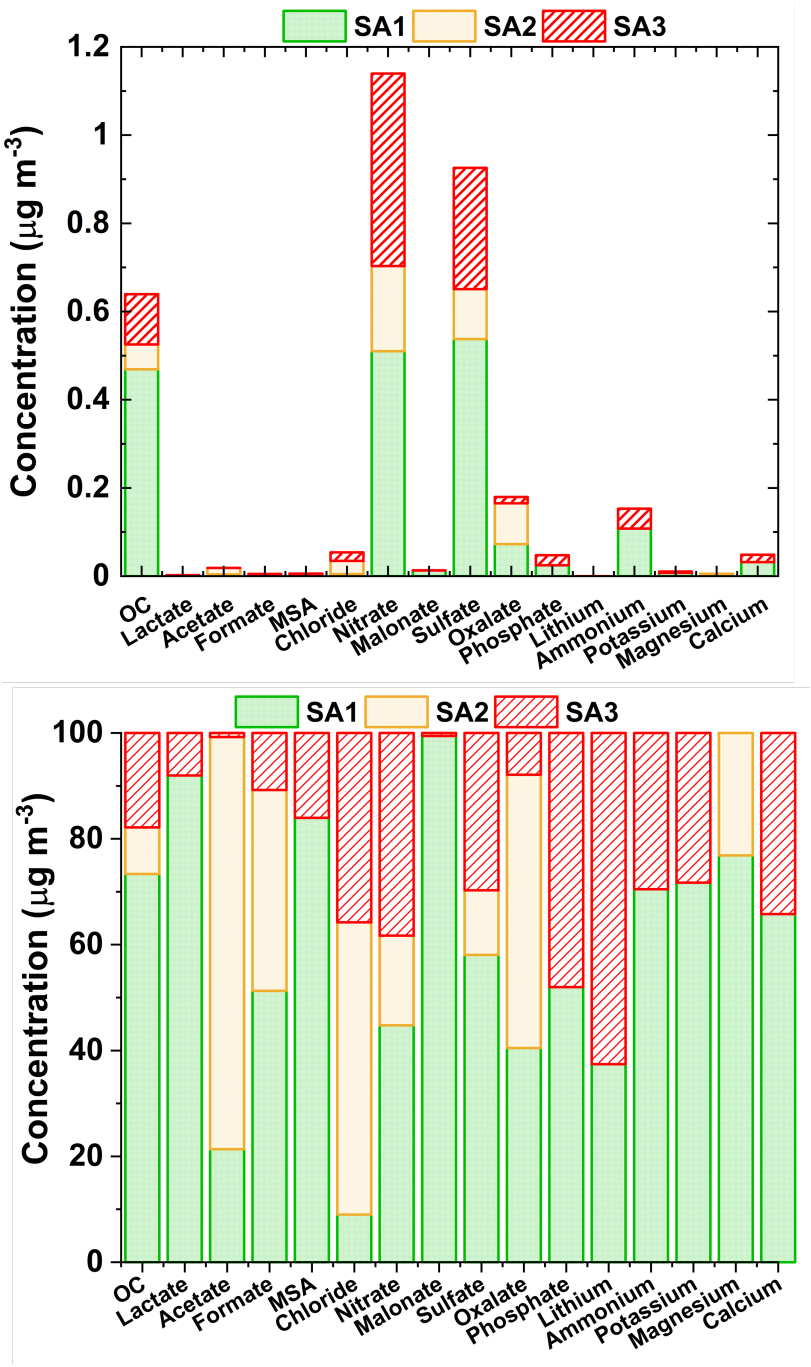

Figure B.18: The top panel reports the concentration and the bottom panel normalized values of elemental carbon, organic carbon, anion, and cation. Note, sodium concentrations were not reported due to the high blank concentrations associated with quartz filters.

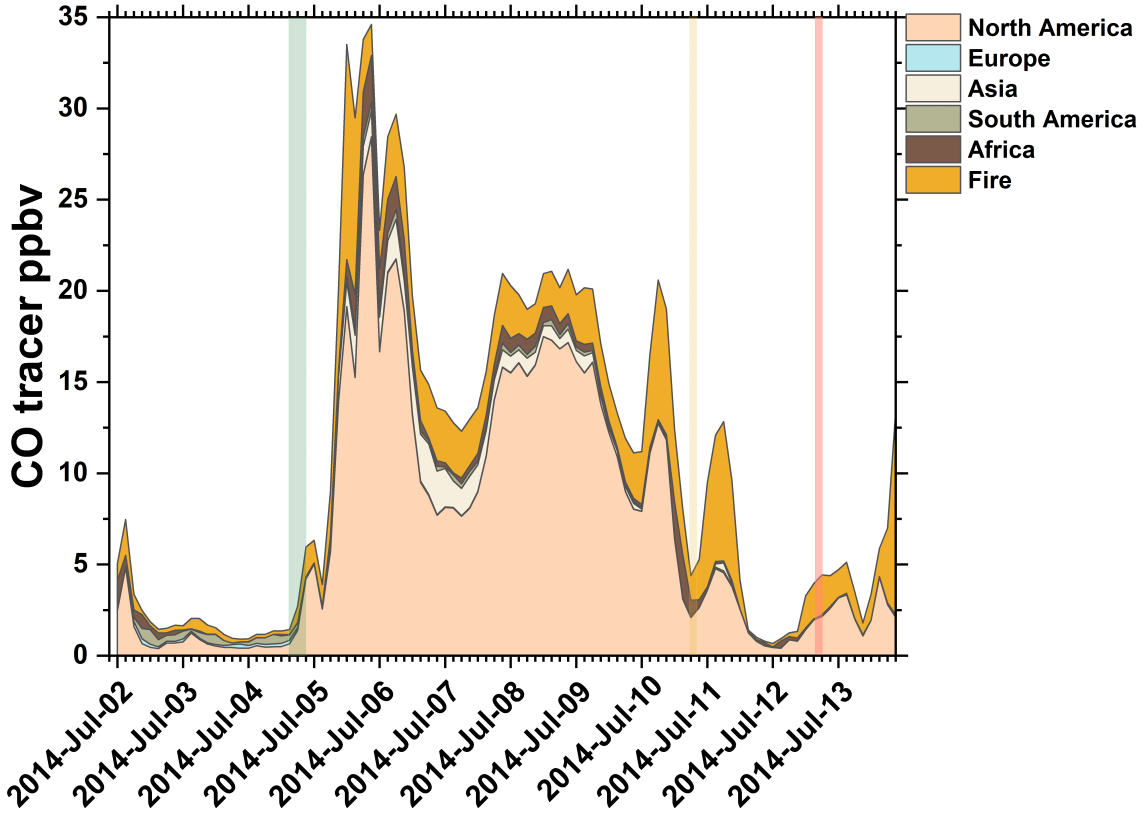

Figure B.19: FLEXPART carbon monoxide source apportionment plot for different sampling times shown with different colors, e.g. SA1 (green), SA2 (yellow), SA3 (red).

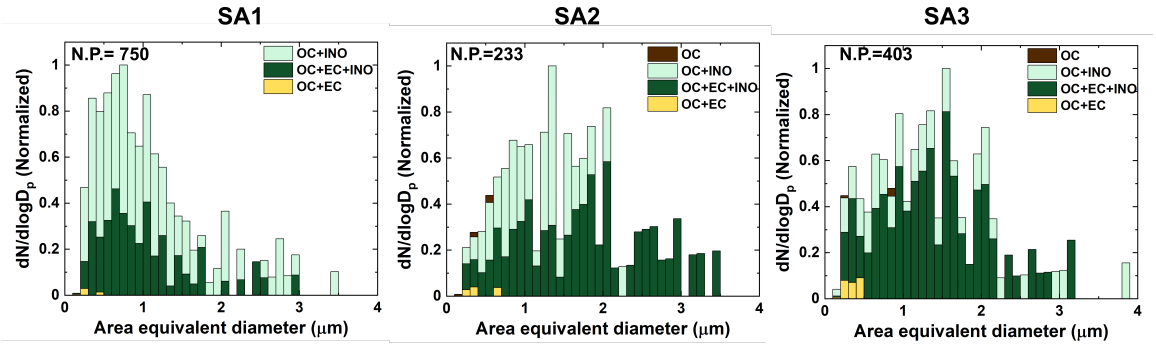

Figure B.20: Size-resolved mixed particle classes obtained from STXM/NEXAFS; N.P. stands for the number of particles analyzed.

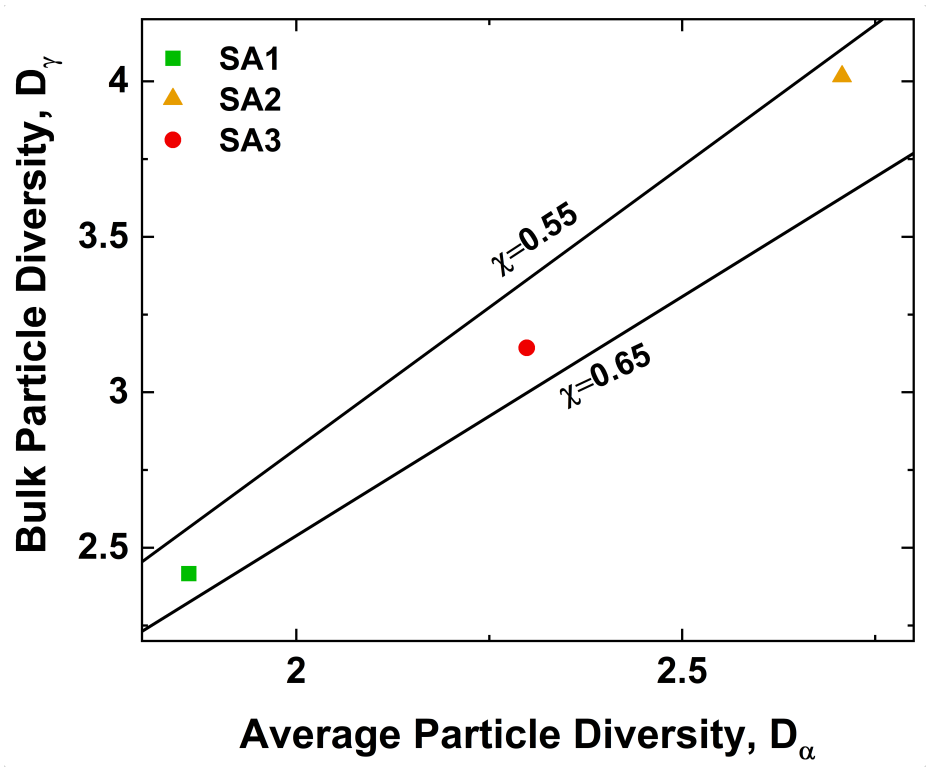

Figure B.21: Scatterplot of average particle species diversity, D_α, and bulk population species diversity, D_γ. The solid lines indicate constant mixing state index χ values. Green, mustard yellow, and red filled circles represent sample SA1, SA2, and SA3 respectively.

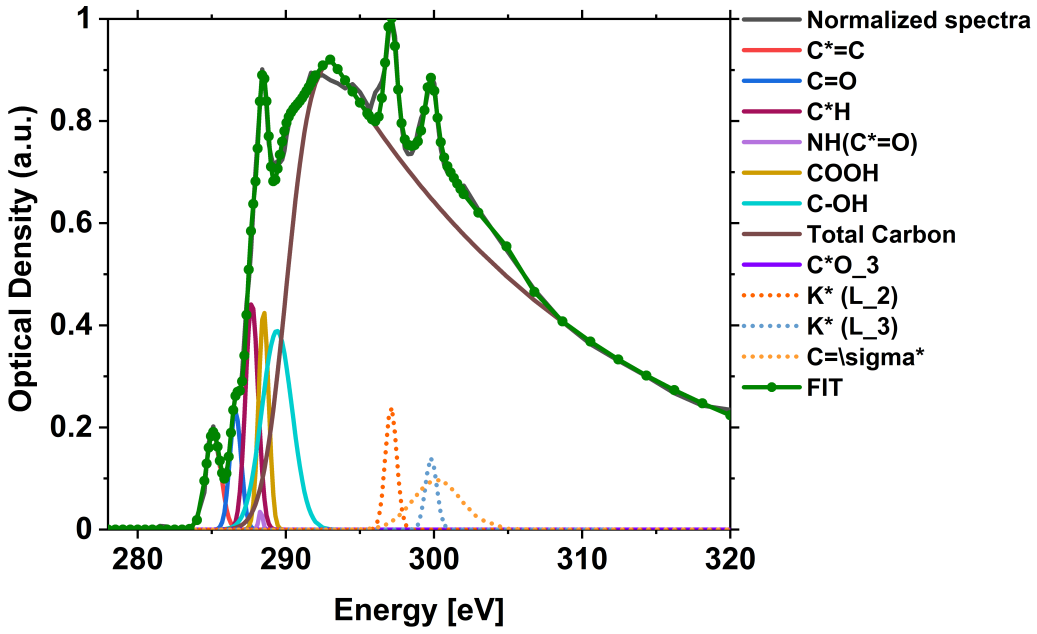

Figure B.22: Representative spectral deconvolution of carbon K-edge spectrum. The bold black line is the normalized spectrum obtained from the experimental data and the green line is the fitted curve. Each of the colors showed different fitted peaks.

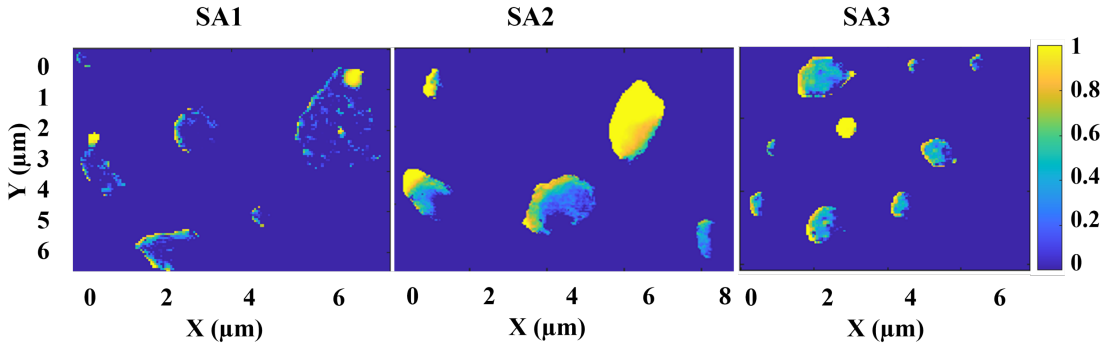

Figure B.23: Representative organic volume fraction maps from STXM/NEXAFS analysis for different samples with respect to NaCl/Adipic acid system. The yellow color indicates organic-rich, and the blue color indicates inorganic-rich portions of the particles.

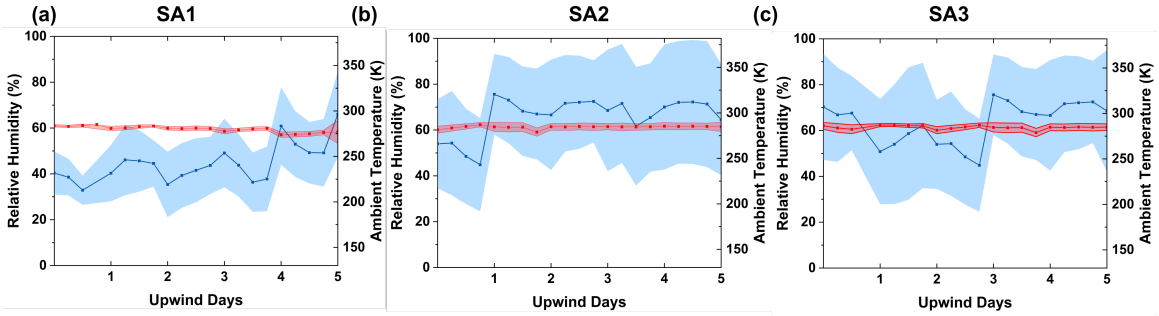

Figure B.24: The plots (a)–(c) represent the ambient conditions of sample SA1, SA2 and, SA3 respectively for the last five days of transport, the conditions were extracted from the GFS analysis along the FLEXPART modeled path weighted by the residence time. The red and blue line represents the mean value of temperature and RH respectively and the shaded region represents the uncertainty of the temperature and RH.

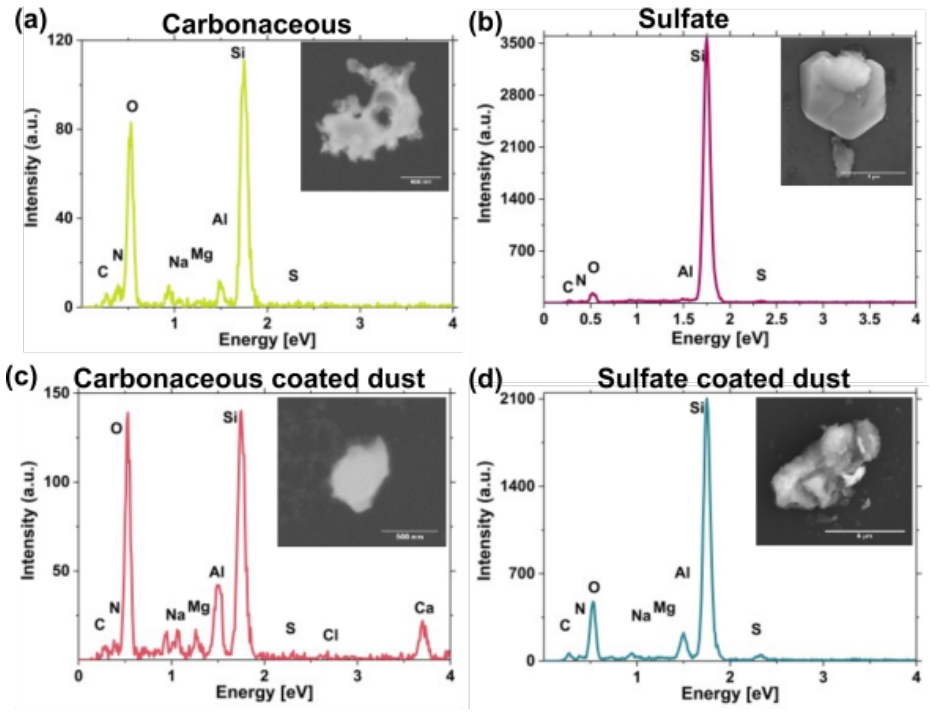

Figure B.25: Representative scanning electron microscopy images of the identified INPs of different classes (a) carbonaceous, (b) sulfate, (c) carbonaceous coated dust and, (d) sulfate coated dust and their respective energy dispersive X-ray spectra.

Table B.2
Sampling dates, times, plume age, estimated mass fraction of organic carbon, concentration, and size of the particle population and of the INPs[(a)]

Sample	Sampling Date and Times (2014)	Plume Age (Day)	OC ($\mu g/m^3$)	DA_{eq} (µm)	A_s (mm^2)	f_A (10^{-5})	d_{INP} (µm)	N_{INP} (L^{-1})
SA1	4 July 14:49-21:00	16.37	0.469	0.52 (±0.71)	0.015 (±0.001)	7.03 (±1.11)	NA	0.017 ±0.003
SA2	10 July 17:24-20:22	16.24	0.056	0.58 (±0.52)	0.012 (±0.002)	9.99 (±5.34)	2.56 (±2.01)	0.017 ±0.009
SA3	12 July 15:07-18:33	16.01	0.114	0.48 (±0.49)	0.023 (±0.001)	4.26 (±0.42)	2.25 (±1.47)	0.010 ±0.001

(a) Mean area equivalent diameter (D_{Aeq}), the total surface area of the particles available for ice nucleation (A_s), INP diameter (d_{INP}). The numbers in brackets indicate the standard deviations for D_{Aeq}, A_s, d_{INP}. For sample SA1, d_{INP} is not available.

Table B.3
Spectral deconvolution parameters.

Energy (eV)	Transition	Functional group	Width (eV)	References
285.1	$K1s \rightarrow \pi^*$	$'C^* = C'$	1.20 ± 0.07	[220, 297]
286.6	$K1s \rightarrow \pi^*$ or $K1s \rightarrow \pi^*$	$C = O'$ or C^*OH	0.92 ± 0.09	[211, 303]
287.7	$K1s \rightarrow C^*H$	$'C^* = H'$	1.10 ± 0.11	[220, 222, 304]
288.3	$K1s \rightarrow \pi^*$	$'NH(C^* = O)'$	0.38 ± 0.40	[220, 222, 304]
288.6	$K1s \rightarrow \pi^*$	$'COOH'$	0.89 ± 0.05	[211, 220, 225, 304]
289.5	$K1s \rightarrow \pi^*$	$'C - OH'$	1.2 ± 0.06	[210, 211, 220, 222, 304]
290	Edge Step	Total Carbon	2 ± 0.20	[210, 211, 220, 222, 304]
290.4	$K1s \rightarrow \pi^*$	$'C^*O3$	0.68 ± 0.10	[210, 211, 220, 222, 304]
297.1	$L_2 2p_{1/2}$	K^*	1.20 ± 0.40	[210, 211, 220, 222, 304]
299.7	$L_3 2p_{3/2}$	K^*	0.82 ± 0.31	[210, 211, 220, 222, 304]
300.2	$1s \rightarrow \sigma^*$	$'C^* = C, C^* = O$	4.08 ± 1.25	[210, 211, 220, 222, 304]

Table B.4
Average particle concentration in the air from optical particle counter measurement, number of particles analyzed using CCSEM/EDX, STXM/NEXAFS and aspect ratio measurement.

Sample	N_p, L^{-1} (>0.3µm)	N_p,L^{-1} (>0.4µm)	Number of Particles analyzed using CCSEM/EDX (Size resolved chemical composition & mixing state)	Number of Particles analyzed using STXM/NEXAFS (Mixing state, TCA)	Number of particles analyzed for Aspect ratio measurement
SA1	247.4	79	11099	750	122
SA2	171.1	56	4346	233	104
SA3	171.3	35	8252	403	102

Table B.5
Particle phase state in different samples from STXM/NEXAFS Measurements.

Samples	Mixing State	Number of Particles	Phase State			Phase State (%)		
			Solid	Semi Solid	Liquid	Solid	Semi Solid	Liquid
SA1	OC + INO	299	53	81	165	17.80	27.02	55.18
	OC+EC	4	4	0	0	100.00	0.00	0
	OC+EC+INO	178	38	61	79	21.35	34.27	44.38
	OC	0	0	0	0	0.00	0.00	0
SA2	OC + INO	86	6	24	56	6.98	27.91	65.11
	OC+EC	3	2	1		66.67	33.33	0
	OC+EC+INO	82	19	25	38	23.17	30.49	46.34
	OC	2	2	0	0	100.00	0.00	0
SA2	OC + INO	80	7	13	60	8.75	16.25	75
	OC+EC	16	10	6	0	62.50	37.50	0
	OC+EC+INO	198	24	34	140	12.12	17.17	70.71
	OC	2	1	0	1	50.00	0	50

Table B.6
The temperature and relative humidity with respect to ice for both the mixed-phase and cirrus cloud regimes investigated using the ESEM.

Sample	Mixed Phase Cloud Regime		Cirrus Cloud Regime	
	Temperature (K)	RHice (%)	Temperature (K)	RHice (%)
SA1	235 - 250	120 - 128	205 - 220	119 - 125
SA2	235 - 250	117 - 131	205 - 220	126 - 139
SA3	235 - 250	121 - 136	205 - 220	134 - 135

Table B.7

Experimentally derived heterogeneous ice nucleation rate coefficients, J_{het} as a function of the water activity criterion, Δa_w used in Figure 4.6(c).

	Δa_w	J_{het} ($cm^{-2}s^{-1}$)		Δa_w	J_{het} ($cm^{-2}s^{-1}$)		Δa_w	J_{het} ($cm^{-2}s^{-1}$)
	0.1435	47.5182		0.1234	56.74531		0.14351	27.06575
	0.14351	51.83821		0.14423	61.90418		0.15801	29.32108
	0.16274	57.02168		0.14788	68.09575		0.16734	31.98674
	0.16988	63.35779		0.17554	75.66064		0.17597	35.1852
	0.17771	71.2771		0.18027	85.11968		0.18616	39.09489
	0.1807	81.45917		0.19847	97.2792		0.20464	43.9815
SA1	0.18596	95.03641	SA2	0.20372	113.49324	SA3	0.21404	50.26434
	0.18622	114.04336		0.21318	136.1915		0.21405	58.64217
	0.19173	142.55419		0.21416	170.23937		0.23405	70.3704
	0.19461	190.07281		0.22408	226.98126		0.23914	87.96299
	0.1975	285.10839		0.22526	340.47874		0.2409	117.28433
	0.20436	570.21679		0.23917	680.95749		0.24392	175.92599
							0.27622	351.85198

B.3 Supplementary Information for Chapter 5

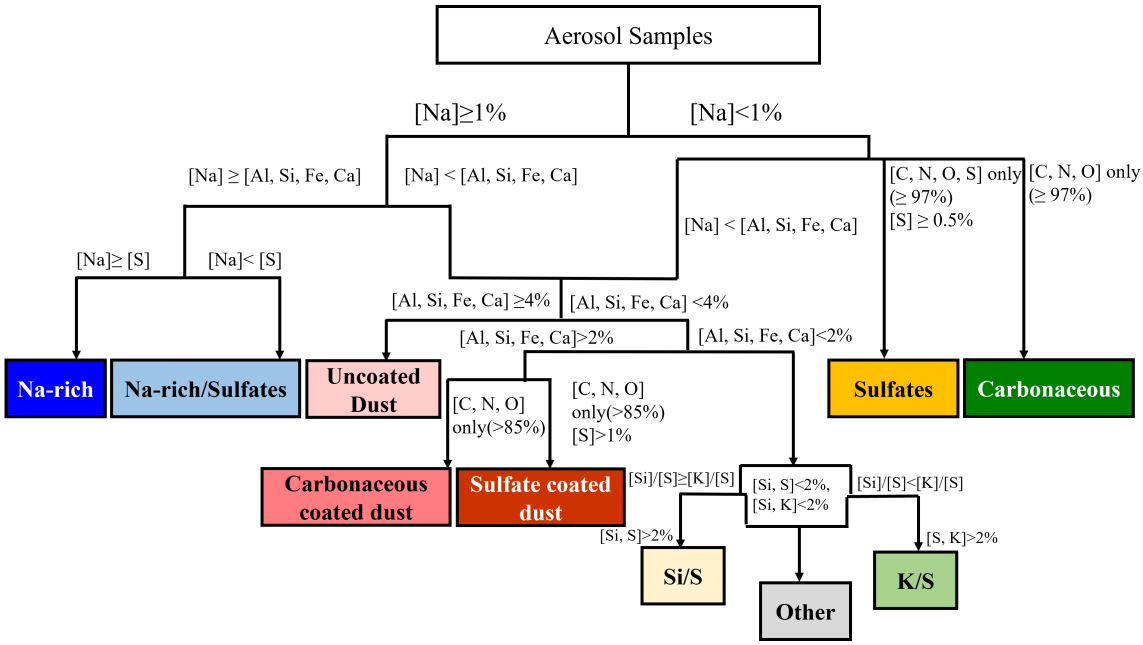

Figure B.26: Classification scheme used to identify the types of particles analyzed by CCSEM/EDX.

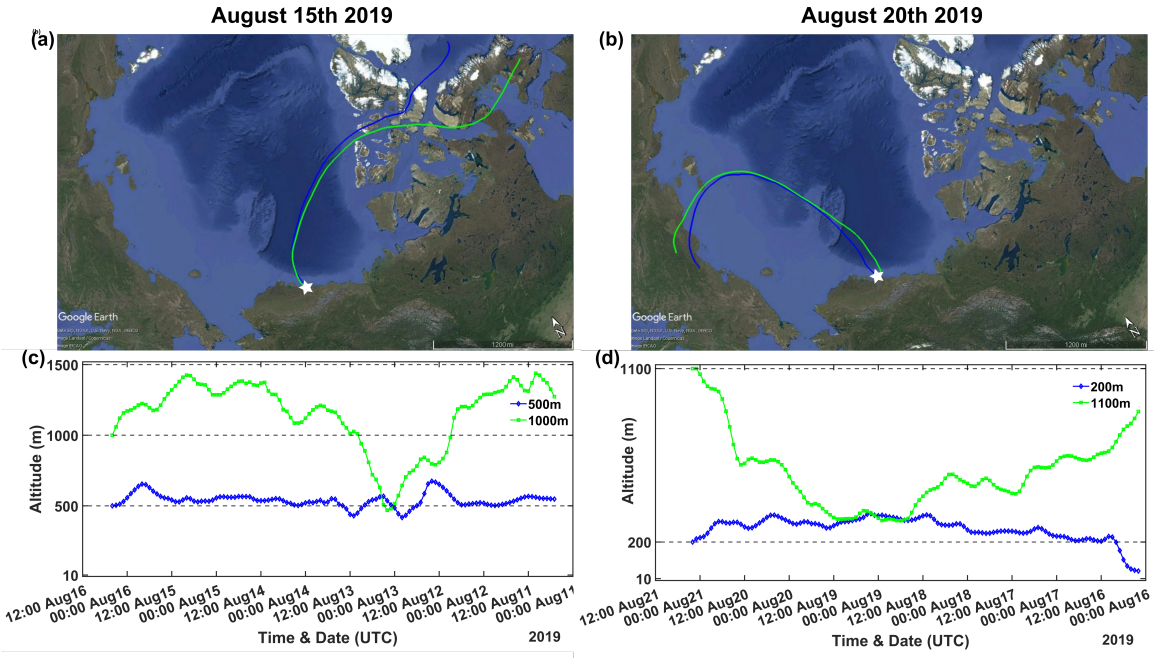

Figure B.27: 120 h Hybrid Single-Particle Lagrangian Integrated Trajectory (HYSPLIT) back trajectory for the end of each sampling period for the samples collected 08/15/2019 (a, c), samples collected on 08/20/2019 (b,d).

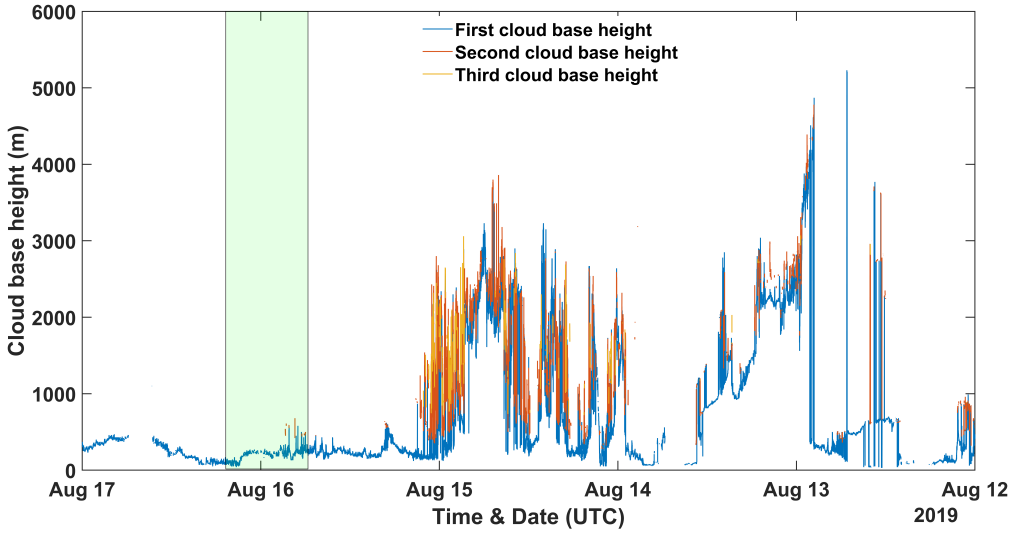

Figure B.28: Cloud base heights measured from ceilometer.

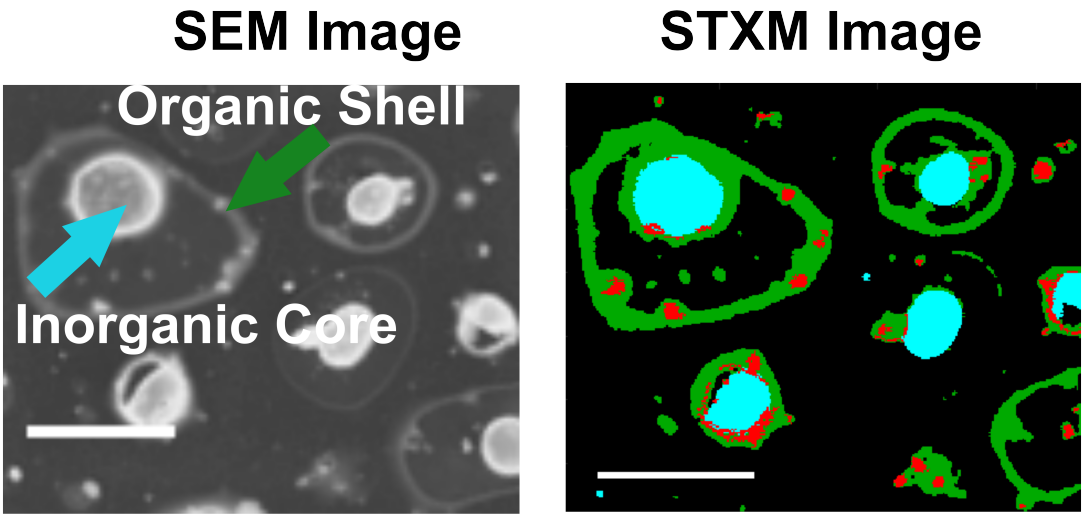

Figure B.29: Core-shell morphology of particles from case study 1 at 1000m. The left panel shows the particle morphology from SEM imaging. The right panel shows the same field of view of the particles using STXM/NEXAFS Imaging

Table B.8
Dates, times, flight hours, altitude and, the instrument flown during TBS flights.

Sampling Date	Sampling time (UTC)	Flight hours (hr)	Altitude (m)	Instrument flown
08/15/2019	21 : 18 : 00 – 03 : 41 : 00	5	500m	iMet, POPS, CPC
08/15/2019	21 : 18 : 00 – 03 : 41 : 00	5	1000m	iMet, POPS, CPC
08/20/2019	23 : 44 : 00 – 01 : 37 : 00	2.7	200m	iMet, POPS, CPC
08/20/2019	23 : 26 : 00 – 01 : 37 : 00	3.9	1100m	iMet, POPS, CPC